博 士 学 位 論 文
Doctoral Thesis

論文題目

Thesis Title

Wind Tunnel Testing Techniques for Trains to Assess Crosswind Stability and Evaluate Aerodynamic Noise with Noise Source Detection

東 北 大 学 大 学 院 工 学 研 究 科

Graduate School of Engineering,

TOHOKU UNIVERSITY

専攻/Department: Department of Aerospace Engineering

学籍番号/ ID No: C0TD1609

氏 名 /Name: Akitoshi MATSUI

TOHOKU UNIVERSITY
Graduate School of Engineering

Wind Tunnel Testing Techniques for Trains to Assess Crosswind Stability and Evaluate Aerodynamic Noise with Noise Source Detection

（鉄道車両の横風環境下での走行安定性評価および
騒音源特定による空力音予測に向けた
風洞試験技術の開発）

A dissertation submitted for the degree of Doctor of Philosophy (Engineering)

Department of Aerospace Engineering

by

Akitoshi MATSUI

January 10, 2023

Wind Tunnel Testing Techniques for Trains to Assess Crosswind Stability and Evaluate Aerodynamic Noise with Noise Source Detection

Akitoshi MATSUI

Abstract

In the present dissertation, the innovative wind tunnel testing techniques that can assess the crosswind stability and evaluate the aerodynamic noise with noise source detection were developed towards the future high-speed train with the low CO_2 emission.

Firstly, an aerodynamic force and moment measurement system was developed in a compact wind tunnel for repeatable easy evaluations of the crosswind stability. The target of the measurement system, which is consisted of a wide nozzle and a splitter plate, was to achieve the same measurement accuracy as the European Norm describes. The outlet size of the wide nozzle was determined to be sufficiently larger than the train test model and achieve sufficient wind velocity within the maximum flow rate of the compact wind tunnel, and its contraction was designed by a simple equation. The developed wide nozzle was found to achieve the same flow quality as that in the reference wind tunnel in the European Norm from both simulation and experimental results. The splitter plate was applied to reduce the boundary layer thickness. The simulation results show that the higher splitter plate with a low height nozzle leads to increase the separation area from the roof of the train test model in the wake because of the lower flow rate over the roof. The splitter plate set at 0.02 times the height of the train test model was found to be suitable to achieve the target boundary layer thickness and acquire sufficient vertical space over the train model. The developed measurement system is found to measure the rolling moment around the leeside rail of the reference benchmark train model within an average 8.6 % and the maximum 14.9 % of the reference value in the European Norm for 5-degree yaw angles from 0 to 90 degrees. Thus, the proposed system can satisfy the necessary dimensions and flow specifications and accurately measure aerodynamic force and moment within the accuracy as the benchmark described in the European Norm.

Secondly, the correlation between wind velocity and aerodynamic noise level for structure with acoustical insulation was investigated to assess the similarity law for accurately estimating full-scale noise from the wind tunnel results obtained with a reduced scale model. The aerodynamic noise radiating from cylinders without and with periodic holes, and a pantograph model with and without a sound insulating plate was measured at the wind velocities above 100 m/s in a low-noise high-speed wind tunnel.

The overall noise level radiated from the cylinder is observed to increase in proportion to the sixth power of wind velocity as a dipole sound source. The noise reduction of the periodic holes, which vanish the Kármán vortex from the cylinder, is found to constantly reduce the main noise level, that is the Aeolian tone, regardless of wind velocity. However, the second peak noise radiated from the cylinder is found to become in proportion to the eighth power of wind velocity over 130 m/s, which leads to underestimate by using the wind conversion based on a dipole sound source. The overall noise level of the pantograph model with the sound insulating plate increased in proportion to lower than the sixth power of wind velocity in contrast to the pantograph model itself as a dipole sound source. This means that the sound insulating plate reduces more noise level of the pantograph noise level with the wind velocity increase. This is caused by that the sound insulating board reduces more noise level at

higher frequencies because higher-frequency sound is difficult to diffract due to its short wavelength. The frequency of the dominant pantograph noise shifts higher with the higher-speed wind velocity, and the sound insulating board becomes able to effectively reduce the dominant pantograph noise. This led to underestimate reduction effect of the sound insulating plate by 2.5dB at the estimation from 50m/s to 116.7m/s by using the wind conversion based on a dipole sound source. To solve this problem, it was formulated that the reduction noise level, which of the finite sound insulating board was theoretically estimated by using the Fresnel number, is subtracted from the estimated noise level of the pantograph itself. This leads the pantograph noise with the sound insulating plate to be estimated within 0.8 dB difference.

Finally, pressure-sensitive paint (PSP), which allows us to estimate time-series surface-pressure distributions by measuring the varying intensity of the luminescent light from the dye in PSP excited by an excitation light, was applied to complex shapes: square cylinders and simplified model of a bogie. A sound-source distribution was evaluated and an unsteady phenomenon in the low-speed region was comprehended for the development of the aerodynamic noise reduction.

The pressure fluctuations distribution on the floor surface behind a square cylinder in the turbulent boundary layer was measured by PSP and its accuracy and frequency response at the Mach number around, $M = 0.3$, were examined, where aerodynamic noise is mainly generated from the surface pressure fluctuations. Four types of the square cylinders were examined in the same turbulent boundary layer for detailed comprehension of the relationship between these conditions and the Kármán vortex shedding structure. The measured values by PSP have a similar tendency to that of the pressure transducer up to 5 kHz. The peak PSD of pressure fluctuations generated by the Kármán vortex shedding from the square cylinder was observed within an error of approximately 30 % up to more than 3 kHz.

The sounds level from a 1/8-reduced-scale simplified model of a bogie and pressure-fluctuation distributions of the bottom surface of the bogie were measured simultaneously by a microphone and an unsteady PSP, and the sound-source distribution of a bogie section of a train was clarified. A peak sound was observed at wind velocity over 69.4 m/s, and a high-pressure-fluctuation area was observed on the upstream side on the bottom surface of the bogie at the peak sound frequency. The phase-shift distribution of the pressure fluctuation shows a delay in the downstream direction regardless of wind velocity. This result shows that the propagation speed of peak pressure fluctuation was 66 % of freestream wind velocity. Thus, the measured peak sound frequency was found to be the same as the theoretical cavity peak frequency given by the Rossiter equation at this propagation speed of the peak surface pressure fluctuation. Moreover, the difference between estimated and measured sound level on the bottom surface of the bogie was no more than 3 dB, where estimated sound level was calculated from the COP data by using the Lighthill-Curle equation. Therefore, the peak sound is concluded to be mainly generated by acoustic feedback in the cavity, namely, the gap between the upstream cavity edge and the bogie.

The developed wind testing techniques and knowledges in this dissertation is expected to be applied to the improvement of the crosswind stability and reduction of the external noise at the design stage of high-speed train, which finally leads to contribute to achieve carbon neutral by supporting the development of trains with the low CO_2 emission.

Table of Contents

Chapter 1
Introduction

1.1. Research Background

One of global problems to be solved is “the global warming”. Average temperature on the Earth is rapidly rising. For example, global surface temperature was found to be 1.09 °C [0.95-1.20] higher in the 2011-2020 decade than the preindustrial baseline (1850-1900) (IPCC 2021). The current rise in global average temperature is mainly caused by greenhouse gases, especially carbon dioxide (CO_2), which result from burning fossil fuels. Greenhouse gases warm the air by absorbing heat radiated by the Earth, trapping the heat near the surface. Greenhouse gas emissions amplify this effect, causing the Earth to take in more energy from sunlight than it can radiate back into space. The global warming causes deserts expanding, permafrost melting and extreme weather (storms etc.).

The international treaty on climate change, named as the 2015 Paris Agreement (United Nations 2022), has been ratified or acceded by 193 states and the EU for prevention of the global warming. The long-term temperature goal in the Paris Agreement is to keep the rise in mean global temperature up to below the temperature 2 °C higher than pre-industrial levels, and preferably limit the increase of 1.5 °C, recognizing that this would substantially reduce the effects of climate change. Emissions should be reduced as soon as possible and reach net-zero by the middle of the 21st century. To stay below 1.5 °C of global warming, emissions need to be cut by roughly 50% by 2030.

To achieve net-zero carbon emissions, railway vehicles are drawing renewed attention as an earth-friendly transport. Figure 1.1 shows the CO_2 emissions per a passenger running 1km of intercity transport (IEA 2020). Railway vehicles generate the 1/6- and 1/10-times lower amount of CO_2 than airplane and large cars, such as trucks. Therefore, in order to reduce CO_2 in passenger and freight transport, the modal shift from road to rail has been promoted. Due to this trend, the railway market reached a record volume of EUR 188 bullion at the end of 2019, and expected to reach EUR 204 billion by 2025 with an average annual growth rate of 2.3% (UNIFE 2020). Therefore, high-speed train needs to develop to support passenger and freight transport between large cities with low CO_2 emission.

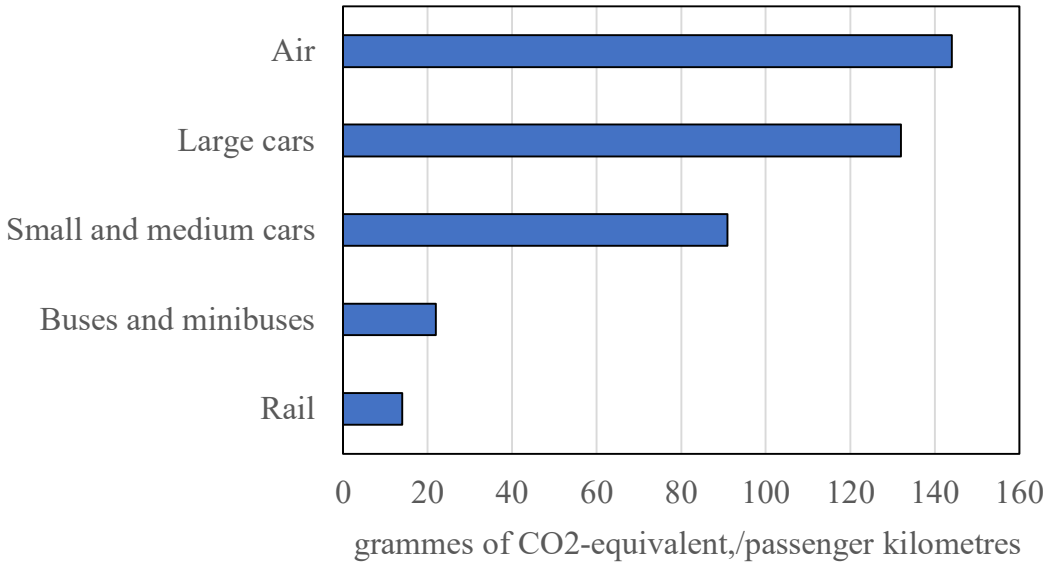

Figure 1.1 CO_2 emissions amount when a single passenger travels a single kilometer (IEA, 2020)

One of the problems on high-speed train is the crosswind stability. Train is more sensitive to crosswind than automobiles because of its larger side area. Crosswind velocity toward train increases with its running speed increase, which leads to increase the risk of overturning due to crosswind. Another problem is the external noise in high-speed running. Aerodynamic noise becomes dominant in the external noise with trains running faster because it increases in proportion to the sixth power of wind velocity. It is necessary to reduce aerodynamic noise for preventing trains from disturbing environment along railway lines.

1.1.1. Crosswind stability

Train is more sensitive to crosswind than automobiles because of its larger side area. Figure 1.2 shows the aerodynamic forces generated by crosswind. The lateral force and rolling moment under crosswind potentially cause to overturn a rolling stock. Adequate assessments of crosswind stability at design stage are being established for prevention of the overturn accidents due to crosswind. Generally, crosswind stability is assessed by using the limit wind speed, which determines the crosswind at which the rolling stock will overturn. The limit wind speed is estimated by using the dynamic response of a railway vehicle from the aerodynamic force and moment. Therefore, assessment of the aerodynamic force and moment and construction of the dynamic model are important.

In Japan, the investigations into past accidents revealed that the yaw angle β of the crosswind for a train and the environment along the railway lines, such as embankment and elevated lines, affect the aerodynamic force and moment (Suzuki et al. 2003). Hence, the infrastructure models in a turbulent boundary layer were generally adopted in the measurement of the aerodynamic force and moment in a wind tunnel in order to simulate the natural wind condition, which is illustrated in Figure 1.3, because its main target is a conventional line. The lateral force and rolling moment of the different rolling stock shape for under crosswind were measured in a wind tunnel test (Tanemoto et al. 2013). Based on these results, the flow structure around a rolling stock on the embankment under crosswind was also investigated by Computer Fluids Dynamics (CFD) (Noguchi et al. 2018, 2022). Moreover, the crosswind stability under real crosswind conditions while a train is running has been investigated. The aerodynamic force in running was calculated from the lateral surface pressure measured using moving model rig in a wind tunnel (Suzuki, 2011). The effect of real crosswind velocity and direction on the wheel unloading ratio in operational train was investigated (Moriyama 2013). The static dynamic equation for assessment of the running safety (Kunieda 1972) was generally used from the viewpoint related to the dynamic response under crosswind. Based on this equation, the detail quasi-steady equations have been adopted to add the impact of the external forces and the displacement of the car body from the knowledge of the past accidents and compared with the full-scale model tests (Hibino et al. 2009, 2013; Kikuchi and Suzuki 2015). The limit wind speed can be calculated by these equations from the estimated aerodynamic force and moment. Recently, the dynamic responses of railway vehicles under crosswinds are investigated by using multibody dynamic simulations and compared with the experimental data (Ishihara et al. 2021).

On the other hand, in the European Union, the requirements of the procedure to assess the crosswind stability have been outlined in the Locomotive and Passenger Technical Specifications for

Interoperability (TSIs) (LOC/PAS TSI 2014). A method for evaluating crosswind stability has been established on the basis of these standards in accordance with the maximum speed of the rolling stock. The main target of this requirements is the high-speed train, which runs faster than 200 km/h. These TSIs must satisfy European Norm EN14067-6:2018 (British Standard 2018), which describes a common method for determining the aerodynamic coefficients and the wheel unloading. In this standard, the coefficients of the aerodynamic forces and moments, especially the rolling moment coefficient around the lee rail, must be determined by reduced-scale wind tunnel measurements for the train running more than 200 km/h. The rolling moment coefficient around the lee rail, which is seen in Fig 1.2(b), is a non-dimensional form of a full-scale wind induced moment acting around the line of contact between the wheels and the lee rail. It is mainly this moment that unloads upwind wheels in strong winds and, at the limit, could cause a vehicle to overturn. The type of wind tunnel test that is described in this standard uses static models of the train in a uniform, low turbulence onset flow. A block profile and low turbulence intensity are usually not present in full scale; nevertheless, this is required in the wind tunnel, because it allows a more reliable and repeatable test than more complex flow simulations. A uniform velocity profile, except for the thin boundary layer on the floor, ensures more repeatable conditions between different wind tunnels. The train model is set on single track ballast and rail (STBR). The experiments under these wind tunnel conditions have been reported in the previous study (Schober et al. 2008; Rüd et al. 2009; Hoefener et al. 2009). Additionally, the aerodynamic forces and moments of the model on the flat ground and the embankments were also measured and the difference in the infrastructure was comprehended, (Bocciolone et al. 2008; Cheli et al. 2010; Tomasini et al. 2014; Li et al. 2022; Brambilla et al. 2022). Figure 1.4 shows an example of the wind tunnel test simulated as crosswind of the train on a flat ground. The limit wind speed, called as the characteristic wind speed in this standard, was calculated by the moment of equilibrium around the lee rail. In this calculation, the simple static method is usually applied because it has the built-in margins. The standard describes the characteristic wind curves, which are the table of the characteristics wind speeds at the different train speeds and wind directions, must be calculated and, be compared value by value to the ones of the reference CWC when the train running speed is over at 250 km/h. For a compliant vehicle, each compared CWC value of the assessed vehicle shall be equal to or greater than the reference values stated in the tables. Figure 1.5 shows an example of the CWCs table with the reference value for passenger vehicles and locomotives. In the previous study, the rollover risk of two types of trains; a low-speed, light-weight train and a high-speed train, was evaluated by means of the CWCs from the aerodynamic force and moment coefficients measured by means of wind tunnel tests on scale models (Giappino et al. 2016).

Generally, aerodynamic force and moment are measured in the wind tunnel with large air flow mass to apply a bigger train model. Table 1.1 shows the simplification of the reference wind tunnel described in the European Norm and our wind tunnel (Hitachi 2014; Matsui et al. 2017, 2020). The reference wind tunnel has a large fan power to acquire the large outlet with the necessary wind speed. However, few wind tunnels have such a large air flow rate, and they are difficult to use continuously for developing new train cars. The aerodynamic forces and moments under crosswind need to be measured in a compact wind tunnel with a small air flow rate for repeatable easy evaluations. In this study, the aerodynamic force and

moment measurement system have developed in our wind tunnel, the fan power of which is lower than 1/10 of that of the reference wind tunnels.

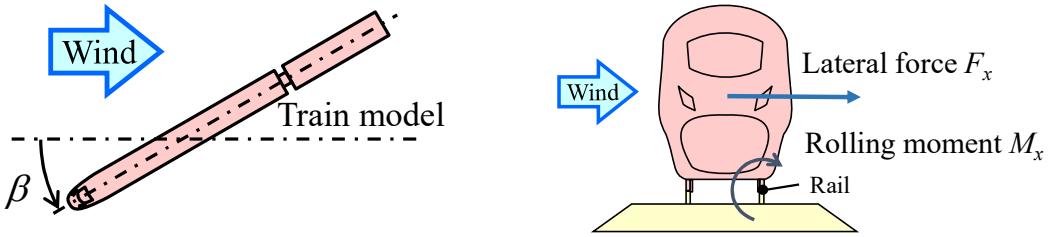

(a) Top view (b) Force and moment

Figure 1.2 The image of train under crosswind

Figure 1.3 Wind tunnel test simulating natural crosswind (Kikuchi and Suzuki, 2015)

Figure 1.4 Crosswind wind tunnel test described in the EN (Bocciolone et al., 2008)

Train speed	CWCs in m/s for angle β									
[km/h]	90°	80°	70°	60°	50°	40°	30°	20°	10°	0°
80										
100										
120										
140										
160	31.7									
180	31.0									
200	30.3									
•										
•										
250	28.6	28.3		30.3		37.7				
•										
•										

Figure 1.5 Reference CWCs for passenger vehicles running at more than 250 km/h (EN 14067-6:2018)

Table 1.1 Specification of wind tunnel

Name	Fan Power [MW]	Outlet [m]	Max wind speed [km/h]
		Width × Height	
Hitachi (Japan) Target of this research	0.32	0.6×0.4	420
CSTB* (France)	3.2	10.0×5.0	150
GVPM** (Italy)	1.4	4.0×3.84	200

*CSTB Centre Scientifique et Technique du Bâtiment
(French: Scientific Center and Technical Building)

**GVPM Politecnico di Milano Wind Tunnel laboratory

1.1.2. External noise and aerodynamic noise

External noise is defined as the sound radiated from the train. The limits of the external noise level were described in several standards and/or laws in the world to keep the silent environment along railway lines. For examples, in the Europe, the TSI (2008, 2014) describes the limits and their measurement methods. One of these noises is the pass-by noise, which is the average values when a unit of train cars running. Its limits are defined at a distance of 25 m from the centerline of the reference track, 3.5 m above the upper surface of the rails. On the other hand, in Japan, the peak noise level through the train running is required in the Japanese law (Ministry of the Environment 1993). Its limits are measured at a distance of 25 m from the centerline of the elevated bridge track. In the development of a new line and/or new train cars, its external noise must be assessed so that the limits of the noise level are satisfied.

Figure 1.6 shows the breakdown of the external noise level (EC 2003). External noise is classified as three noise sources: Traction noise, rolling noise and aerodynamic noise. Traction noise is generated from the equipment set on/under a train at their operating. It is basically independent on the train running speed, and becomes a main noise source at the train stopping. Rolling noise is generated by the vibration of the wheel and rail induced by the interaction force generated due to the irregularities present in their surfaces. It is found to increase in the proportion to the third power of the running speed (Mellet et al., 2006, Thompson, 2010). Aerodynamic noise is generated by the running wind blowing to parts of a train. Aerodynamic noise is observed to increase in proportion to the fifth to eighth power of the wind velocity from the measurement of the running train cars in operation (Thompson et al. 2015; Sica et al. 2021). Therefore, the main noise source of the external noise of the rolling noise is shifted from the rolling noise to the aerodynamic noise as the running speed increases, which is illustrated in the Fig. 1.6. The aerodynamic noise needs to be reduced because it becomes dominant for a high-speed train.

It is important for reduction the external noise to detect the noise source position and investigate the adequate shape. In the previous study, the external noise source position of high-speed train was investigated from the measurement of a running train by using a microphone array (Takano et al. 2003; Kurita et al. 2011). Figure 1.7 shows an example of the microphone array measurement result. These results illustrate that the external noise of Shinkansen was found to be mainly radiated from the bogie region and the pantograph on its roof. Noise from the bogie region is found to be mixed with the rolling noise and the aerodynamic noise, which is generated by that the running wind flows into the bogie cavity and hit the bogie and the car body (Kitagawa et al. 2013; Yamazaki et al. 2019a). The bogie side and bottom covers and the lower shape near the bogie cavity were optimized to reduce the aerodynamic noise by preventing the wind flowing into the bogie cavity (Uda et al. 2016; Sawamura et al. 2019) and applied to be embed sound-absorbing materials in them to prevent the noise from the bogie region propagating to the outside (Kurita, 2011). The pantograph generated the aerodynamic noise by receiving the high-speed running wind due to its location on the roof. In previous study, the shape of the pantograph was optimized for aerodynamic noise reduction to adjust for the current collecting performance and the distance between train roof and a catenary (Kurita et al. 2010; Saito et al. 2019). Especially, the panhead shape, which contacts the catenary for collection current, was found to be one of the noise sources and optimized to reduce the aerodynamic noise and acquire the adequate the uplift force (Mitsumoji et al.

2019). In addition to the shape optimization of the pantograph itself, the control of the propagation of the aerodynamic noise radiated from the pantograph has been investigated. The sound insulating boards were applied to be set on the side of the pantograph on the roof to prevent the radiation to the wayside of the railway line (Kanda et al. 2008; Kurita et al. 2010).

The wind tunnel tests have been conducted for repeatable evaluations because full-scale tests require enormous cost and time, and these reduction methods for the aerodynamic noise were investigated. We measure the radiated aerodynamic noise of a reduced scale model in a wind tunnel and estimate the full-scale noise from the test result by using a similarity law of aerodynamic noise. Therefore, the similarity law is important for accurately estimating full-scale noise from the results obtained with a reduced scale model. The law needs to convert the noise spectrum of a reduced scale model in a wind tunnel into that of a full-scale one by taking the difference between the wind velocity, the scale and the measurement conditions of the two models into consideration. Iida et al. (2000, 2007) suggested the use of the law for aerodynamic sound generation which estimates full-scale model noise in the condition of the low Mach number. In this similarity law, the sound pressure level *SPL* is in proportion to the sixth power of wind velocity and to the double power of the scale from the sound pressure of a reduced-scale model. However, next generation high-speed trains are expected to run faster, which will probably lead to full-scale estimated noise error because of the change of the noise source on trains or the difference in wind velocity between reduced-scale and full-scale models. In this study, the change in the similarity law by increasing the wind velocity was assessed to increase the accuracy of the full-scale noise level estimation.

Moreover, detection of the aerodynamic noise source is also important to investigate the noise reduction. The Lighthill-Curle equations (Lighthill 1952; Curle 1955) show that a sound source of aerodynamic noise is changed from a dipole sound source into a quadrupole sound source depending on the Mach number M ($= U/a$), which is the ratio between the freestream velocity U and the sound velocity a. Aerodynamic noise is found to be mainly generated as a dipole sound source from pressure fluctuations on a surface in the low-speed region under $M = 0.3$ (Iida et al. 2000). Therefore, it is important to measure distributions of surface-pressure fluctuation on a test model for the assessment and the detection of aerodynamic noise sources. Conventionally, pressure fluctuations are measured by using pressure sensors set in orifices on a surface of a test model. This measurement technique is highly accurate and reliable. However, it is difficult to be applied to a curved surface, and to acquire the pressure distribution across a whole surface, multiple sensors and/or repeated measurements are necessary. Therefore, it is required to easily measure the surface pressure fluctuation distribution. In this study, pressure-sensitive paint (PSP) was investigated for the application to detect noise source and estimate its noise level.

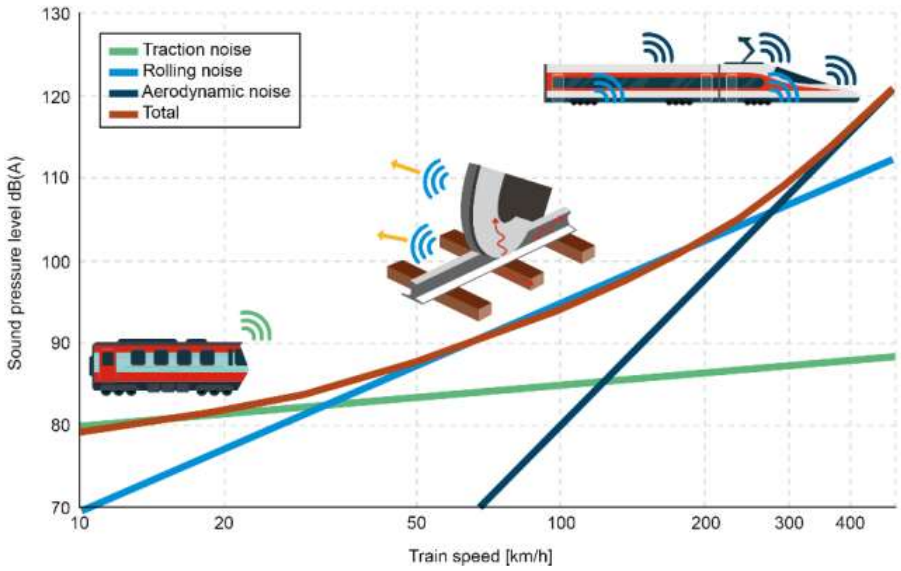

Figure 1.6 Breakdown of the external noise level (EC, 2003)

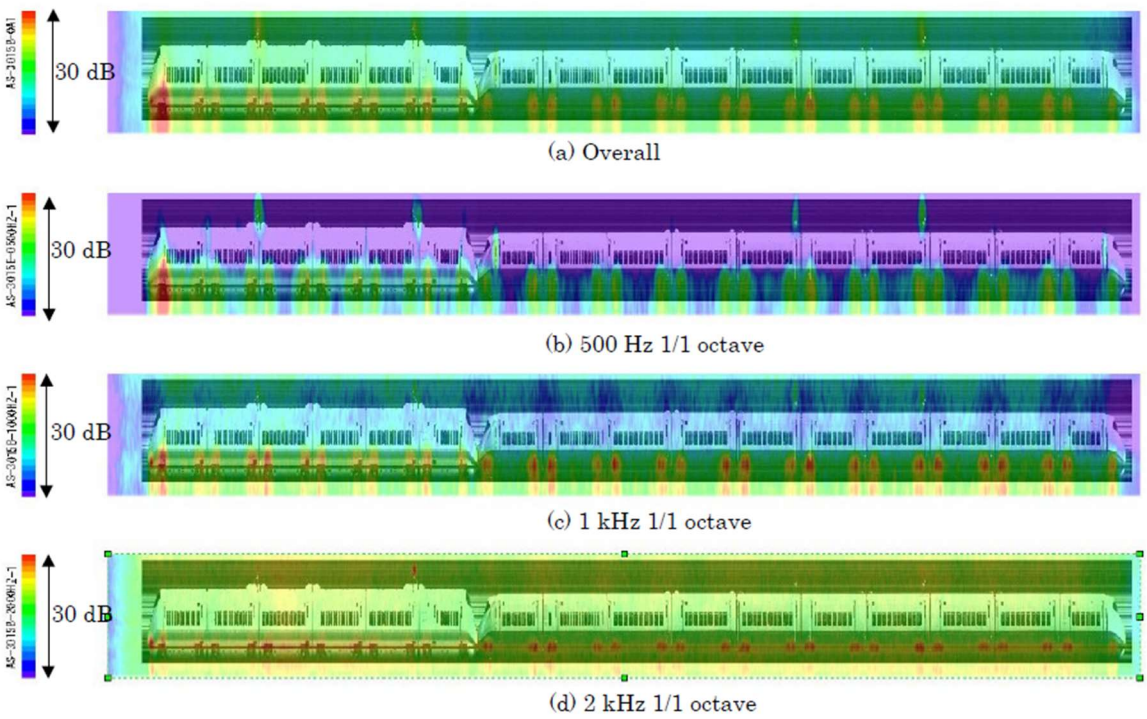

Figure 1.7 Sound level distribution of the Shinkansen measured by a microphone array (Takano et al. 2003)

1.1.3. Pressure sensitive paint

Pressure-sensitive paint (PSP) has been developed as a new method by which to measure pressure fields with high spatial resolution (Bell et al. 2001; Liu and Sullivan 2005). PSP is an optical pressure-measurement technique based on oxygen quenching of luminescence.

Figure 1.8 shows the schematic of the PSP coating and a measurement system. PSP consists of oxygen sensing molecules (luminophore), an oxygen-permeable binder, and a solvent. In general, PSP can be applied to a test article by spray coating procedure. Luminophore is excited from the most stable (ground) state to excited electronic states by a light with a proper wavelength. The excited molecules return to the ground state by a combination of radiative and radiationless processes. The radiative process is accompanied by a light emission, whereas the radiationless process including oxygen quenching is accompanied by energy dissipation by a collision with another molecule or vibration of the molecule. Hence, the characteristics of light, i.e., intensity emitted from the PSP layer depends on the oxygen concentration in the PSP layer. Since the oxygen concentration in a layer is proportional to the oxygen partial pressure according to Henry's law, the air pressure over the PSP coating can be calculated from the measured luminescence characteristics. Cameras are typically used as a photodetector of the PSP emission.

One of the measurement methods to obtain pressure information using PSP is the intensity-based method that is based on the relation of the luminescent intensity to air pressure. The intensity-based method is widely used in wind-tunnel tests because of the simple experimental setup and the high luminescent intensity. Continuous excitation light sources and a photodetector such as a digital camera were used in the intensity-based method. Since the emission intensity of PSP depends not only on air pressure but also on the dye concentration, the paint thickness, and the intensity of an excitation light, the ratio of a wind-on (run) and wind-off (reference) images is used to calculate pressure.

The high-spatial-resolution pressure information provided by PSP enables understanding of aerodynamics on locations where conventional pressure taps and transducers cannot be installed, such as sharp edges, corners, thin or small models, and rotating surfaces. In addition, the aerodynamic force acting on a test article can be calculated by integrating surface pressure measured by PSP. It is important for the validation of CFD simulations to use high-resolution experimental data.

PSP has been applied to the unsteady measurements in the transonic and supersonic flows since the development of the fast-response PSP and the high-speed cameras with high resolution. Nakaktia et al. (2012) successfully revealed the complex three-dimensional flow field on the rocket fairing by the using PSP, of which the time-series pressure data were agreed well with those acquired by unsteady pressure transducers. Sellers et al. (2017) conducted unsteady PSP measurement of a generic launch vehicle. Figure 1.7b shows the root-mean-square pressure fluctuations on the model measured by the unsteady PSP technique. They finally calculated fluctuating integrated loads acting on the launch vehicle model.

In recent years, moreover, PSP has been applied to unsteady phenomena in the low-speed region (Liu 2003; Asai and Yorita 2011; Nakakita 2011; Peng et al. 2016). Applying PSP to unsteady phenomena in the low-speed range faces two major problems: time response of PSP and low signal-to-noise ratio (SNR) due to low dynamic pressure. Regarding the former problem, unsteady PSP has been

developed, and PSPs with quick response time, which can adequately follow pressure fluctuation in the order of kilohertz (Gregory et al. 2001; Kitashima et al. 2014; Sugioka et al. 2018, 2018a, 2018b, 2021; Uchida et al. 2021) have been demonstrated. Regarding the latter problem, several methods for improving SNR of PSP have been developed. A simple one is a phase-lock measurement that accumulates synchronized snapshots with a reference signal out of the targeted periodic phenomenon. A fast Fourier transform (FFT) was applied to PSP images (Nakakita 2011), and subtracting power spectral density (PSD) of the wind-off images from that of the wind-on images is shown to be an effective way to reduce the noise component (Nakakita 2013). Recently, the spectrum estimation technique using cross-corelation was also devised and the noise floor was further reduced while it requires a lot of samples (Ozawa at al. 2019). Meanwhile, coherent output power (COP), which is given by a cross correlation between time-series pressure measured by PSP and a reference signal, was employed for the measurement of pressure fluctuations associated with tonal trailing-edge noise for a two-dimensional NACA 0012 airfoil (Noda et al. 2018). Accuracy of an unsteady PSP measurement in the low-speed region has thus been improved. However, there are still few examples of applying a PSP measurement to a complex shape for evaluation of a sound-source distribution and for comprehension of an unsteady phenomenon in the low-speed region.

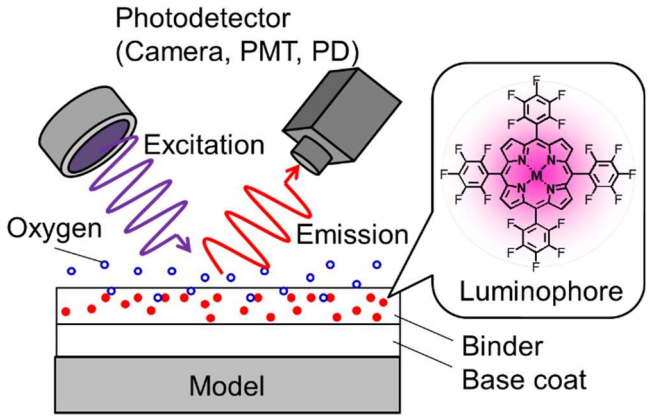

Figure. 1.8 Schematic illustration of pressure-sensitive paint and measurement system.

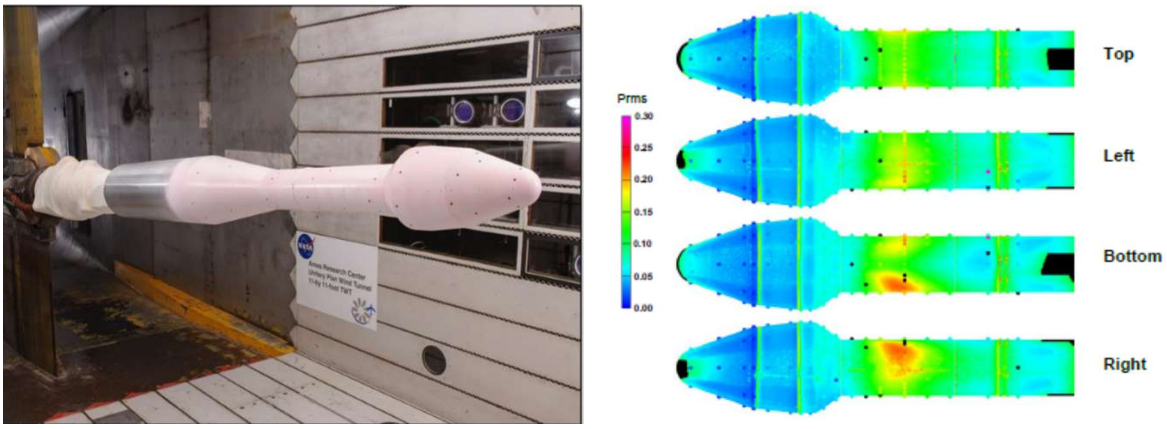

(a) Launch vehicle model coated with PSP **(b)** RMS distribution at $M = 0.8$

Figure. 1.9 Unsteady PSP measurement on a launch vehicle model (Sellers et al. 2017).

1.2. Contributions and Outline

In the present dissertation, the innovative wind tunnel testing techniques were developed in order to assess the crosswind stability and evaluate the aerodynamic noise with noise source detection for the development of the high-speed train with the low CO_2 emission.

In Chapter 2, the aerodynamic force and moment measurement system was developed in a compact wind tunnel for repeatable easy evaluations of the crosswind stability. The aim of the measurement system is to accurately measure aerodynamic force and moment within a required tolerance of the benchmark data listed in the European Norm. A wide nozzle which is a suitable size for the reduced-scale train model was developed for effective use of the limited air flow rate. Moreover, the train model installation setup is optimized, and a sufficient flow is obtained while controlling the boundary layer thickness.

In Chapter 3, the correlation between wind velocity and aerodynamic noise level for structure with acoustical insulation was investigated and the similarity law for accurately estimating full-scale noise from the results obtained with a reduced scale model was evaluated. The aerodynamic noise that radiates from cylinders with and without periodic holes and a reduced-scale pantograph model with and without a sound insulating plate, which are generally used for suppression of noise from high-speed trains, are measured in a low-noise high-speed wind tunnel.

In Chapter 4, pressure-sensitive paint (PSP) was applied to the measurement of the pressure fluctuations distribution on the floor surface behind a square cylinder and the frequency response and accuracy of measured values of PSP in the low-speed region were examined. Four types of the square cylinders were examined in the same turbulent boundary layer. The impact from the difference of the square cylinder aspects to the peak frequencies and distribution of the pressure fluctuations generated by the Kármán vortex from the square cylinder was examined. The main mode of the peak pressure fluctuations distribution was calculated by the singular value decomposition.

In Chapter 5, the PSP, which was verified for measurement in the low-speed region in Chapter 4, was applied to a bogie section of a railway vehicle to evaluate a sound-source distribution and comprehend an unsteady phenomenon for the development of the aerodynamic noise reduction. The sound level from a 1/8-reduced-scale simplified model and pressure-fluctuation distribution of the bottom surface of the bogie were measured simultaneously by a microphone and PSP, and the sound-source distribution from the bogie section was discussed. The sound level at the bottom surface of the bogie was estimated from the pressure data measured by PSP with the measured sound pressure, by using the Lighthill-Curle equation.

The present study is concluded in Chapter 6 by giving the summary of the result in each chapter and an outlook for future work.

Chapter 2
Aerodynamic Force and Moment Measurement for Crosswind Stability Assessment in a Compact Wind Tunnel

List of symbols

A_0 Reference normalization area [m^2] (=10 m^2)

A_r Required outlet area [m^2]

A_s Reduced-scale train projected area against outlet nozzle at the yaw angle β = 30 degrees [m^2]

A_t Actual train projected area against outlet nozzle at the yaw angle β = 30 degrees [m^2]

C_{Fx} Side force coefficient [-]

C_{Fz} Uplift force coefficient [-]

C_{Mx} Rolling moment coefficient [-]

$C_{Mx,lee}$ Rolling moment coefficient around leeward rail [-]

D_I Nozzle inlet dimension [m]

D_O Nozzle outlet dimension [m]

F_x Side force [N]

F_z Uplift force [N]

L Nozzle length [m]

M_r Required air flow rate [m^3/s]

M_z Rolling moment [Nm]

$R(x)$ Shape outline of nozzle curve [mm]

Re Reynolds number based on the reduce-scale reference length d_{0s} [-]

Re_r Required Reynolds number [-]

Tu_x Turbulent intensity [-]

U Mean flow velocity [m/s]

U_r Required flow velocity [m/s]

W Outlet width [m]

W_r Required outlet width [m]

$2b_0$ Nominal lateral distance [m] (= 1.5 m)

d_0 Reference normalization length [m] (= 3 m)

d_{0s} Reduced-scale reference normalization length [m]

f_{BL} Blockage correction factor

h_s Reduced-scale train model height [m]

h_{sp} Splitter plate height [m]

h_t Actual train model height [m]

l_s Reduced-scale train model length [m]

l_t Actual train model length [m]

s Train model scale [-]

u Streamwise flow velocity [m/s]

x Streamwise position from the nozzle outlet[m]

x_b Blockage ratio at yaw angle β = 30 degrees [%]

x_{br} Required blockage ratio at yaw angle $\beta = 30$ degrees [%]

x_i Inflection point [m]

y Height position from the bottom of the nozzle outlet [m]

z Width position from the center of the nozzle [m]

β Yaw angle [degrees]

ε_{max} Max tolerance target value [-]

ε_{mean} Mean tolerance target value [-]

$\delta_{99\%}$ Boundary layer thickness [mm]

ρ Air density [kg/m3]

ν Kinematic viscosity coefficient [m^2/s]

2.1. Introduction

A train car is more sensitive to crosswind than automobiles because of its larger side area. Crosswind significantly affects the running safety and has even caused a train car to overturn (Diedrichs 2005). Currently, a rolling stock needs to be speeded up to shorten delivery times and to be lightened to save energy, and thus, increasing the risk of overturning due to crosswind. On the basis of this risk, adequate assessments of crosswind stability are being established.

Generally, crosswind stability is assessed by using the limit wind speed, which determines the crosswind at which the rolling stock will overturn. The limit wind speed is estimated by using the dynamic response of a railway vehicle from the aerodynamic force and moment (Hibino et al. 2009; LOC/PAS TSI 2014). In Japan, investigations into past accidents revealed that the yaw angle of the crosswind for a train and the environment along the railway lines, such as embankment and elevated lines, affect the aerodynamic force and moment (Suzuki et al. 2003). Moreover, the crosswind stability under real crosswind conditions while a train is running has been investigated (Suzuki 2011). In addition, in the European Union, the latest requirements of the procedure to assess the crosswind stability have been outlined in the Locomotive and Passenger Technical Specifications for Interoperability (TSIs) (LOC/PAS TSI 2014). A method evaluating crosswind stability has been established on the basis of these standards in accordance with the maximum speed of the rolling stock. These TSIs must satisfy European Norm EN14067-6:2010 (British Standard 2010), which describes a common method for determining the aerodynamic coefficients and the wheel unloading.

According to the European Norm, for high-speed trains, aerodynamic force and moment coefficients under crosswind need to be measured in a wind tunnel that meets the specifications in the Norm, such as flow quality and equipment requirements. The European wind tunnels, in which the measured aerodynamic force and moment were described as the reference value in the European Norm, have a sufficient air flow rate and a large-scale train model while satisfying the width/height ratio. For example, the Politecnico di Milano Wind Tunnel (Politecnico di Milano 2022), which was one of the reference wind tunnels, has 4×3.84 m^2 test section with 55 m/s, which means air flow is over 800 m^3/s, and 1/10 reduced-scale model for crosswind assessment (Rocchi et al. 2011). However, few wind tunnels have such a large air flow rate, and they are difficult to use continuously for developing new rolling stock. The aerodynamic forces and moments under crosswind need to be measured in a compact wind tunnel with a small air flow rate for repeatable easy evaluations.

One problem of using a compact wind tunnel is that the small air flow rate limits the measurement area and the wind velocity, which is thought to lead to the flow around the train model of the reference wind tunnel not being simulated. Furthermore, the small measurement area makes the train model smaller when acquiring a sufficient blockage ratio of the train model for the tunnel area, which deteriorates the measurement accuracy. Additionally, the slow velocity causes an insufficient Reynolds number. Therefore, a limited air flow rate must be effectively used when precisely measuring a crosswind effect in a compact wind tunnel. In particular, flow from the outlet nozzle must be the required quality, and flow simulated around the train model must be the same as that in the reference wind tunnel. An adequate nozzle for the train model and boundary layer control need to be developed for acquisition of this flow.

In this study, we developed a measurement system in our own high-speed low-noise wind tunnel, the airflow of which is lower than 1/10 of that of the reference wind tunnels. The aim of the measurement system is to accurately measure aerodynamic force and moment within a required tolerance of the benchmark data listed in the European Norm. To effectively use the limited air flow rate, a wide nozzle is developed that is a suitable size for the reduced-scale train model. Moreover, the train model installation setup is optimized, and a sufficient flow is obtained while controlling the boundary layer thickness.

2.2. Measurement System Design

2.2.1. Measurement System Outline

Figure 2.1 shows the outline of the proposed aerodynamic force and moment measurement system, and Table 2.1 lists the target specifications to meet the EN requirements. To blow the wind to a train model set transversely to the wind direction and measure the aerodynamic force and moment to assess crosswind stability, a sufficient flow outlet area and flow speed for the train model need to be acquired. In this research, a leading car was targeted for measurement because it directly receives crosswind. Referring to the EN, we set the target width of the outlet area to over 4/3 the reduced-scaled train model length l_s and the target blockage ratio $x_b(=A_s/WH)$, which is the ratio of reduced-scale train projected area against outlet nozzle, A_s, to the outlet nozzle area, to less than 15% at the yaw angle $\beta = 30$ degrees, which is the angle between the train model and the mainstream direction. Furthermore, the air flow must be the same quality as that in the reference wind tunnel for maintaining the measurement precision. We set the target Reynolds number $\mathrm{Re}(=Usd_0/\nu)$ based on the reduced-scale reference length $d_{0s}(=sd_0)$ to more than 2.5×10^5 and the target boundary layer thickness $\delta_{99\%}$ at the model set position to 30% of the reduced-scale train model height hs. The wide nozzle and boundary layer control which enables us to maintain these target values were developed

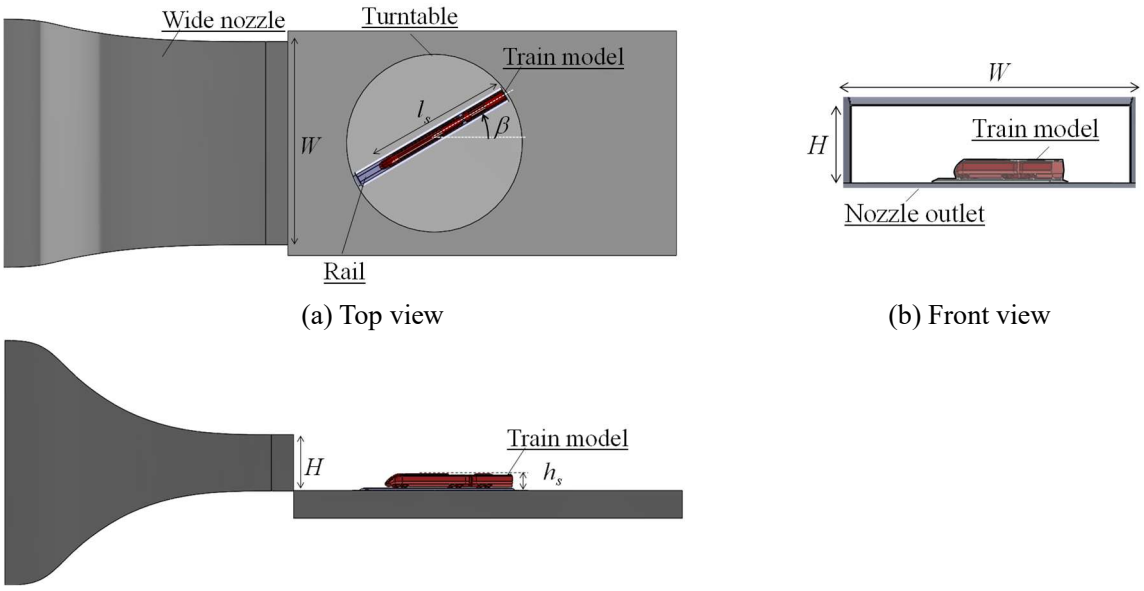

(a) Top view

(b) Front view

(c) Side view

Figure 2.1 Measurement system overview

Table 2.1 Target values

Specifications	Value
Outlet width W [m]	over $\frac{4}{3}l_s$
Blockage ratio x_b [%]	under 15
Reynolds number Re [-]	over 2.5×10^5
Boundary layer thickness $\delta_{99\%}$ [m]	under $0.3h_s$

2.2.2. Wide Nozzle Design

2.2.2.1. Determination of outlet area

The air outlet area size must be determined for the development of the wide nozzle. The air outlet area needs to have an outlet width W over 4/3 the reduced-scaled train model length l_s and a blockage ratio x_b lower than the required blockage ratio x_{br} = 15% at the yaw angle β = 30 degrees. Moreover, the flow velocity U, which is determined by the flow outlet size and the fan power of this wind tunnel, must satisfy the required Reynolds number Re_r based on the reduced-scale reference length d_{0s}. Since each specification depends on the train model scale s, we determine the train model scale s so as to meet the requirements for this wind tunnel.

Table 2.2 shows the specifications estimated from the train model scale s. According to the EN, the train model must have a test vehicle and at least half a vehicle downstream. In this research, a TGV Duplex powercar, which is one of wind tunnel benchmark vehicle models defined in the EN, was used. It has height h_t = 3.9 m and was set the length l_t = 37.5 m, generally the train vehicle length is approximately 25 m. At these dimensions, the required outlet width W_r, the required outlet area A_r, and the required wind velocity U_r , which satisfy the Reynolds number, are estimated from the target values at each train model scale: s = 1/20, 1/30, and 1/40. Moreover, the required air flow rate M_r is also estimated by using the required outlet area A_r and flow velocity U_r for the estimation of the fan power. These specifications are acquired from the actual train projected area at the yaw angle β = 30 degrees, A_t, which was measured by the 3D-CAD, and the kinematic viscosity coefficient ν by equations (2.1) - (2.4). Table 2 presents that the smaller train model scale s decreases the required air flow rate M_r. Since the maximum air flow rate of our wind tunnel with the high-speed original nozzle is estimated to be 28 m^3/s, the train model scale s that satisfies the specifications in this wind tunnel is found to be lower than 1/20. On the other hand, the larger train model scale s increases the aerodynamic force and moment at the measurement and improves the measurement accuracy, which leads to the train model scale s being determined to be s = 1/30. If the train model scale is s = 1/30, the target outlet width W is more than 1.7 m, the target outlet area A is over 0.52 m^2, and the target wind velocity V is over 37.5 m/s. The nozzle outlet size is determined to have the width W = 1.8 m and the height H = 0.5 m and the margin for satisfying these specifications are widened.

$$W_r = \frac{4}{3} s l_t \tag{2.1}$$

$$A_r = \frac{A_s}{0.15} = \frac{s^2 A_t}{0.15} \tag{2.2}$$

$$U_r = Re_r \frac{\nu}{d_0 s} \cong \frac{5}{4s} \tag{2.3}$$

$$M_r = A_r U_r \tag{2.4}$$

Table 2.2 Required specifications estimated from train model scale *s*

Train model scale *s* [-]	1/20	1/30	1/40
Required nozzle outlet width W_r [m]	2.3	1.5	1.1
Required nozzle outlet area A_r [m^2]	1.17	0.52	0.29
Required wind velocity U_r [m/s]	25	37.5	50
Required air flow rate M_r [m^3/s]	29	19	15

2.2.2.2. Nozzle shape design

Adequate contraction is required for the uniformity of flow velocity distribution. Here, the nozzle curve, such as the change in dimensions from the inlet area to the outlet area, is designed with reference to the shape supposed by Rouse and Hassan (1949). This shape shows the relationship of the contraction ratio and nozzle curve for the cavitation-free profile at the outlet and was adapted to the wind tunnel nozzle design for preventing local pressure drop at the outlet by Kobayashi (1981). The general shape is designed as the following equations. The shape outline of the nozzle curve $R(x)$ from the center of the wind tunnel at the streamwise position x, of which the origin is the outlet, is acquired from the inlet dimension D_I, the outlet dimension D_O, the nozzle length L, and inflection point x_i/L, which are shown is equations (2.5) and (2.6). In this research, the inlet width and height are $D_{I,width} = D_{I,height} = 0.42L$ and the outlet width and height are $D_{O,width} = 0.35L$ ($=W/2$) and $D_{O,height} = 0.10L$($= H/2$).The origin of the coordinates system is the center of the outlet.

$$R(x) = \frac{D_I}{2} - \left(\frac{D_I - D_O}{2}\right)\frac{(1 + x/L)^3}{(x_i/L)^2} \qquad \left(-1 \le \frac{x}{L} \le \frac{x_i}{L} - 1\right) \tag{2.5}$$

$$R(x) = \frac{D_O}{2} - \left(\frac{D_I - D_O}{2}\right)\frac{(x/L)^3}{(1 - x_i/L)^2} \qquad \left(\frac{x_i}{L} - 1 \le \frac{x}{L} \le 0\right) \tag{2.6}$$

A suitable shape is easily designed by changing the inflection point. Figure 2.2 shows the inflection point of this research in the cavitation-free design profile (Rouse and Hassan 1949), and Figure 2.3 shows the designed nozzle curve. In the references, in order to generate a local pressure drop near the outlet, the max inflection point was limited from the contraction ratio from the outlet size to the inlet size and the

ratio from the inlet size to the nozzle length. In this research, the contraction ratio is ($D_{I,width}$ $D_{I,height}$)/($D_{O,width}$ $D_{O,height}$) = 2.3 and the ratio from the inlet size to the nozzle length is $L/2D_{I,width} = L/2D_{I,height}$ = 1.2, which decides the inflection point less than x_i/L = 0.27 in the shape supposed for cavitation-free profile as shown in Figure 2.2. Smaller inflection point makes the rapid curvature of the nozzle shape near the inlet, and may make pressure increasing area and cause the boundary separation. Therefore, for the uniformity of the velocity distribution without separation, the inflection point x_i is set at 0.2 of the nozzle length L from the inlet, and the curves are set to straighten close to the nozzle outlet.

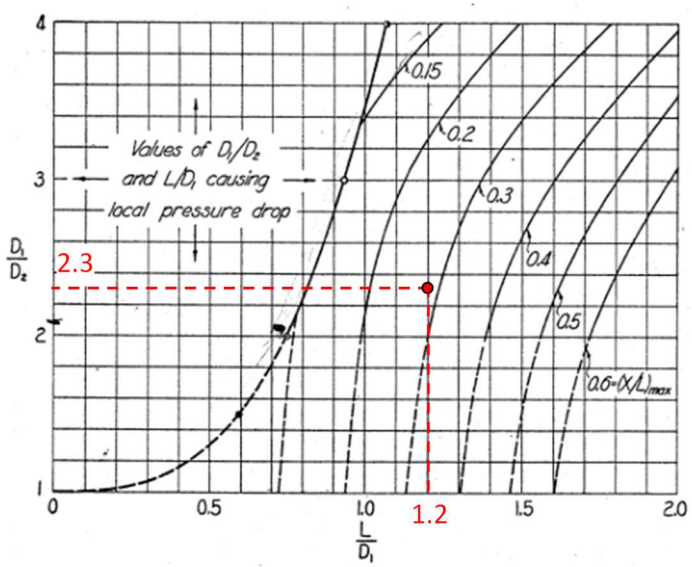

Figure 2.2 Inflection point of this research and the conditions of cavitation-free design from the reference (Rouse and Hassan 1949)

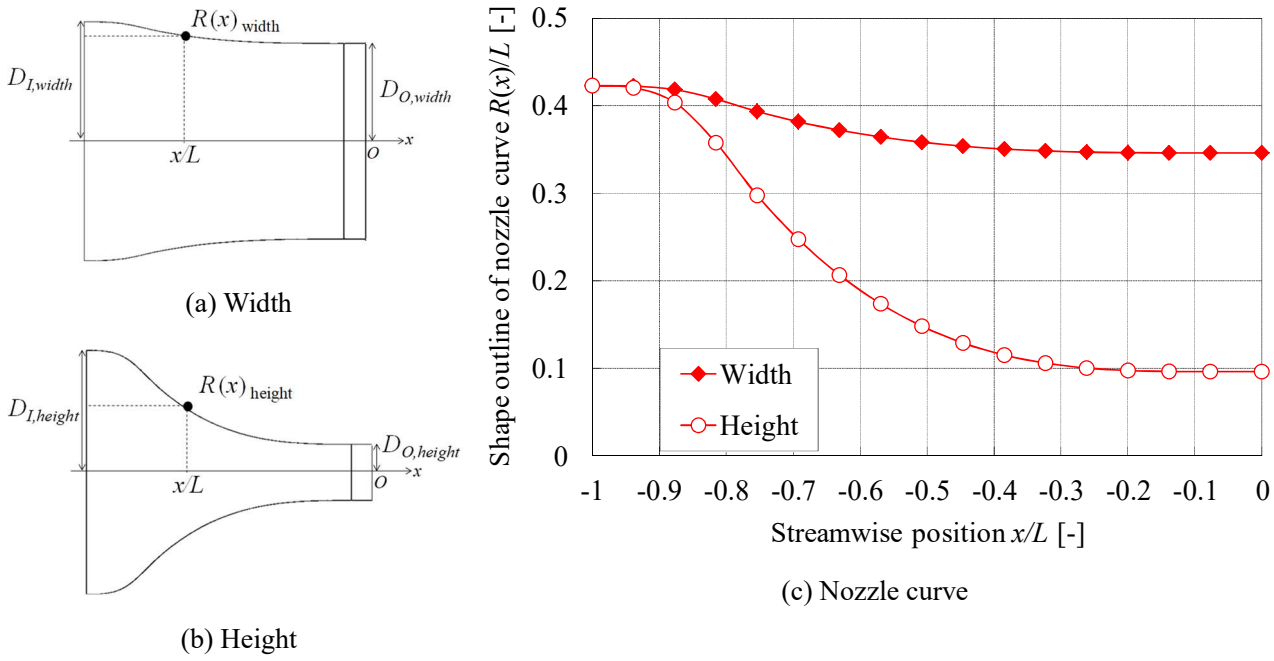

Figure 2.3 Shape outline of wide nozzle curve

The flow generated by a wide nozzle is simulated by the software Star-CCM+, and the uniformity of the velocity distribution from the designed wide nozzle is checked. Table 2.3 indicates the simulation conditions, and Figures 2.4 and 2.5 show the simulation domain and mesh, including the designed wide nozzle, ground plate, and collectors. Figure 2.6 shows the velocity contour map in the horizontal cross-section at the nozzle center and velocity distribution in the model set position. The origin of the coordinate system is at the center of the nozzle outlet bottom. We set conditions under which the air flow rate is 35 m^3/s at the wide nozzle inlet and outlet at the collector, and simulate the wind flowing through the wide nozzle to the collector. The air flow rate is estimated from the fan power and the pressure resistance, because the wide nozzle reduces the pressure resistance at the nozzle and increases the available air mass flow from the original high-speed nozzle by its larger outlet area. The results reveal that the mean wind speed is U/U_r =1.04, which exceeds the required wind velocity U_r =37.5 m/s estimated by using the Reynolds number. Moreover, the constant mainstream speed range was 88 % of the nozzle width W, at the model set position (the streamwise position x/L = 0.46). This shows that the developed wide nozzle satisfies the uniformity of the flow velocity. This figure also shows the measured values, the measuring method of which is described in chapter 2.3.1, and the simulated results are in good agreement with experimental results.

Table 2.3 Simulation conditions

Turbulence model	・Steady ・RANS (Reynolds Averaged Navier-Stokes Simulation)
Inlet condition	35 m^3/s
Outlet condition	Pressure outlet boundary
Mesh	Trim mesh
Number of elements	32,090,638

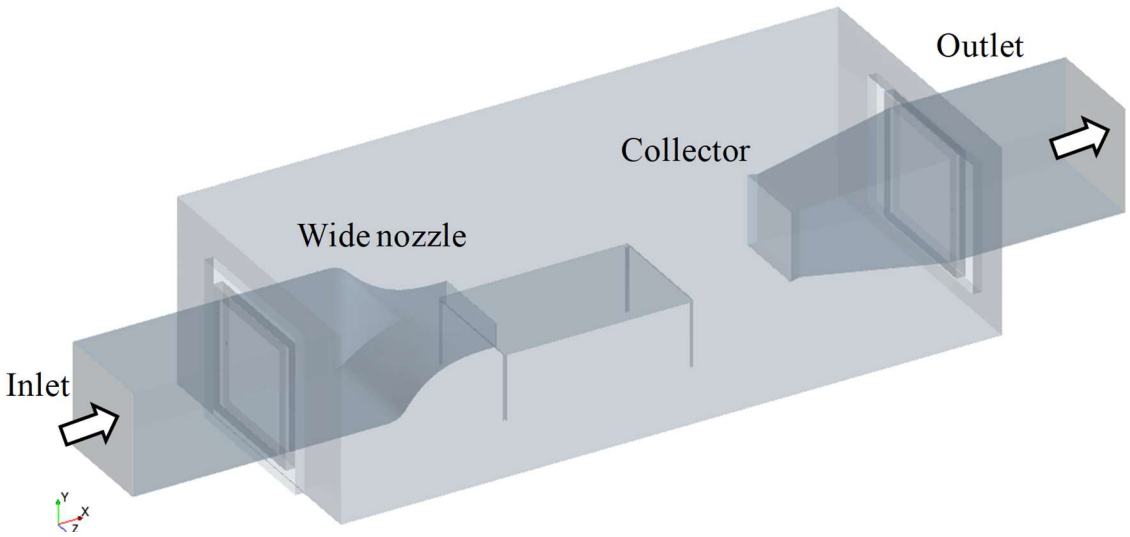

Figure 2.4 Simulation domain, including designed wide nozzle, ground plate, and collectors.

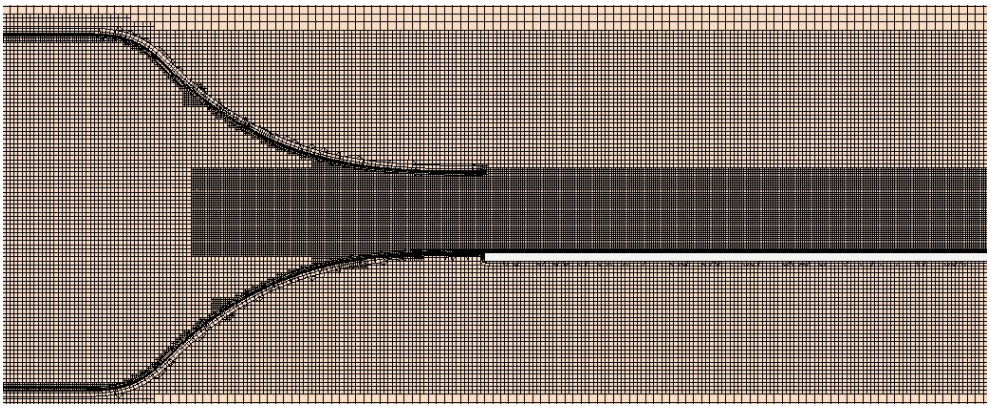

Figure. 2.5 Simulation mesh at the center plane.

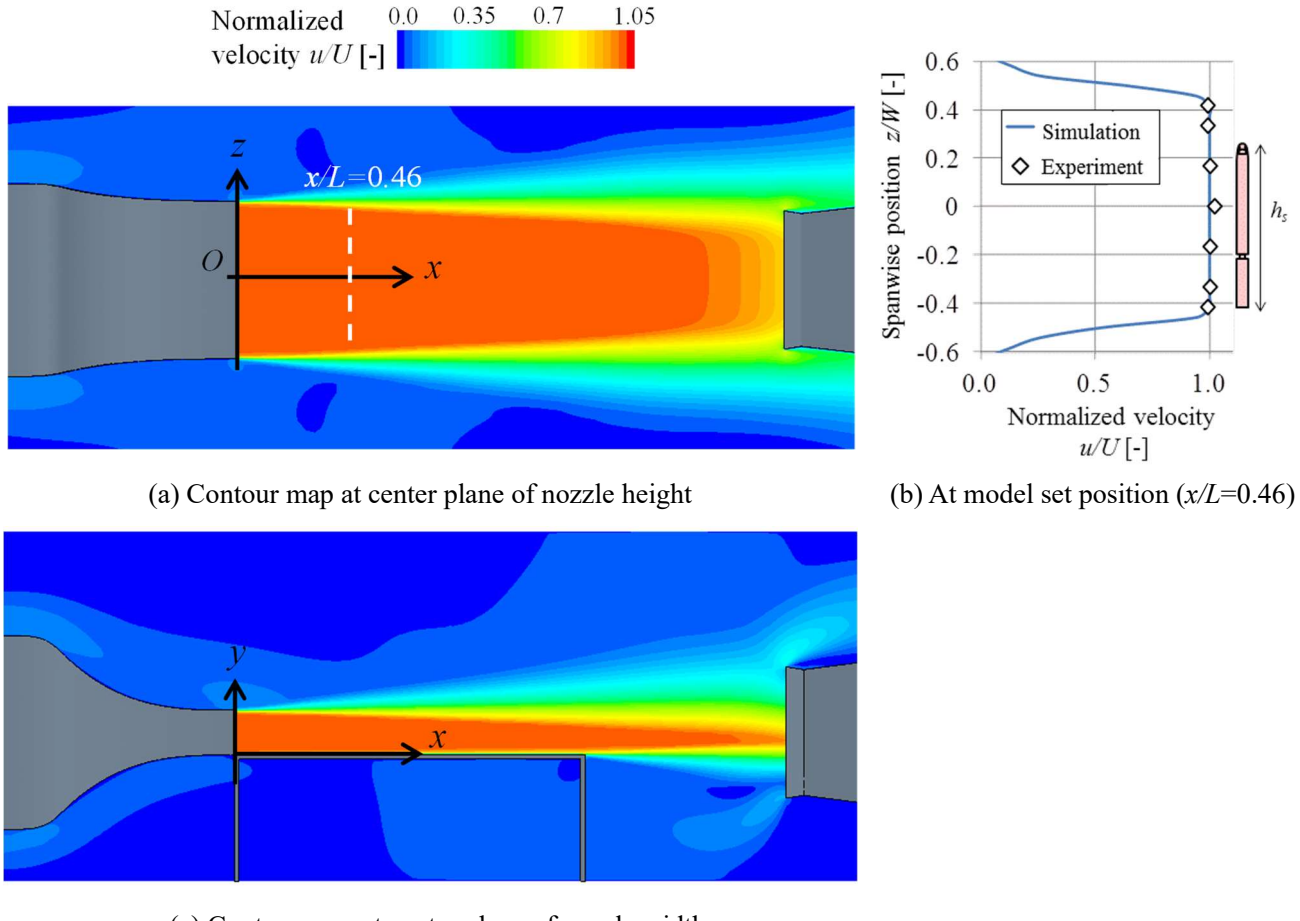

(a) Contour map at center plane of nozzle height

(b) At model set position (x/L=0.46)

(c) Contour map at center plane of nozzle width

Figure 2.6 Simulation results for velocity distribution.

2.2.3. Optimization of Model Installation

It is also important to consider boundary layer thickness $\delta_{99\%}$ of the velocity profile for accurate measurements of forces and moments. Because the boundary layer thickness $\delta_{99\%}$ at the model setup is simulated to be $\delta_{99\%}/h_s$=0.31, which is over the required boundary layer thickness $\delta_{99\%}/h_s$=0.3, the boundary layer control is necessary. Here, the splitter plate is installed under the train model because the boundary layer thickness is easily controlled by changing the splitter plate height h_{sp}. In this research, the splitter plate is a rounded rectangular shape, the size of which is 1,780 mm × 1,080 mm, and the distance from the leading edge to the train model is set constant. Its shape at the leading edge was rounded and its thickness was 5 mm.

The splitter plate height h_{sp} must be made higher for reduction in the boundary-layer thickness. Here, however, the splitter plate height h_{sp} is limited because the height of the wide nozzle is too low for the train model due to the limitation of fan power. Therefore, we investigate the effect of the splitter plate height in the developed wide nozzle for the velocity distribution around the train model in the simulation. The simulation conditions are the same as those in Table 2.3, except that the splitter plate and the train model at the yaw angle β = 90 degrees are set on the ground plate. The splitter plate heights of h_{sp}/H = 1/12.5 and 1/50 are chosen and the effects of different splitter plate heights for the flow structure around the train model are investigated. The former is the height assuming a quite thin boundary layer, and the latter is the lowest height at which the target boundary layer thickness can be satisfied.

Figure 2.7 shows the streamwise velocity contour map in the vertical cross-section at the train model center and the velocity distribution at the streamwise position x/L=0.58(the train model setup position is x/L = 0.46). At the splitter plate height h_{sp}/H = 1/12.5, the freestream flow also runs under the splitter plate. However, at the splitter plate height h_{sp}/H = 1/12.5, the separation area, shown by the white dotted line, increases over that for the splitter plate height h_{sp}/H = 1/50. This phenomenon is also shown by the velocity distribution at streamwise position x/L = 0.58. The position at which the flow velocity becomes the freestream u/U = 1 from the ground at the splitter plate height h_{sp}/H = 1/12.5 is higher than h_{sp}/H = 1/50.

Figure 2.8 shows the pressure contour map of the train model. At h_{sp}/H = 1/12.5, the surface pressure on the side of train model and at the upstream corner on the roof on the train model is higher than that at h_{sp}/H = 1/50, which can be thought to be caused by the splitter plate height. The former increases the rolling moment, and the latter reduces the uplift force.

Therefore, the air flow rate above the train model was smaller because there is insufficient space vertically due to the small nozzle height at the splitter plate height h_{sp}/H = 1/12.5, which possibly increases the rolling moment

The splitter plate is set to h_{sp}/H = 1/50, and the boundary layer thickness and acquire vertical space above the train model is satisfied.

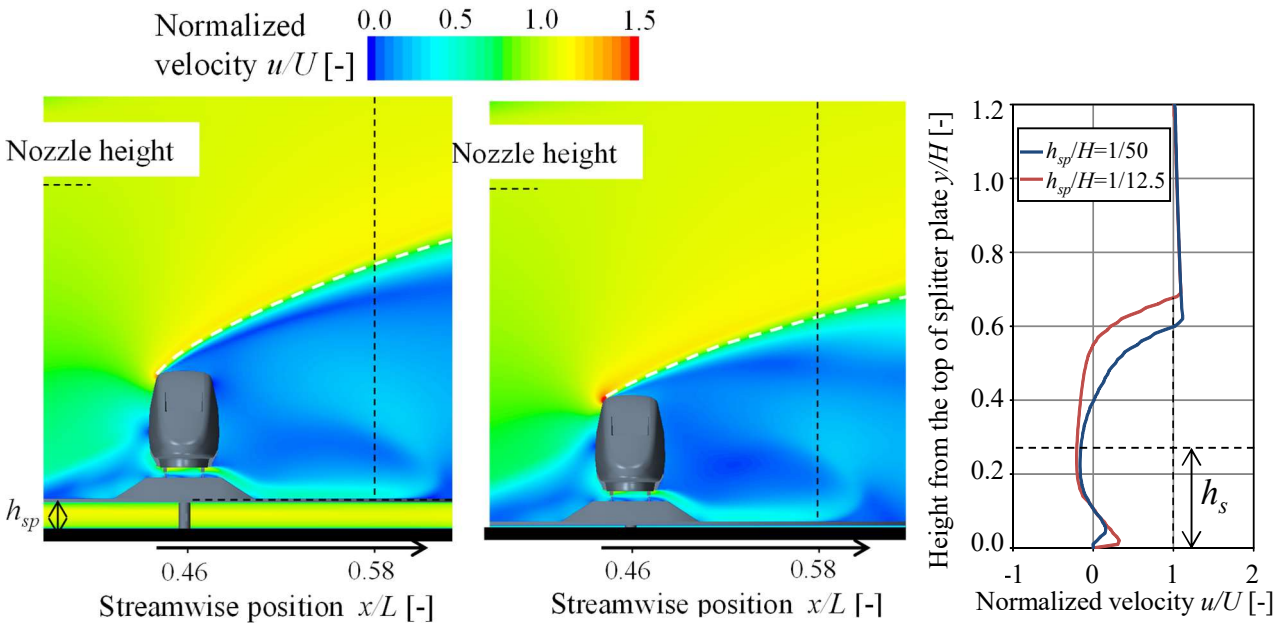

(1) Contour map for splitter plate height h_{sp}/H=1/12.5.

(2) Contour map for splitter plate height h_{sp}/H=1/50.

(3) At streamwise position x/L=0.58.

Figure 2.7 Velocity distribution from simulation results

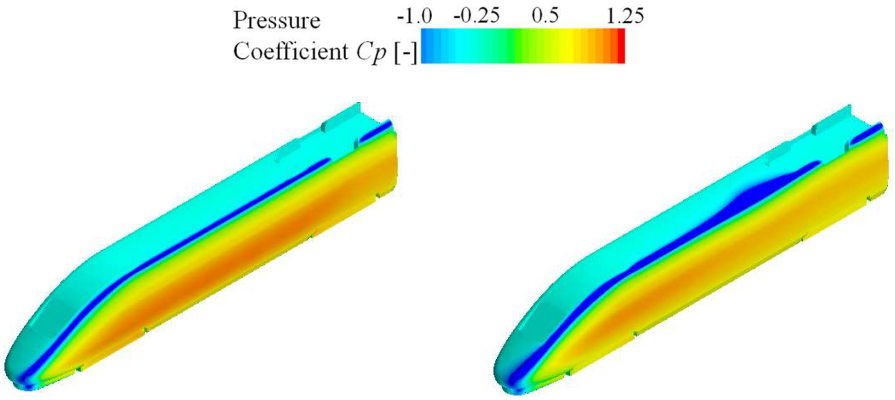

(1) At splitter plate height h_{sp}/H=1/12.5.

(2) At splitter plate height h_{sp}/H=1/50.

Figure 2.8 Surface pressure contour map on the upstream side

2.3. Measurement System Evaluation

2.3.1. Assessment of Developed Measurement System

The wide nozzle and splitter plate were developed in accordance with the design described in chapter 2.2. Figure 2.9 shows an overview of the developed measurement system and Table 2.4 shows the test conditions in this measurement system. The outlet area size of the wide nozzle is W = 1,800 mm and H = 500 mm, which satisfies the target outlet width W and the target blockage x_b. The 1/30 reduced-scale train model is set at the streamwise position x/L = 0.46 from the nozzle on the h_{sp}/H = 1/50 splitter plate and set on the turntable which can change the yaw angle β of the model attitude.

Table 2.4 Test conditions in proposed measurement system

Wind tunnel conditions	Value
Nozzle outlet width W [mm]	1,800
Nozzle outlet height H [mm]	500
Blockage ratio x_b [%]	12.9
Mean wind velocity U [m/s]	40.0
Train model position x/L [-]	0.46
Air density ρ [kg/m^3]	1.17

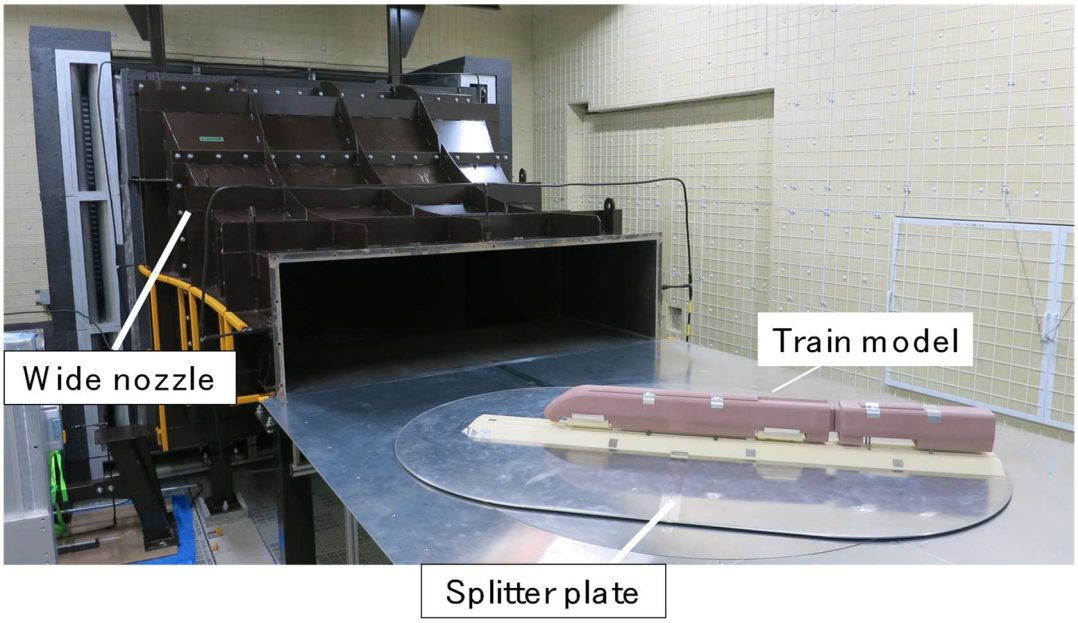

Figure 2.9 Overview of developed measurement system

The flow velocity and the boundary layer thickness were measured by using a hot-wire anemometer (Kanomax, Model 7000Ser) and I-shape probe without the train model, and whether this measurement system satisfies the Reynolds number and boundary layer described in chapter 2.2.1 was evaluated. The Reynolds number based on the measured velocity is Re = 2.67 × 10^5 and exceeds the target value, and the turbulence intensity Tu_x was 0.024. Figure 2.10 shows the velocity profile at the model setup position x/L = 0.46 from the nozzle. The boundary layer thickness at the center of the measurement area, z = 0, is $\delta_{99\%}/h_s$ = 0.31 without the splitter plate and $\delta_{99\%,sp}/h_s$= 0.22 with it. Thus, the boundary layer satisfies to be lower than the target boundary thickness $\delta_{99\%}/h_s$ = 0.3 when the splitter plate is used.

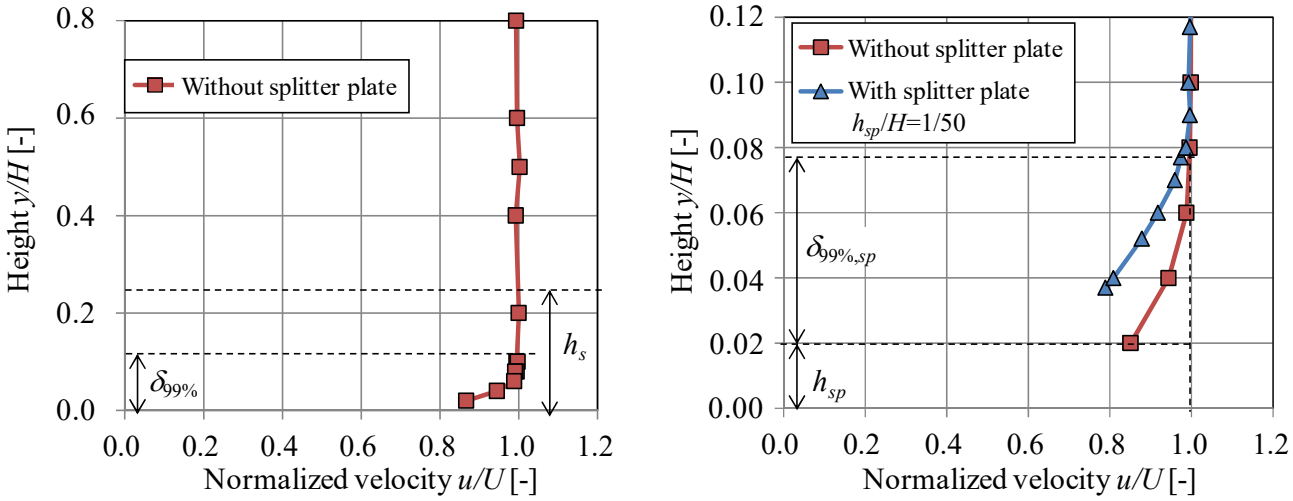

(a) $0 < y / H < 0.8$ (b) $0 < y / H < 0.12$

Figure 2.10 Measured velocity profile at the model setup position x/L = 0.46 from the nozzle outlet

2.3.2. Evaluation of Moment Measurement Accuracy

The proposed system satisfies the equipment requirements and flow specifications in EN14067-6. The force and the moment of the train model, which was described as a wind tunnel benchmark vehicle model in the EN, was measured and the results from the proposed system are compared with those for the reference data indicated in the EN for the evaluation of measurement accuracy.

Figure 2.11 shows the track dimensions described in EN14067-6 and Figure 2.12 shows the rolling moment around the leeside rail. The force and moment of the benchmark vehicle model on the rail are measured every 5-degree yaw angle from 0 to 90 degrees by the load-cell (Nissho-electric-works Ltd., LMC-6524A) with 0.2% measurement accuracy, which is connected with the train model under the ground plate. The side force, uplift force and rolling moment was measured at the sampling rate 100 Hz. The measured value was averaged from 2 times of test runs in each 10 s duration and represented the dimensionless value as Equations (2.7), (2.8) and (2.9).

The measurement accuracy was assessed by the rolling moment coefficient around the leeside rail $C_{Mx,lee}$, which is calculated by using the uplift force coefficient C_{Fz} and the rolling moment C_{Mx} as Equations (2.10).

$$C_{Fx} = {}^{2F_x}\!/_{\rho U^2 A_0} \tag{2.7}$$

$$C_{Fz} = {}^{2F_z}\!/_{\rho U^2 A_0} \tag{2.8}$$

$$C_{Mx} = {}^{2M_x}\!/_{\rho U^2 A_0 d_0} \tag{2.9}$$

$$C_{Mx,lee} = C_{Mx} - C_{Fz} \cdot {}^{b_0}\!/_{d_0} \tag{2.10}$$

where $2b_0$ is the nominal lateral distance between the contact points of a wheel set and has a value of 1.5 m at full scale, d_0 is the reference length 3 m at full scale, and A_0 is the reference area 10 m^2 at full scale. In this research, the German method of the blockage correction in Annex B in EN was adapted. The correction only applies to the rolling moment coefficient, the other coefficients remain unchanged. The correction factor f_{BL} is calculated by Equation (2.11), which leads to f_{BL} = 1.053.

$$f_{BL} = 0.0003x_b^2 + 0.0002x_b + 1 \tag{2.11}$$

Mean flow velocity U with a train model is defined by the nozzle difference pressure measured at the nozzle surface near the inlet and the outlet. Before the force and moment measurement, the correlation between the measured nozzle difference pressure and the mean flow velocity, which is measured without the train model by the pitot-tube, was estimated. And, at the force and moment measurement, the mean flow velocity with a train model was calculated by the measured nozzle difference pressure.

Figure 2.13 shows the sensitivity of the rolling moment coefficient around the leeside rail $C_{Mx,\ lee}$ to the Reynolds number Re at the yaw angle β = 90 degrees. In this research $C_{Mx,\ lee}$ is found to be nearly independent on the Reynolds number at Re of over 2.0×10^5.

Figure 2.14 shows the force and moment coefficients measured in this measurement system and the reference wind tunnel described in EN at every 5-degree yaw angle. Fig. 2.14 also shows the force and moment measurement uncertainty as the error bars. The uncertainty was estimated from the standard deviation of the measured values with 0.5 % of the velocity measurement accuracy. The measured side force coefficient C_{Fx} was the same as the reference at the yaw angles from 0 to 40 deg., but became to be lower than the reference at the yaw angles β=50 deg. and 75 deg., at which the side force has peaks. The measured uplift force coefficient C_{Fz} and rolling moment coefficient C_{Mx} were found to be higher than these of the reference values, especially at the yaw angle β=90 deg. This is because the separation at the corner of the train model roof was slightly different from that measured in the reference wind tunnel described in EN. This wide nozzle has a smaller amount of the air flow rate above the train model than the reference wind tunnel and makes to the flow easily separate from the roof of the train model. This leads that the measured rolling moment coefficient around the leeside rail C_{Mx} was higher than the reference values around the yaw angle β=90 deg.

Table 2.5 shows the measurement results. Comparing the measured and reference values, the tolerance ε, shown in equation (2.12), is the average tolerance ε_{mean} = 0.086 and the max tolerance ε_{max} = 0.149 for all 5-degree yaw angles from 0 to 90 degrees. Figure 2.15 shows the rolling moment coefficient around the leeside rail $C_{Mx,lee}$ which shows the (a)symmetry of the yaw angle β. $C_{MX,lee}$ at the yaw angle β = -45 and -90 degrees was measured within 4% of that at the positive yaw angle β, which shows the symmetry of the incident flow. In this research, $C_{Mx,lee}$ was larger than the reference value at all yaw angle β, including the measurement uncertainty.

This shows the proposed system can obtain results within the required tolerances and has the same measurement accuracy as that in the benchmark described in the European Norm.

$$\varepsilon = \left| \frac{C_{Mx,lee,bmk} - C_{Mx,lee,max}}{C_{Mx,lee,bmk}} \right| \tag{2.12}$$

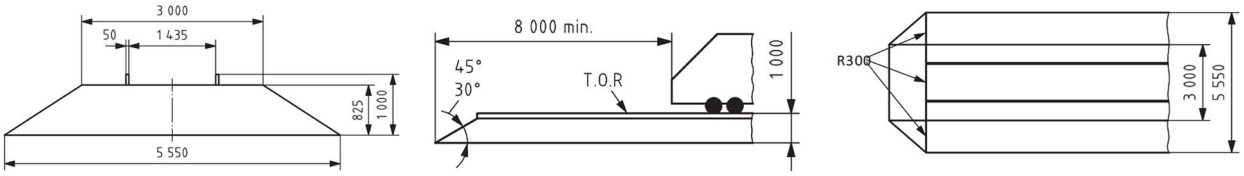

(1) Front view (2) Side view (3) Upper view

Figure 2.11 Sketch of wind tunnel configuration: single-track ballast

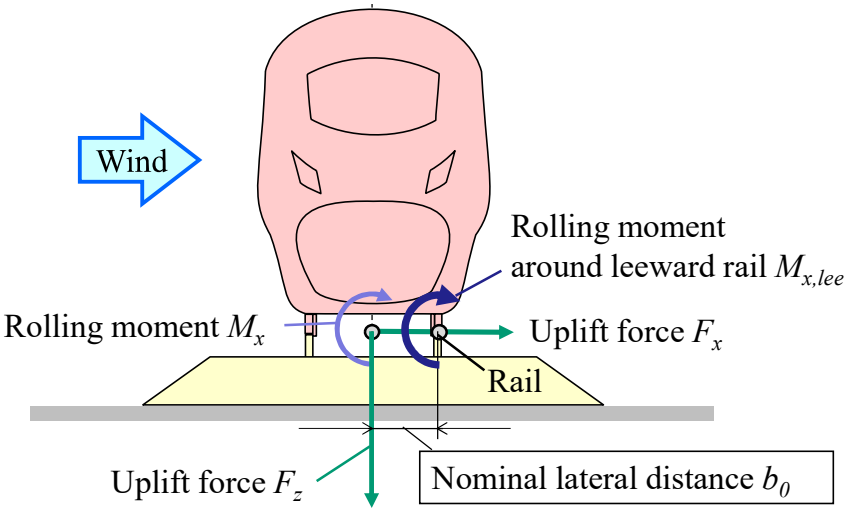

Figure 2.12 Rolling moment around leeward rail

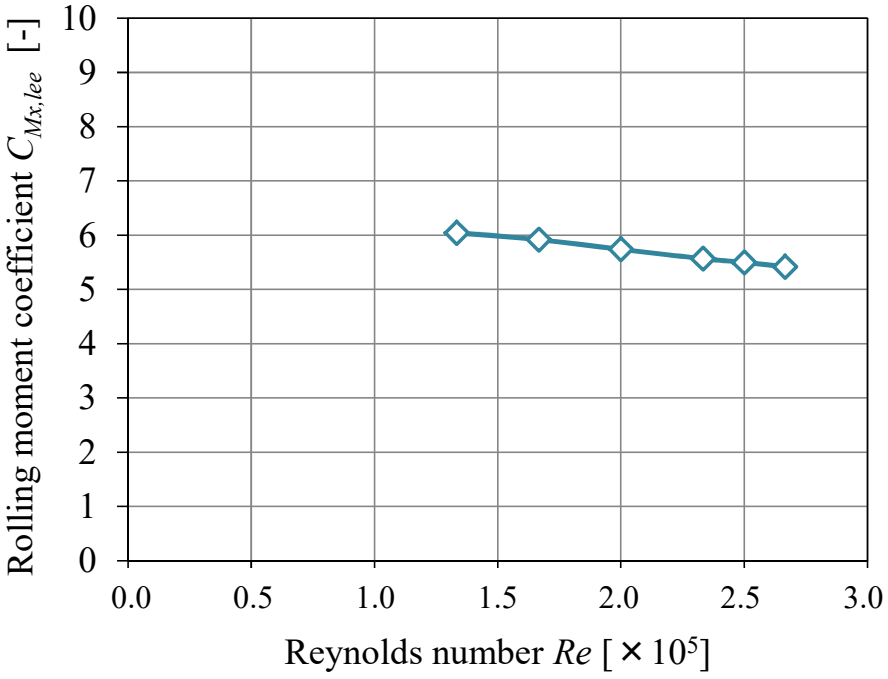

Figure 2.13 The sensitivity of $C_{MX,\,lee}$ to the Reynolds number Re at the yaw angle $\beta = 90$ degrees.

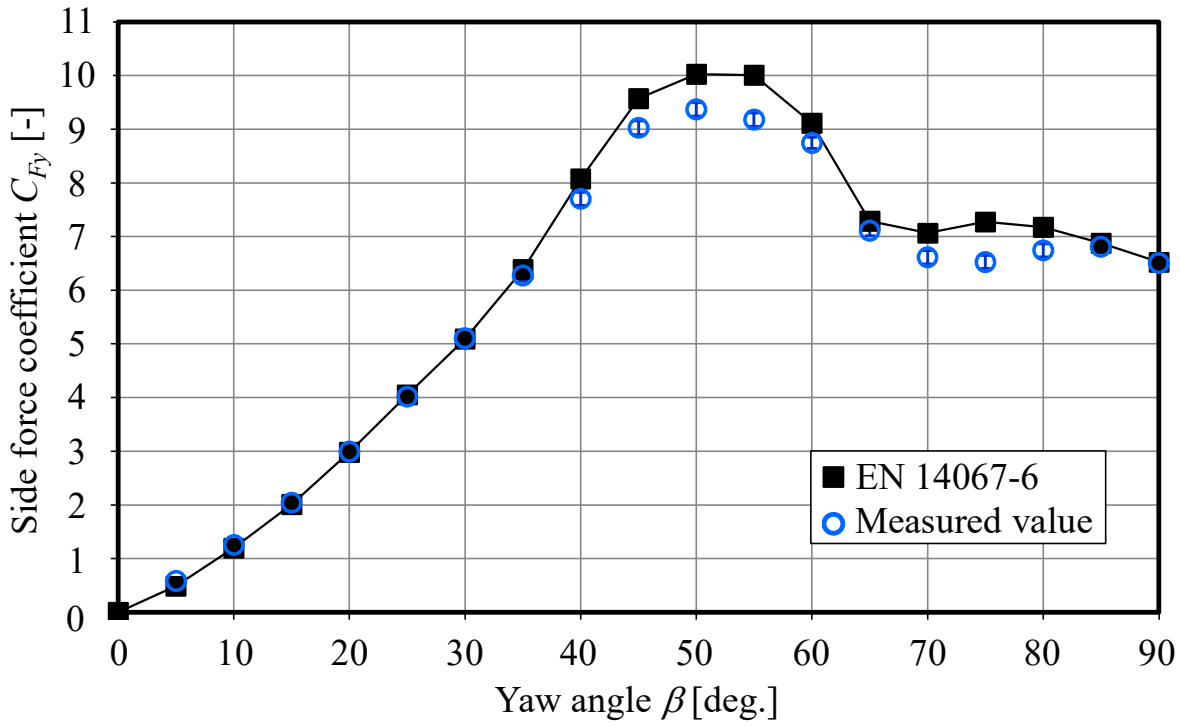

(a) Side Force C_{Fx}

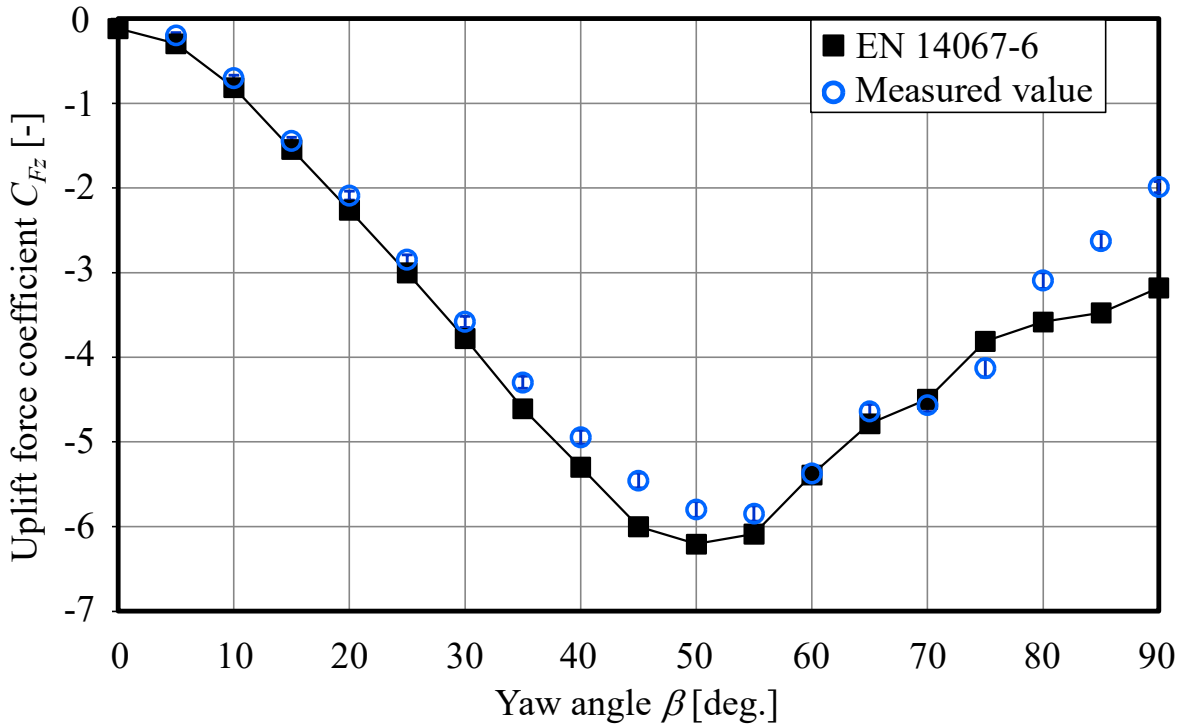

(b) Uplift Force C_{Fz}

Figure 2.14 Force and moment coefficient at every 5-degree yaw angle

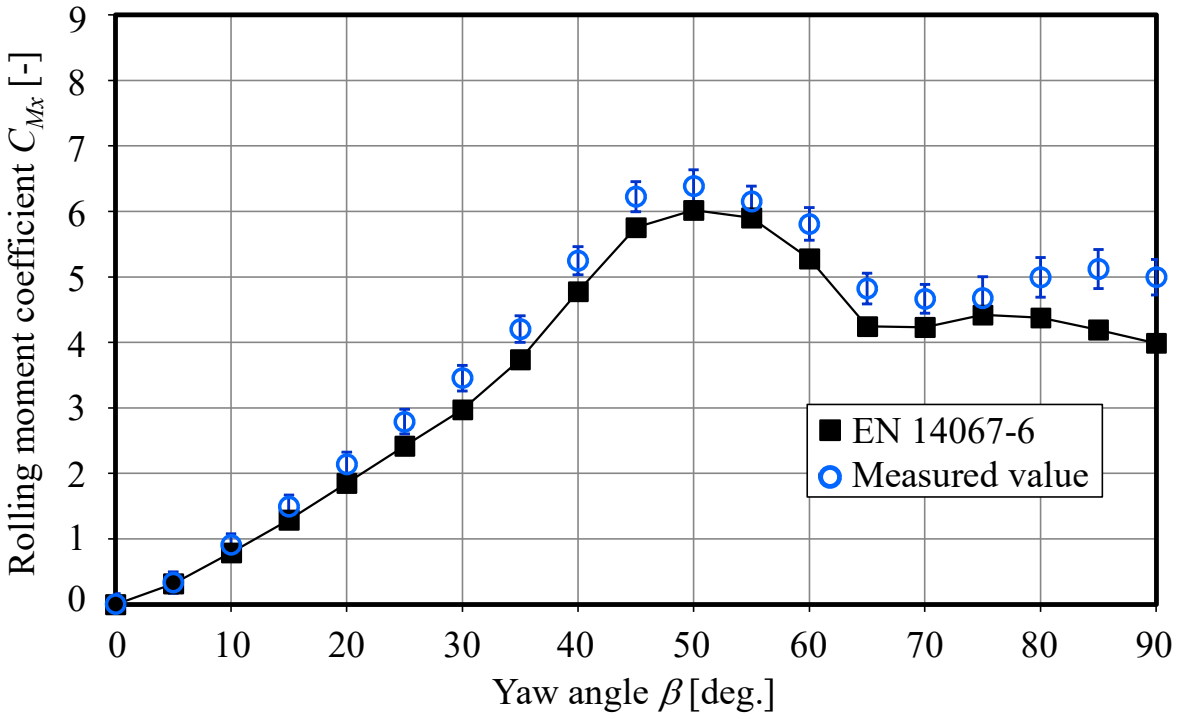

(c) Rolling moment C_{Mx}

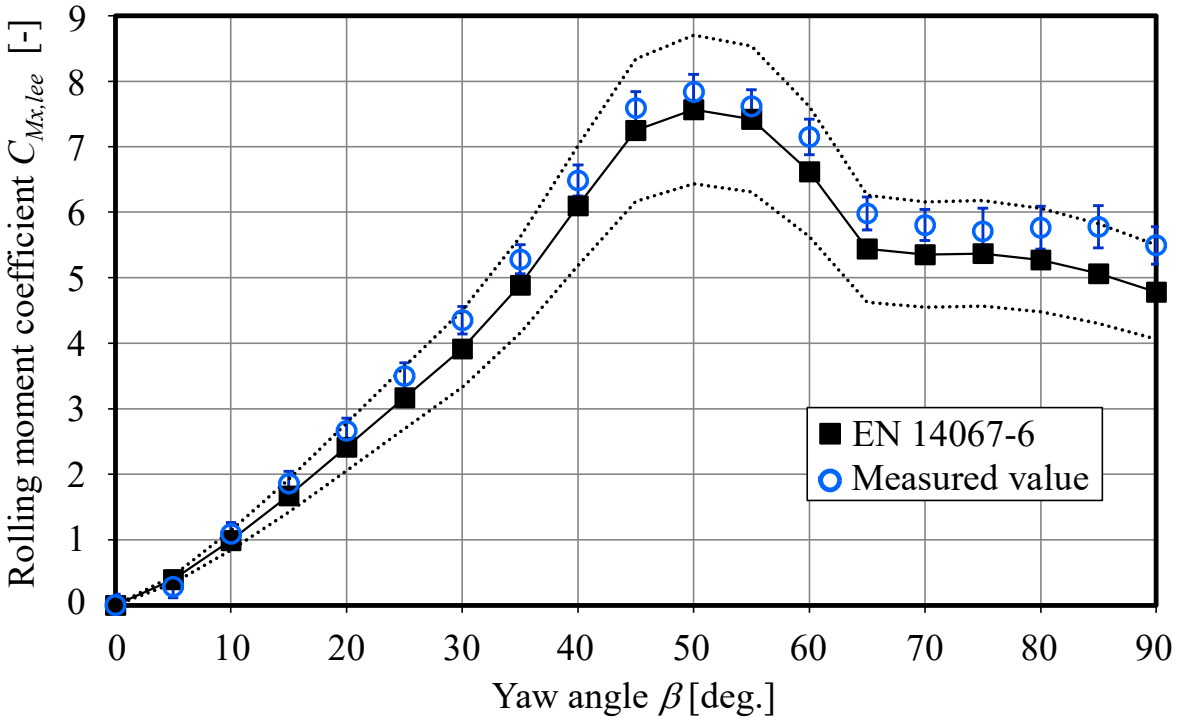

(d) Rolling moment $C_{Mx,lee}$

Figure 2.14 Force and moment coefficient at every 5-degree yaw angle

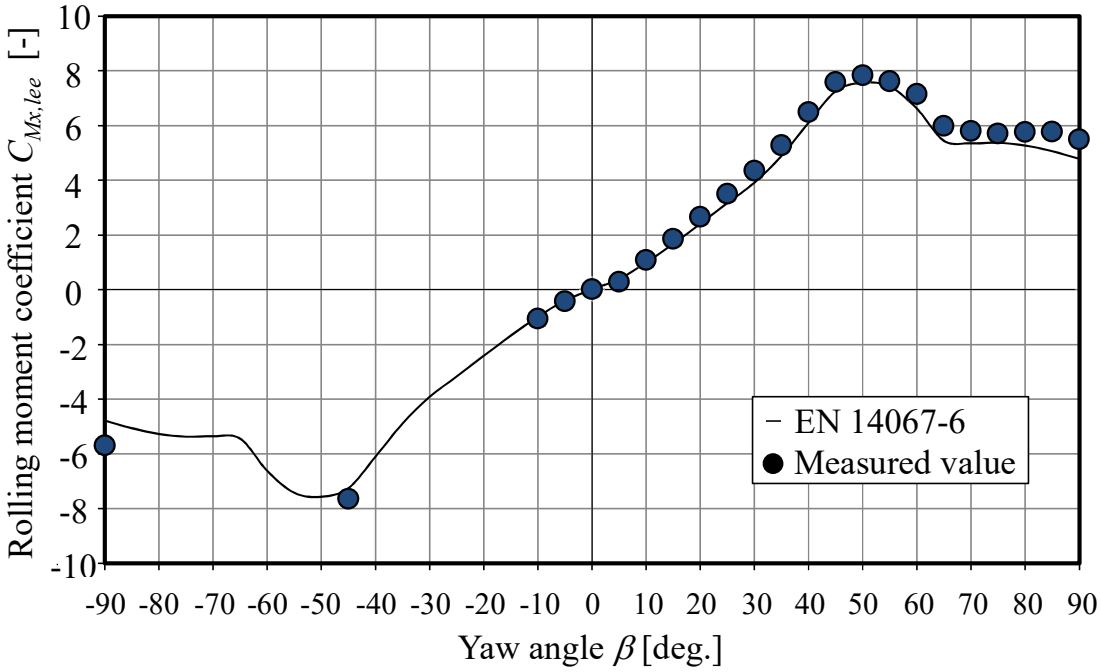

Figure 2.15 Rolling moment coefficient around leeward rail $C_{MX,lee}$ for symmetry check

Table 2.5 Measurement results for proposed measurement system

Wind tunnel conditions		Specifications (Scale s=1/30)	Test results
(1)	Nozzle outlet width W [mm]	≧1,500	1,800
(2)	Blockage ratio x_b [%]	<15	12.9
(3)	Reynolds number Re [$\times 10^5$]	≧2.5	2.67
(4)	Boundary layer thickness $\delta_{99\%}/h_s$ [-]	<0.3	0.22
(5)	Turbulent intensity Tu_x [-]	≦0.025	0.024
Moment measurement results			
(6)	Mean tolerance ε_{mean} [-]	≦0.10	0.086
(7)	Max tolerance ε_{max} [-]	≦0.15	0.149

2.4. Conclusion

An aerodynamic force and moment measurement system including a wide nozzle and a splitter plate was developed with reference to European Norm EN14067-6 for the measurement of the force and the moment of trains precisely in a compact wind tunnel to assess crosswind stability. The development and evaluation revealed the following findings.

A) For effective use of the limited air flow rate, the wide nozzle outlet, which has a width 3.6 times its height, was designed to match the train model, and the adequate contraction from the inlet area to the outlet area was designed by a simple equation (Hassan & Rouse). Simulation and experimental results show that the developed wide nozzle achieves the same flow quality

as that in the reference wind tunnel in the European Norm.

B) The simulation results show that the higher splitter plate with a small nozzle increase the separation area because the flow above the train model runs insufficiently. When the splitter plate was set at the height h_{sp}/H=1/50, the boundary layer thickness was satisfied, and sufficient vertical space was acquired above the train model.

C) The force and moment measurement of the wind tunnel benchmark vehicle model shows that the average and max tolerances of this system are 0.086 and 0.149 from the European Norm for 5-degree yaw angles from 0 to 90 degrees

Thus, the proposed system can satisfy the equipment and flow specifications and has the same measurement accuracy as the benchmark described in the European norm.

2.5. Appendix

2.5.1. Summary of the requirements in the EN 14067-6

Table 2.6 shows the summary of the requirements in the EN 14067-6.

Table 2.6 The summary of the requirements

No.	Items	Clause	Requirement
1	Flow profile	5.3.4.1	Block profile
2	Benchmark test	5.3.4.2	If wind tunnel benchmark tests are conducted, at least one of the three benchmark vehicle models for ICE 3 endcar, TGV Duplex powercar or ETR 500 powercar shall be used. Accuracy for mean rolling moment at leeward rail ($C_{Mx,lee}$) better than 10%. Accuracy for max rolling moment at leeward rail ($C_{Mx,lee}$)better than 15%.
3	Turbulence level	5.3.4.3	$Tu_x \leq 0.025$
4	Boundary layer	5.3.4.4	Less than 30% of the vehicle height
5	Reynolds number	5.3.4.5	$Re > 2.5\times10^5$
6	Reynolds number independency check	5.3.4.5	For one configuration over the range [$0.6\times Re_{max}$, Re_{max}]
7	Mach number	5.3.4.6	$Ma < 0.3$ or smaller than the Mach number of the real train.
8	Blockage	5.3.4.7	Less than 15% at 30°. Blockage corrections are needed for closed test sections
9	Model length / Tunnel width	5.3.4.8	Less than 0.75
10	Train model configuration	5.3.4.8	At least half a down-stream vehicle shall be placed next to the tested model. If the vehicle under investigation is not a leading vehicle, at least one full vehicle ahead needs to be present
11	Ground configuration	5.3.4.12	Standard ground configuration single track ballast and rail
12	Yaw angle	5.3.4.12	Sufficient yaw angle resolution
13	Symmetry check	5.3.4.9	To verify the symmetry of the incident flow, check measurements should be performed with both positive and negative yaw angles.

2.5.2. List of Wind Tunnel Tests Related the EN 14067-6

Table 2.7 shows the summary of the wind tunnel tests for EN 14067-6. In Europe, the wind tunnel tests were conducted in 2009-2010, when the requirement for crosswind was established, in order to check the impact of the different train model, ground configurations and wind tunnels. In Japan, there were few wind tunnel tests for the crosswind requirement.

Table 2.7 Measurement results for proposed measurement system

Author	Gregoire	Rüd	Rocchi		Cheli		Suzuki
Years	2009	2009	2009		2010		2015
Wind tunnel	CSTB[*1]	DNW[*3]	GVPM[*5]		GVPM[*5]		RTRI[*8]
Type	JVCWT[*2]	KKK[*4]	LS[*6]	HS[*7]	LS[*6]	HS[*7]	Maibara
Outlet height H [m]	5	2.4	14	4	14	4	5
Outlet width W [m]	6	2.4	4	4	4	4	2.5
Test wind velocity [m/s]	45	N/A	15	50	10	55	50
Splitter plate height [m]	0.7	N/A	N/A	N/A	0.3	0.3	0.2
Turbulence intensities [%]	1	0.004	2	0.2	2	0.2	0.2
Test model	TGV	ICE3	ATM[*9]		EMUV250		TGV
Reduced-scale s [-]	1/15	1/25	1/10		1/10		1/20
Model height h_s [mm]	270	120	385		385		195
Cars	2	1.5	1.25		1.33		2
Rail configuration	FG[*10]	FG[*10]	FG[*10]		FG[*10]		STBR[*11]
Reynolds number Re [-]	6.0×10^5	1.0×10^6	3.0×10^5	1.0×10^6	2.0×10^5	1.1×10^6	4.9×10^5
Blockage ratio [%]	≤ 3	≤ 5	≤ 4.7	≤ 10	N/A	N/A	≤ 5
Boundary thickness $\delta_{99\%}/h_s$ [-]	≤ 0.3	≤ 0.3	N/A	N/A	50	50	50

*1 CSTB Centre Scientifique et Technique du Bâtiment
(French: Scientific Center and Technical Building)

*2 JVCWT Jules Verne climatic wind tunnel

*3 DNW German-Dutch Wind Tunnels

*4 KKK KRYO-KANAL KÖLN

*5 GVPM Politecnico di Milano Wind Tunnel laboratory

*6 LS Low speed

*7 HS High Speed

*8 RTRI Railway Technical Research Institute

*9 ATM Aerodynamic Train Model

*10 FG Flat Ground

*11 STBR Single Track Ballast and Rail

Chapter 3
Aerodynamic Noise Evaluation for Aeolian Tone and Acoustical Insulating Plate by Similarity Law

List of symbols

A Area of compact body facing turbulent flow [m^2]
B Distance of insulating plate from a pantograph [mm]
C Distance of insulating plate from a pantograph [mm]
D Characteristic length [m]
D_m Measurement distance at the side of a model [mm]
D_p Distance of insulating plate from a pantograph [mm]
H Wind tunnel inlet height [mm]
L Wind tunnel measurement length [mm]
M Mach number (= U/a) [-]
N Fresnel number (= $2\delta/\lambda = 2\delta f/a$) [-]
SPL Sound pressure level [dB]
St Strouhal number [-]
U Wind velocity [m/s]
V_0 A certain volume with a compact body [m^3]
W Wind tunnel inlet width [mm]
ΔL Reduced noise level by a sound insulating plate with infinite length [dB]

a Sound speed [m/s]
b Distance between noise source and edge of sound insulating plate [m]
c Distance between edge of sound insulating plate and measurement point [m]
d Distance between noise source and measurement point [m]
d_c Diameter of cylinders [mm]
f Frequency [Hz]
h_b Height of a pantograph body [mm]
h_c Height of cylinders [mm]
h_i Height of insulating plate [mm]
h_t Height of a pantograph panhead [mm]
l Turbulent correlation length [m]
l_h Length of periodic holes of a cylinder [mm]
l_i Length of insulating plate [mm]
l_p Assumed length of insulating plate [mm]
r Measurement distance [m]
w_h Width of periodic holes of a cylinder [mm]

Π Sound power [dB]

δ Distance difference among a noise source, an edge of plate and a measurement point [m]

λ Wavelength of sound [m]

ρ Air density [kg/m^3]

Suffix

b From pantograph body

d A value from a dipole sound source

est Estimated value

m A value of a reduced-scale model

mea Measured value

r A value of a full-scale model

red Reduction effect

p Peak noise from a cylinder

pl A sound insulating plate

q A value from a quadrupole sound source

t From pantograph panhead

the Theoretically calculated value

1st 1st peak noise from a cylinder

2nd 2nd peak noise from a cylinder

3.1. Introduction

The trend of speeds of inter-city trains around the world is to become faster. It is necessary to prevent trains from disturbing environment along railway lines and especially to reduce aerodynamic noise, which increases as running speeds of trains increase. Detailed knowledge on the noise distribution and properties of sound sources are necessary for the reduction in aerodynamic noise. Measuring the noise of full-scale running trains is useful for finding a noise distribution. Martens et al. (2009) identified different noise sources of the German ICE 3 train by using a microphone spiral array, and Kurita (2011) carried out noise measurements on a series E2-1000 train that was running and the areas which generate sound and its contribution to overall noise are clarified. However, measuring the noise of full-scale trains requires noise reduction methods, and developing such methods requires enormous cost and time. Therefore, generally, wind tunnel tests are conducted for evaluation of such methods. We measure the radiated aerodynamic noise of a reduced scale model in a wind tunnel and estimate the full-scale noise from the test result by using the similarity law of aerodynamic noise. For example, Yamazaki et al. (2007) investigated noise reduction techniques for the gap section in a 1/8 scale train model in a wind tunnel.

The similarity law is important for accurately estimating full-scale noise from the results obtained with a reduced scale model. The law needs to convert the noise spectrum of a reduced scale model in a wind tunnel into that of a full-scale one by taking the difference between the wind velocity, the scale and the measurement conditions of the two models into consideration. Iida et al. (2000, 2007) suggested using the law for aerodynamic sound generation to estimate full-scale model noise. In the similarity law, the sound pressure level SPL is in proportion to the sixth power of wind velocity and to the double power of the scale from the sound pressure of a reduced-scale model SPL_m. The full-scale frequency f_r [Hz] is acquired from the frequency of the scale model f_m [Hz], the wind velocity U [m/s], and the characteristic length D [m].

$$SPL_r = SPL_m + 10\log\left(\frac{{a_m}^2{\rho_r}^2}{{a_r}^2{\rho_m}^2}\right) + 60\log\left(\frac{U_r}{U_m}\right) + 20\log\left(\frac{D_r}{D_m}\right) - 20\log\left(\frac{r_r}{r_m}\right) \tag{3.1}$$

$$f_r = St\frac{U}{D} = f_m\frac{D_m}{D_r}\frac{U_r}{U_m} \tag{3.2}$$

Where a [m/s]: the sound speed, ρ [kg/m^3]: the air density, and r [m]: measurement distance. the suffix m denotes the value of a reduced-scale model and the suffix r does the value of a full-scale model

This similarity law is derived from Lighthill-Curle's equation (Lighthill 1952; Curle 1955). The equation indicates that the main source of aerodynamic noise is changed from a dipole sound source generated by aerodynamic force fluctuation to a quadrupole sound source generated by flow disturbances, depending on the Mach number. The difference in noise source leads to the similarity law being changed, such as the correlation between wind velocity and aerodynamic noise level. A dipole sound source increases in proportion to the sixth power of wind velocity, and a quadrupole sound source increases in proportion to the eighth power of wind velocity. In Curle's equation, the sound power Π_d and Π_q, which are directly radiated from a dipole sound source and a quadrupole sound source in a certain volume V_0

with a compact body, is approximated as Eqs. (3.3) and (3.4) and the ratio of sound power Π_q / Π_d is approximately estimated by the Mach number as Eq. (3.5).

$$\Pi_d \sim \frac{A\rho_0 U^6}{a^3} = A\rho_0 U^3 M^3 \tag{3.3}$$

$$\Pi_q \sim \frac{\left(\frac{V_0}{l}\right)\rho_0 U^8}{a^5} = \left(\frac{V_0}{l}\right)\rho_0 U^3 M^5 \tag{3.4}$$

$$\Pi_q \Big/ \Pi_d \sim \frac{\left(\frac{V_0}{l}\right)}{A} M^2 \tag{3.5}$$

Where A [m^2]: Area of compact body facing turbulent flow, $M(= U/a)$ [-]: Mach number, V_0 [m^3]: a certain volume, l [m]: turbulent correlation length.

Until now, the radiated aerodynamic noise from trains was regarded as a dipole sound source generated from surface pressure fluctuations since the Mach number of the flow around trains is comparatively small. Therefore, we estimate the noise level of full-scale trains in proportion to the sixth power of the train running speed as Eq. (3.1). However, next generation high-speed trains are expected to run faster, which will probably lead to full-scale estimated noise error because of the quadrupole sound source of the aerodynamic noise from trains or the difference in wind velocity between reduced-scale and full-scale models.

In this study, the aerodynamic noise that radiates from cylinders with and without periodic holes and a reduced-scale pantograph model with and without a sound insulating plate, which are generally used for suppression of noise from high-speed trains, are measured in a low-noise high-speed wind tunnel, and the change in the similarity law was evaluated when the flow was accelerated to be faster than 100 m/s. We investigated the correlation between wind velocity and aerodynamic noise level for structure with acoustical insulation and assessed aerodynamic noise sources and wind velocity conversion with the similarity law.

3.2. Experimental Setup

Experiments were performed in a low noise high-speed wind tunnel (Hitachi 2014; Matsui et al. 2017). The wind tunnel test section is 600 mm (W) × 400 mm (H) × 2,000 mm (L), and the maximum flow speed is 116.7 m/s. Figure 3.1 shows the configuration of the experimental setup. The test model was installed at a location 400 mm from a nozzle, and a microphone (DC53A, Rion) was set up at spanwise D_m = 1,000 mm from the center of the model at the same height as a ground plate to reduce the effect of noise reflection. The noise was measured by a sound-level meter (NL-14, Rion) and recorded by a data logger (DS-2000, Onosokki). The sampling frequency was 40,000 Hz. The measured data was FFT-analyzed. The sampling points is 16,384 points and the average time was 64 times.

Two types of test models, cylinders and a pantograph model, were used. Figure 3.2 shows the cylinders used in this study. The cylinders, of which the diameter was d_c = 25 mm and the height was h_c = 550 mm, were measured. It is seen in Fig. 3.2(b) that the cylinder was set vartically on the gound plate.

One of them had 11 periodic holes, of which the width was w_h = 5 mm and length was l_h = 20 mm. Periodic holes are known to reduce aerodynamic noise, especially peak noise, named “aeolian tone,” by preventing Kármán vortex shedding (Takaishi et al. 2003).

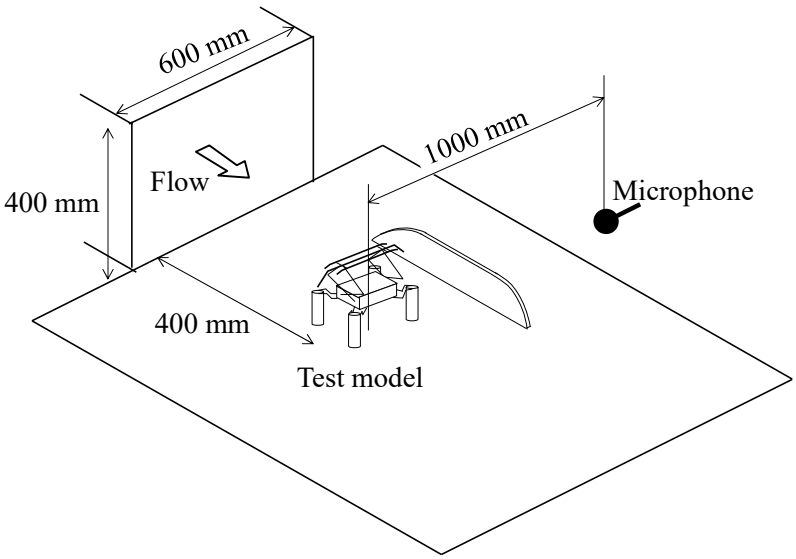

Figure 3.1 Experimental setup

(a) Test model

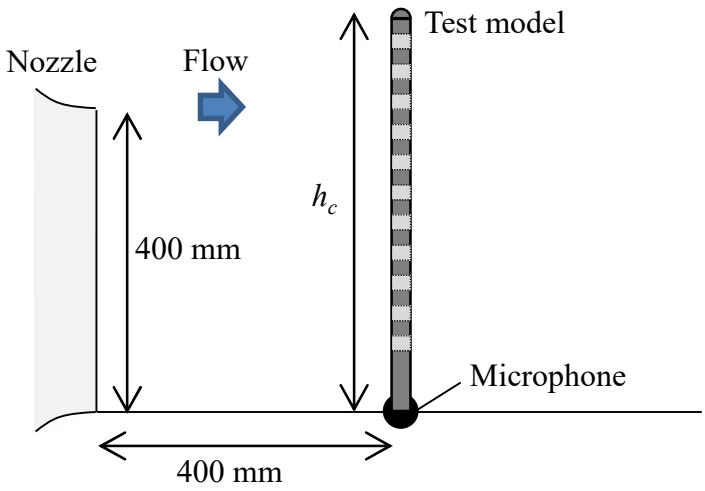

(b) Setup postion from the side view

Figure. 3.2 Cylinders with and without periodic holes

We also measured the noise radiated from the 1/10 reduced-scale pantograph model. Generally, sound insulating plates are used in shinkansens (bullet trains) in Japan (Wakabayashi et al. 2008), and pantograph noise is prevented from radiating. The pantograph noise with and without a plate was measured, and noise reduction effect of sound insulating plates was evaluated. An insulating plate was set at the microphone side D_p =150 mm from the center. The height of the sound insulating plate was h_i = 0.53 D_p and its length l_i = 3.3 D_p with 30 degrees bottom corners. The height of the pantograph was h_t = 0.9 D_p.

3.3. Experimental Result

3.3.1. Background Noise

Figure 3.3 shows the background noise level of the wind tunnel. The horizontal axis indicates the wind velocity, and the vertical axis indicates the sound pressure level (*SPL*) measured by the sound-level meter. The dashed line is the sum of the sixth and eighth powers, shown as Eq. (3.6), in which B and C is calculated by using the least square method to minimize the difference from the experimental value. The result shows the contribution of dipole sound and quadrupole sound in the background noise. In a low-speed region until 60 m/s, the background noise was mainly proportional to the sixth power of wind velocity. This dependence shows that the dominant sound of the background noise was a dipole sound source from the surface pressure fluctuation on the nozzle and collector. In a high-speed region, the background noise became proportional to the eighth power of wind velocity. This dependence shows that the noise generated by the vortex generated from the shear layer at the nozzle became the dominant aerodynamic noise source, that is, a quadrupole sound source.

$$SPL_{est} = 10\log(B \cdot U^6 + \mathrm{C} \cdot U^8) \tag{3.6}$$

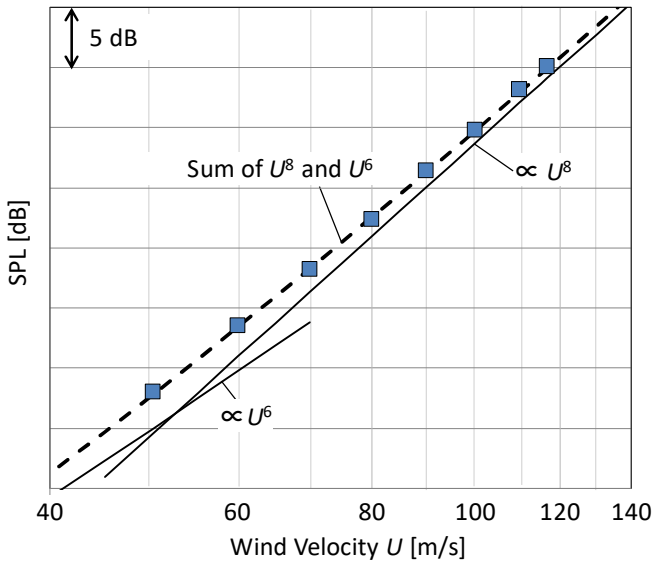

Figure 3.3 Background noise level of wind tunnel. Measured value of wind tunnel background noise is plotted with square dots (blue), and dashed line is sum of sixth and eighth powers, which was calculated by least square method to minimize difference from measured value.

3.3.2. Cylinders without and with Periodic Holes

3.3.2.1. Cylinders without periodic holes

Figure 3.4 shows the overall noise level of the cylinders at each wind velocity. The noise level of the cylinder without periodic holes continued to increase in proportion to the sixth power of wind velocity. This indicates that the aerodynamic noise of the cylinder mainly consisted of a dipole sound source. Its main noise source is known to be generated from the Kármán vortices. The Strouhal number, which shows the dimensionless frequency of the Kármán vortices from a cylinder, depends on its Reynolds number and changes at a Reynolds number Re of approximately 1.0×10^6 due to the laminar-turbulent transition of the boundary layer around the cylinder (Fujita et al.; 1999). In this study, the Reynolds number Re based on the cylinder diameter d_c was 1.9×10^5 at the maximum wind velocity $U = 116.7$ m/s. The Strouhal number St of the Aeolian tone generated by the Kármán vortex is considered to be constant in this range. Figure 3.5 shows the frequency analysis results of the measured noise radiated from a cylinder at 50 and 110 m/s. The dominant peak noise level of the cylinder without periodic holes was found at the frequency $f_{p,1st} = 381$ Hz (at 50 m/s) and $f_{p,1st} = 825$ Hz (at 110 m/s). And, the second peak noise level was found at the peak frequency $f_{p,2nd} = 756$ Hz (at $U = 50$ m/s) and $f_{p,2nd} = 1{,}633$ Hz (at $U =$ 110 m/s). Figure 3.6 shows the Strouhal number St of the peak frequencies, the representative length of which was set as the cylinder diameter d_c. Regardless of the wind velocity, the Strouhal number St was constant i.e., the Strouhal number of the first peak is $St_{p,1st} = 0.19$ and that of the second peak is $St_{p,2nd} =$ 0.38, which implicates the vortex formation is constant.

Figure 3.7 shows the peak noise levels at each wind velocity. The dashed line is the sum of the sixth and eighth powers, shown as the Eq. (3.6), in which C and D is calculated by using the least square method and the difference from the experimental value was minimized. The first peak noise level, which is dominant in the noise radiated from the cylinder, increases in proportion to the sixth power of wind velocity. However, the second peak noise level increases in proportional to the sum of the sixth and eighth powers of wind velocity. Over the wind velocity $U = 130$ m/s, the eighth power of wind velocity became dominant. This indicates the second peak noise was changed from a dipole sound source to a quadrupole sound source. This is why the ratio of noise from a quadrupole source increases at higher frequency. Generally, representative noise at higher frequency f_p, which related to the wind velocity U and the turbulent correlation length l as the in Eq. (3.7), generated from the vortices with the shorter turbulent correlation length l. Equation (3.4) presents that shorter turbulent correlation length l generates higher noise level from a quadrupole sound source. In this study, the Kármán vortex is assumed to generate a sufficient quadrupole sound source at the second peak noise frequency.

$$f_p \sim \frac{U}{l} \tag{3.7}$$

This result indicates that the dominant peak noise level of a cylinder increases in proportion to the sixth power of wind velocity as a dipole sound source while vortex formation is steady. However, noise at higher frequency may increase in proportional to the sum of the sixth and eighth powers of the wind velocity because a quadrupole sound source increases due to the shorter turbulent correlation length l.

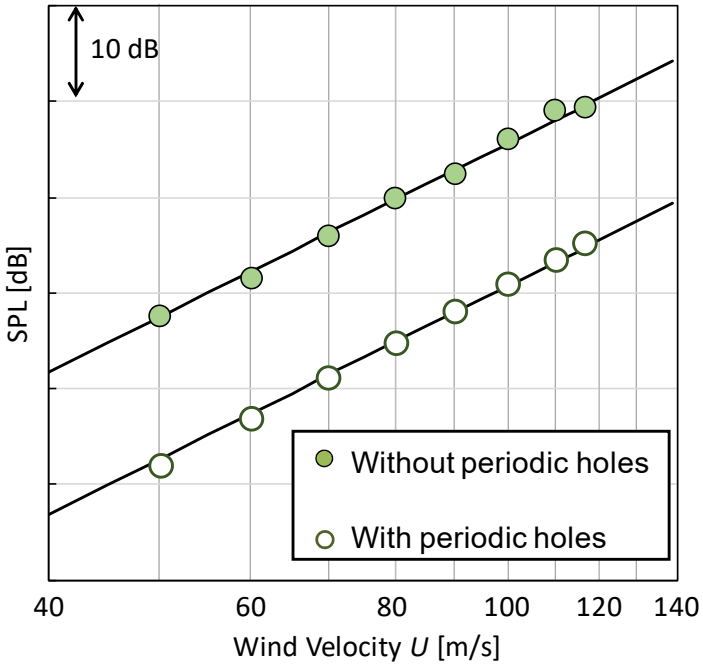

Figure 3.4 Over all noise level of cylinders. Measured values of cylinders without and with periodic holes are plotted with white and green dots. Solid line shows sixth power of wind velocity estimated from the experimental value.

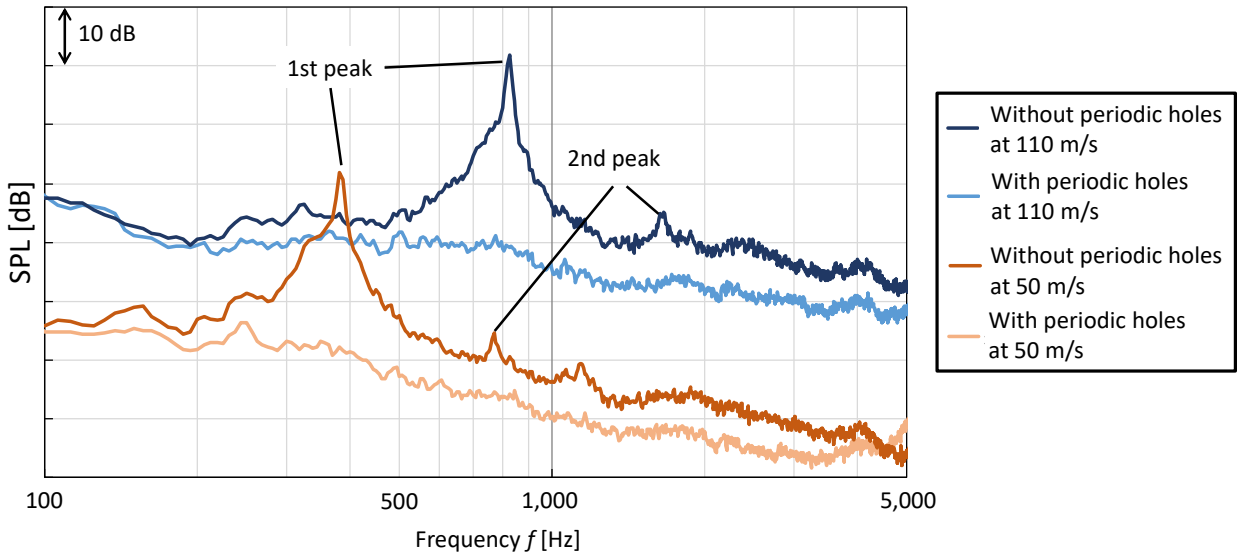

Figure 3.5 Comparison of noise level of cylinders at 50 and 110 m/s. Values of cylinders without and with periodic holes measured at 50 m/s are shown with orange and red lines, and those at 110 m/s are shown with black and blue lines.

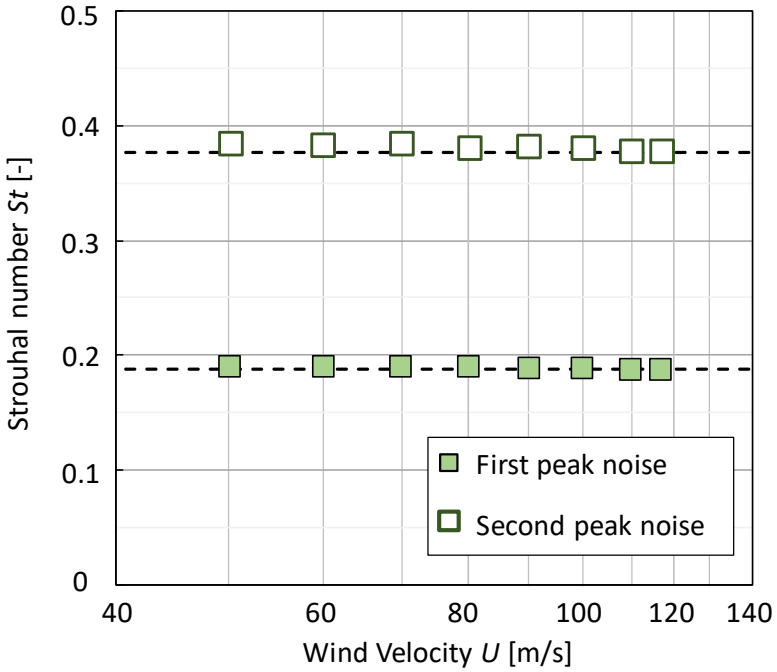

Figure 3.6 Strouhal number of the first and second peaks noises. Measured values of cylinders without and with periodic holes are plotted with white and green square dots. Dashed line shows the average value.

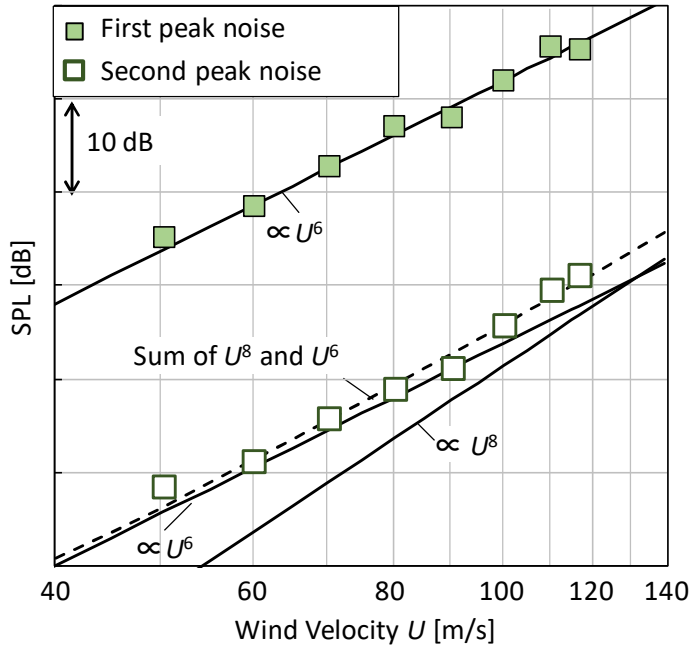

Figure 3.7 Peak noise levels of cylinders without periodic holes. Measured values of the first and second peak are plotted with green and white square dots. Dashed line is sum of the sixth and eighth powers of wind velocity estimated from experimental value by least square method.

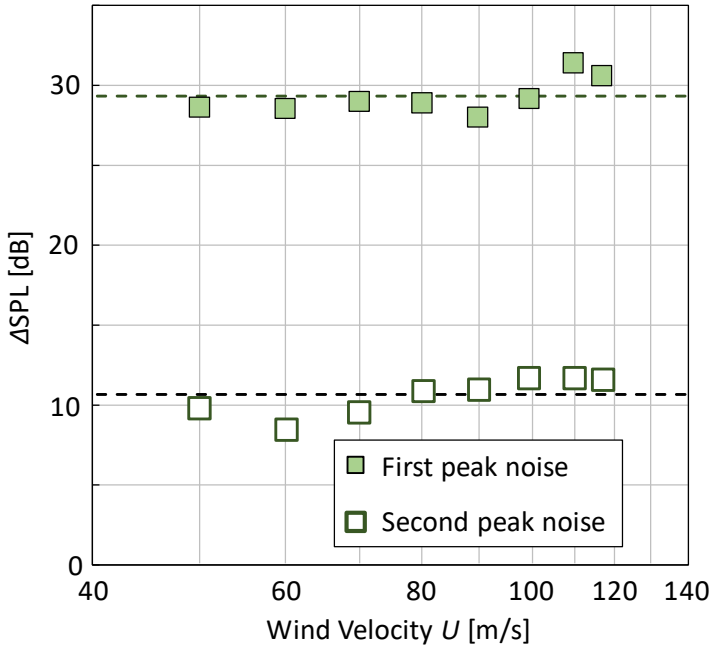

Figure 3.8 Reduction noise level of the first and second peak noises. Measured values of the first and second peak noises are plotted with green and white square dots.

3.3.2.2. Cylinders with periodic holes

Figure 3.4 also shows the overall noise level of the cylinders with periodic holes. The noise level also increased in proportion to the sixth power of wind velocity. This indicates that the aerodynamic noise of the cylinder with periodic holes also mainly consisted of a dipole sound source. Figure 3.5 illustrates that the periodic holes reduced the noise level: mainly, the peak noise of the cylinder at both 50 and 110 m/s. The periodic holes kept preventing the Kármán vortex, which generates the Aeolian tone in this Reynolds number condition. Figure 3.8 shows the reduced noise level by the periodic holes at the frequency, at which the first and second noise peak was observed. The reduction noise level $\Delta SPL_{p,red}$ at each wind velocity is estimated by Eq. (3.8).

$$\Delta SPL_{p,red} = SPL_{p,witho\quad hole} - SPL_{p,with\,holes} \tag{3.8}$$

Figure 8 indicates the reduction noise level is almost constant, the reduction of the first and second peak noise is about 29 dB and 11 dB with the difference 2 dB. In this Reynolds number range, vortex formation was not changed, and the periodic holes steadily prevented Kármán vortex formation and reduced peak noises, regardless of the wind velocity.

3.3.2.3. Estimation by similarity law

The noise levels of the cylinders without and with periodic holes at the wind velocity U = 110 m/s was estimated from the measured noise levels at the wind velocity U = 50 m/s in two ways, and the similarity law was evaluated. Firstly, the value $SPL_{est,Vd=11\quad/s}$ was calculated by using Eqs. (3.2) and (3.9). Equation (3.9) is transformed from Eq. (3.1) for applying the only wind velocity conversion. Secondly, the estimated value $SPL_{est,Vdq}$ was also calculated by using Eqs. (3.2), (3.9) and (3.10). Equation (3.10) includes the eighth power of wind velocity as a quadrupole sound at the frequency greater than the second peak noise frequency of f = 1,600 Hz because the sound level from a quadrupole sound was almost the same as that from a dipole sound at the second peak noise frequency at the wind velocity U = 110 m/s as shown in Fig. 3.7.

$$SPL_{est,Vd} = SPL_{mea,U=50m/s} + 60\log\left(\frac{110m/s}{50\quad/s}\right) \tag{3.9}$$

$$SPL_{est,Vdq} = SPL_{mea,U=50m/s} + 0.5\times 60\log\left(\frac{110m/s}{50m/s}\right) + 0.5\times 80\log\left(\frac{110m/s}{50\quad/s}\right)$$

$$\text{at } f \geq 1600 \text{ Hz} \tag{3.10}$$

Figure 3.9 shows the measured and estimated noise levels of the cylinders without and with periodic holes at the wind velocity U = 110 m/s. Figure 3.9(A) shows that the overall noise levels of the cylinder without periodic holes, $SPL_{est,Vd}$ and $SPL_{est,Vdq}$, were estimated with 0.9 dB difference from the measured value. This was why the first peak noise, which was dominant noise of a cylinder without periodic holes, was estimated precisely by using the wind velocity conversion as the sixth power of the wind velocity as a dipole sound source. However, the estimated value $SPL_{est,Vd}$ was approximately 4 dB lower than the measured value at the frequency greater than 1,600 Hz, as shown in Fig. 3.9(A). This was caused by not including the wind velocity conversion of a quadrupole sound source in $SPL_{est,Vd}$. On the other hand, the estimated value $SPL_{est,Vdq}$ was within 2 dB from the measured value at the frequency greater than 1,600 Hz. Fig. 3.9(B) shows the overall noise levels of the cylinder with periodic holes were estimated with 0.5 dB difference from the measured value. The estimated value $SPL_{est,Vdq}$was closer to the measured value at the frequency greater than 1,600 Hz than $SPL_{est,Vd}$.These results indicate that the similarity law needs to include the eighth power of wind velocity at high frequency for more precise estimation of noise level at the frequency greater than the second noise peak frequency in this study.

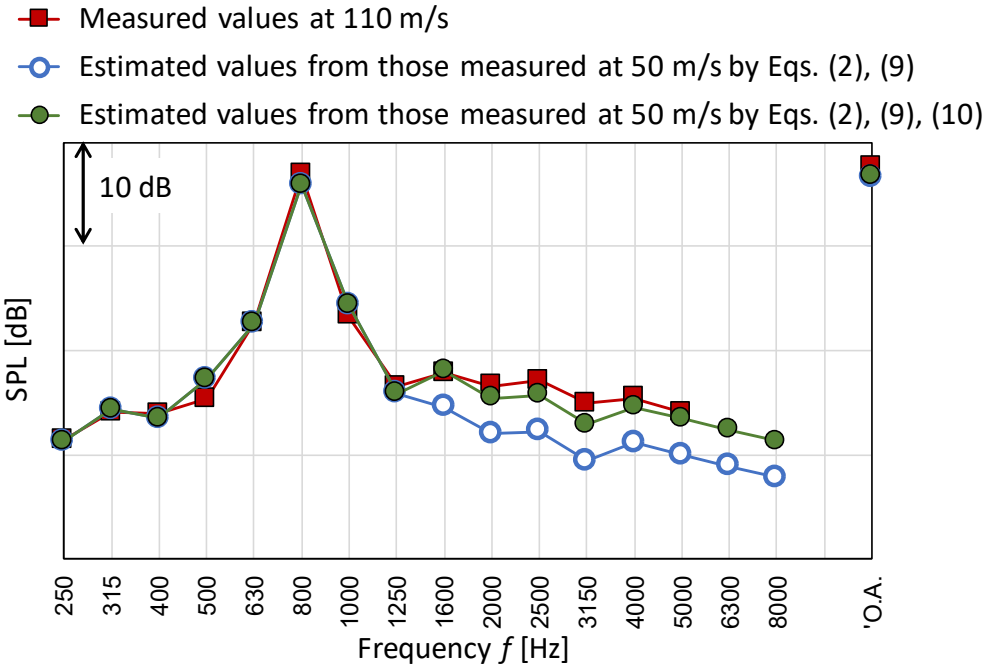

(A) Cylinders without periodic holes

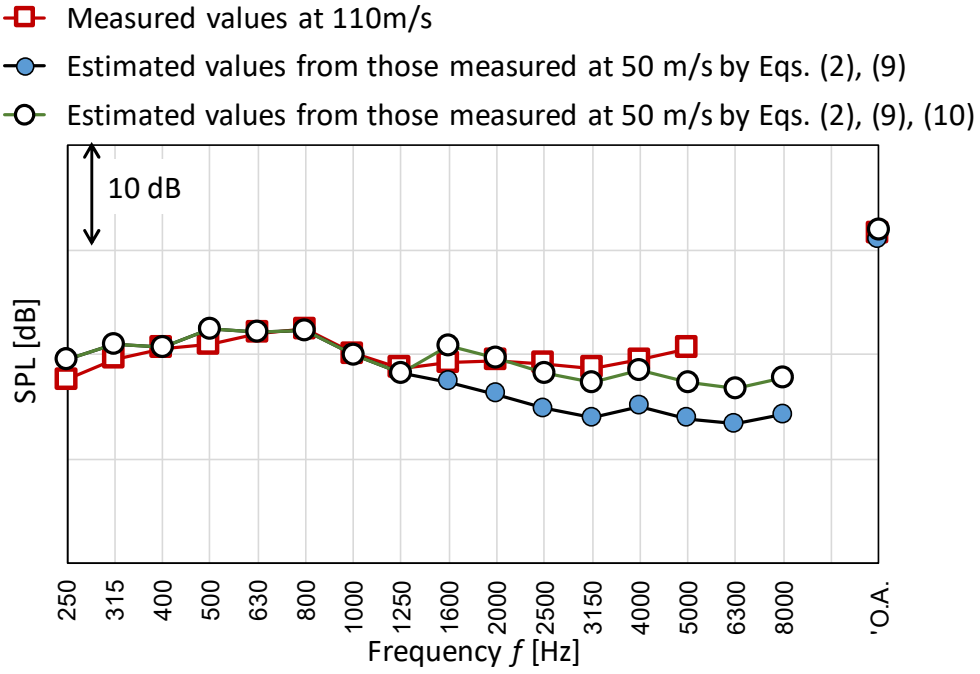

(B) Cylinders with periodic holes

Figure 3.9 1/3 octave band frequency analysis of the noise from measured and estimated values of cylinders without and with periodic holes at the wind velocity U = 110 m/s. Measured values are plotted with white square dots. Estimated values by Eqs. (3.2), (3.9) and ones by Eqs. (3.2), (3.9), (3.10) are plotted with blue and green circle dots.

3.3.3. Pantograph Models without and with Sound Insulating Plate

3.3.3.1. Comparison of pantograph models without and with sound insulating plate

Figure 3.10 shows the noise level of the full-scale pantograph estimated from the measured values of a 1/10 scale model. The noise level of the pantograph without the sound insulating plate continued to increase in proportion to the sixth power of wind velocity. This indicates that the aerodynamic noise of the pantograph mainly consisted of a dipole sound source. The dipole sound source generated from surface pressure fluctuations is considered to be caused by the shape of the pantograph was dominant. However, the noise level of the pantograph model with the sound insulating plate increased in proportion to less than the sixth power of wind velocity. This indicates that the effect of noise reduction with the sound insulating plate increased in accordance with wind velocity.

Figure 3.11 shows a comparison of the noise level radiated from the pantograph without and with the sound insulating plate at 50, 75 and 116.7 m/s. The comparison of the pantograph without the plate at different wind velocity shows that the dominant frequency of the pantograph noise increased according to increasing the wind velocity. This peak frequency increased from 500 Hz at 50 m/s to 750 Hz at 75 m/s and 1,250 Hz at 116.7 m/s, which shows the frequency increases in accordance with the Strouhal number, written in Eq. (3.2). The comparison of the pantograph without and with the plate at the same wind velocity illustrates that the sound insulating plate reduced more noise level at a high frequency than that at a low frequency. This is why the diffraction of acoustic wave was changed by noise frequency. Because of its short wavelength, the expansion of high-frequency sound at the edge of sound insulating plate due to diffraction was prevented and noise radiated from the pantograph was shielded more. The comparison of the pantograph with and without the plate at different wind velocity presents that the dominant pantograph noise level began to reduce by the sound insulating plate as the wind velocity increased. The peak noise level of the pantograph model at 116.7 m/s was reduced 2.9 dB by the sound insulating plate in contrast to that at 50 m/s. This resulted from that the dominant frequencies of the pantograph noise increases as the wind velocity increases and the noise reduction of the sound insulating plate is more effective in the higher frequencies. Therefore, the noise reduction effect of the sound insulating plate was increased by increasing the wind velocity. This leads that the pantograph model with the sound insulating plate increases the noise level in proportion to less than the sixth power of wind velocity.

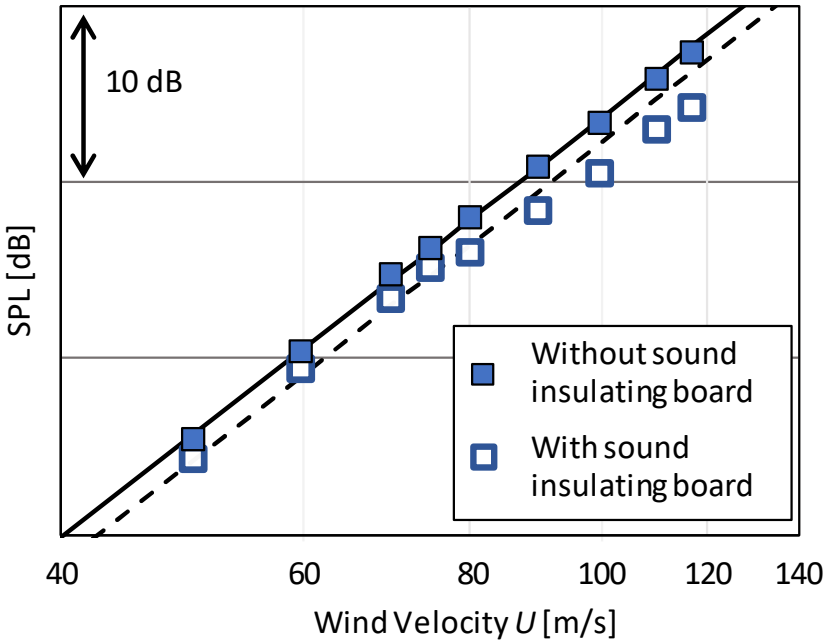

Figure 3.10 Overall noise level of full-scale pantograph estimated from measured values of 1/10 scale model. Measured values of pantograph without and with sound insulating board are plotted with white and blue squares. Solid line is sixth power of wind velocity estimated from measured value of pantograph without sound insulating board, and dashed line is that of pantograph with sound insulating board in low-speed region until 80 m/s.

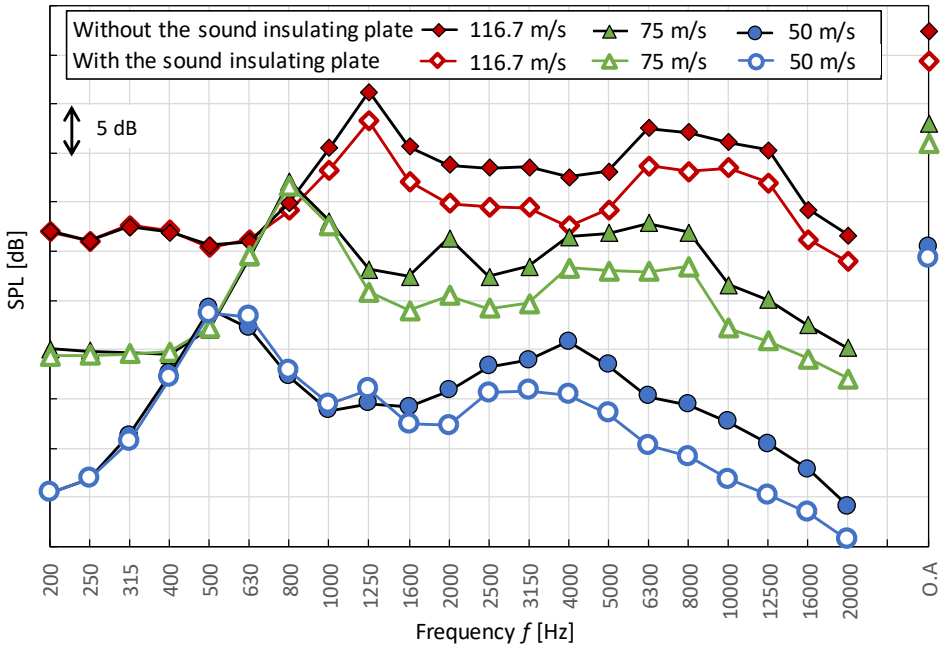

Figure 3.11 1/3 octave band frequency analysis of the noise from measured values of 1/10-scale pantograph without and with the sound insulating plate. Measured values at 116.7 m/s are plotted with red and white rhombus dots. Measured values at 75 m/s are plotted with green and white triangle dots. Measured values at 50 m/s are plotted with blue and white circle dots.

3.3.3.2. Sound insulating plate reduction effect

The theoretical reduction noise level of the sound insulating plate, $\Delta SPL_{pl,the}$, was estimated from Eqs. (3.11), (3.12) and (3.13), a reduction effect of the sound insulating plate was evaluated

Equation (3.11) indicated reduced noise level by a sound insulating plate with infinite length, ΔL. Here, the Fresnel number N is the ratio of the sound wavelength λ and the distance difference δ among a noise source, an edge of plate and a measurement point, of which the position were shown in Fig. 3.12(Maekawa 1962; Yamamoto and Takagi 1991). The distance difference δ was calculated by Eq. (3.12) and was changed by a noise source position, the relation between the noise source height h_N and the height of the edge of plate h_i in Fig. 3.12. Equation (3.13) indicated the reduction noise levels of a sound insulating plate with a limited length (Yamamoto et al. 1994). This was calculated from the sum of the noise contribution through the open area in the plane of the sound insulating plate. Equation (3.13) indicated the noise reduction of the square insulating board, which was shown as the separated area C_0, C_6, C_7 and C_8 in Fig. 3.13.

$$\Delta L(f) = \begin{cases} 10\log N + 13 & N \geq 1 \\ 5 + 8N^{0.45} & 0 \leq N < 1 \\ 5 - 8|N|^{0.4} & -0.3 \leq N < 0 \\ 0 & N < -0.3 \end{cases} \quad (3.11)$$

Where N [-]: the Fresnel number $(= 2\delta/\lambda = 2\delta f/a)$

δ [m]: the distance difference

λ [m]: the wavelength of sound$(= a/f)$

$$\delta = \begin{cases} b + c - d & h_N < h_E \\ -(b + c - d) & h_N \geq h_E \end{cases} \quad (3.12)$$

Where b [m]: a distance between noise source and edge of sound insulating plate

c [m]: a distance between edge of sound insulating plate and measurement point

d [m]: a distance between noise source and measurement point

$$\Delta SPL_{pl,the}(f) = -10\log_{10}\left\{10^{-\frac{\Delta L_{123}}{10}} + \left(10^{-\frac{\Delta L_{0-5}}{10}} - 10^{-\frac{\Delta L_{123}}{10}}\right) \times \left(10^{-\frac{\Delta L_{146}}{10}} + 10^{-\frac{\Delta L_{358}}{10}}\right)\right\} \quad (3.13)$$

Where the suffix shows the number open area. For example, ΔL_{123} means the reduction noise level when the areas except C_1, C_2, C_3 are assumed to be a sound insulating plate with infinite length.

The theoretical reduction noise level of the sound insulating plate was calculated by Eqs. (3.11) - (3.13) at each 1/3 octave band frequency region. In this study, the noise source of the pantograph was supposed to be set at its body and panhead. The panhead height was $h_t = 0.9\ D_p$ and the body height was $h_b = 0.5\ D_p$. For simple estimation of the ΔL_{146} and ΔL_{358} in Eq. (3.13), the sound insulating plate was assumed to be the square shape, of which the height was $h_i = 0.53\ D_p$ and the length was $l_p = 0.6\ l_i$ as shown in Fig. 3.13.

Figure 3.14 shows the theoretical and measured reduced noise levels by the sound insulating plate.

Figure 3.14 illustrates that the theoretical reduced noise levels by the plate are different due to a source position. At high frequency region, the theoretical values from the pantograph body increases, and, in contrast, those from its panhead decreases. This is why the Fresnel number, *N*, is changed at the high frequency. The sound insulating plate hides the pantograph body and prevent the sound from it to the measurement point, which leads the noise reduction effect to increasing at high frequency. However, the panhead of the pantograph can be seen from the measurement point and the sound radiated from its panhead is reduced by only the diffraction of the plate. This results in the decrease of the noise reduction at the high frequency, at which the sound wavelength is short, according to Eq. (3.11).

The measured values were the difference between without and with the sound insulating plate in Eq. (3.14).

$$\Delta SPL_{pl,mes} = SPL_{\,without\ plate} - SPL_{\,with\ plate} \tag{3.14}$$

In Fig. 3.14, the pantograph noise over about 1,250 Hz was reduced by the sound insulating plate, and the reduction level over 3,150 Hz was in the range between the theoretical values from its body and those from its panhead. The experimental reduction effect of the plate was small at the low frequency This is considered to be because the plate length is too short to reduce the intensity of the sound of which the wavelength is long. In this study, the plate length, l_i = 3.3 D_p, equals to the wavelength of sound at approximately 1,700 Hz, which may lead to decreasing the reduction effect at a low frequency range. The comparison of different wind velocity result shows that the noise reduction frequency range expands to low frequency and the noise reduction level at high frequency decreases by increasing the wind velocity. This is why the noise source position of the pantograph is changed by wind velocity. According to the Strouhal number shown in Eq. (3.2), the frequency of the pantograph noise increases, and a sound source may become able to receive the noise reduction effect of the plate. These results above show that the experimental noise reduction effect was small at low frequency and approximate to the theoretical values at high frequency.

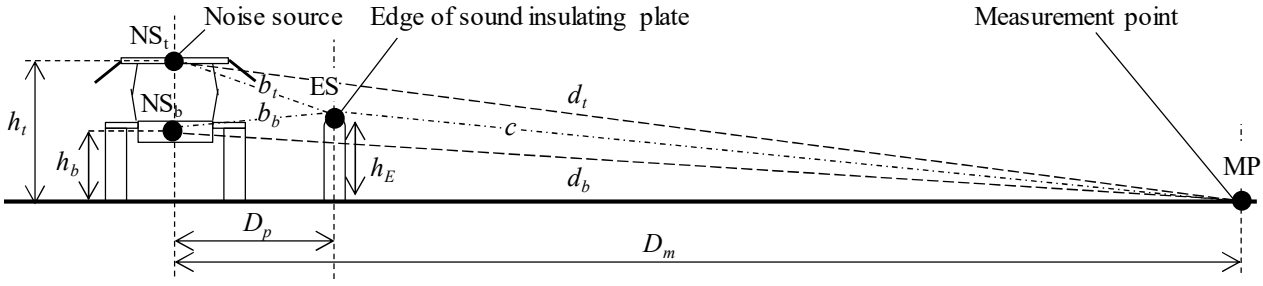

Figure 3.12 Positions of a noise source, an edge of plate and a measurement point. The distances, b_t and b_b, are between noise source and edge of sound insulating plate. The distance, c, is between edge of sound insulating plate and measurement point. The distance, d_t and d_b, are between noise source and measurement point. In this study, the noise source of the pantograph was supposed to be set its body NS_b and its panhead NS_t.

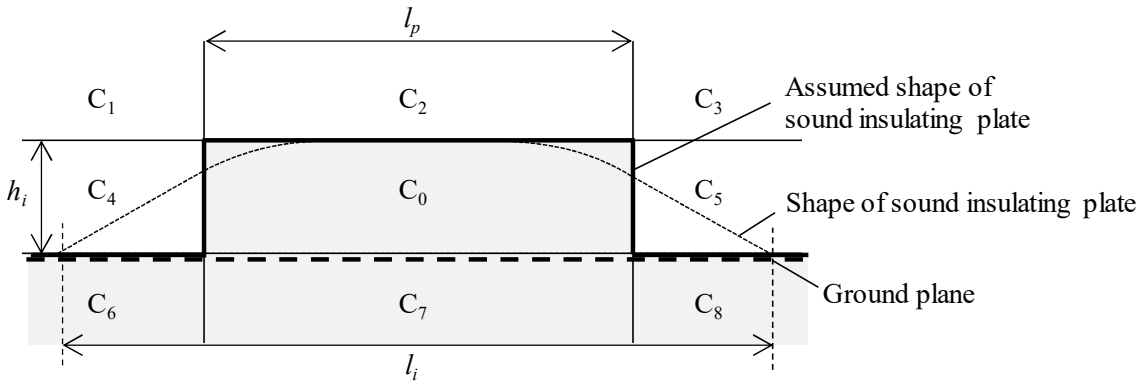

Figure 3.13 Image areas of sound insulating plate with limited length at the plate plane. Equation (3.12) indicates the noise reduction of the plate, which is shown as the separated area C_0, C_6, C_7 and C_8. The experimental real plate is shown as a dashed line. In this study, the plate shape was supposed to be the square area C_0, shown as the bold solid line, in order to easily calculate the noise reduction effect.

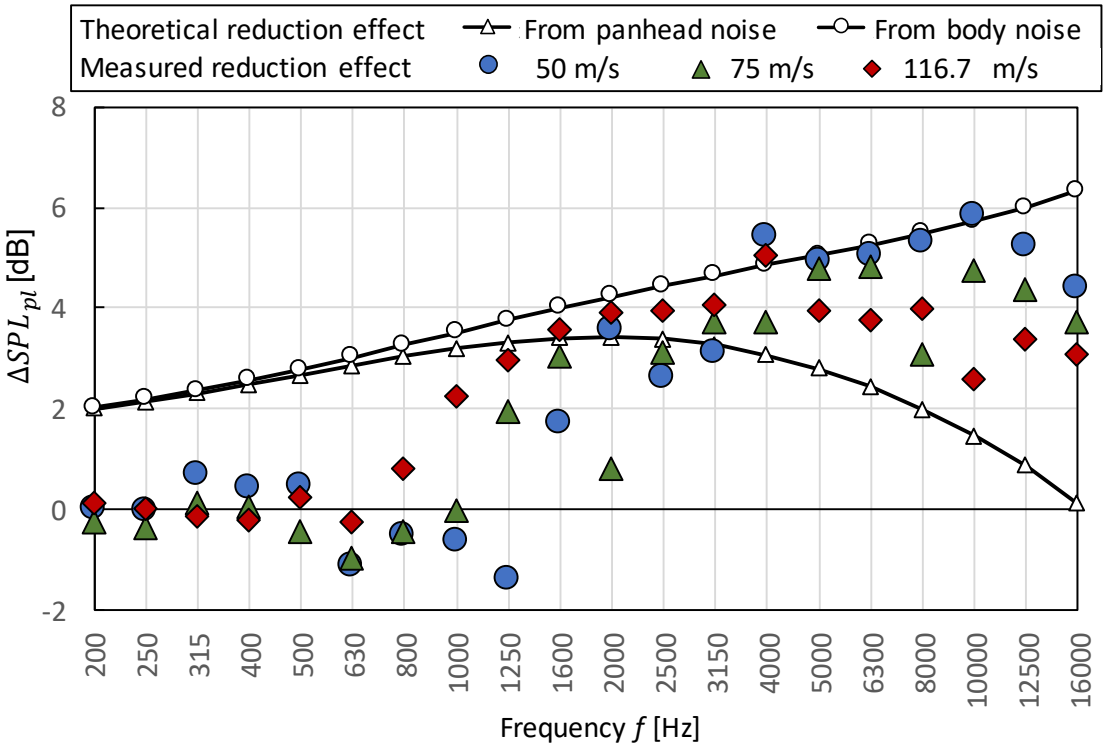

Figure 3.14 Theoretical and measured reduced noise levels by the sound insulating plate at 1/3 octave band frequency. Theoretical values from the pantograph's panhead noise and from its body noise are plotted with white triangle dots and white circle dots. Measured values at 50, 75 and 116.7 m/s are plotted with blue circle dots, green triangle dots and blue circle dots.

3.3.3.3. Estimation by similarity law

The noise levels of the full-scale pantograph without and with the sound insulating plate at the wind velocity U = 116.7 m/s were estimated from the measured noise levels of the 1/10 reduced-scale model at the wind velocity U = 50 m/s and U = 116.7 m/s, and the similarity law was evaluated. The value $SPL_{est,VdD}$ was calculated by using Eqs. (3.2) and (3.15). Equation (3.15) is transformed from Eq. (3.1) for adapting the wind velocity and model scale conversion. The value $SPL_{est,D}$ was calculated by using Eqs. (3.2) and (3.16) for adapting the only model scale conversion.

$$SPL_{est,VdD} = SPL_{mea,U=50m/s} + 60\log\left(\frac{116.7m/s}{50m/s}\right) + 20\log 10 \tag{3.15}$$

$$SPL_{est,D} = SPL_{mea,U=116.7m/s} + 20\log 10 \tag{3.16}$$

In addition, the noise level with the sound insulating plate was estimated by using the theoretical noise reduction effect of the sound insulating plate. The value $SPL_{est,VdD,red}$ was calculated by using Eqs. (3.2), (3.17). Equation (3.17) indicated the that the theoretical noise reduction of sound insulating plate for the pantograph body, $\Delta SPL_{b,the}(f)$, was subtracted from the estimated noise level of the pantograph without the sound insulating plate.

$$SPL_{est,VdD,red} = SPL_{mea,U=50m/s,w/o\ plate} + 60\log\left(\frac{116.7m/s}{50m/s}\right) + 20\log 10 - \Delta SPL_{b,the}(f) \tag{3.17}$$

Figure 3.15 shows the estimated noise levels of the full-scale pantograph without and with the sound insulating plate at the wind velocity U = 116.7 m/s. Figure 3.15(A) shows that the estimated noise level without the sound insulating plate from the values at 50 m/s, $SPL_{est,VdD}$, has same tendency as that from the value at 116.7 m/s, $SPL_{est,D}$. This leads the overall noise levels of $SPL_{est,VdD}$ to being with 0.4 dB difference from $SPL_{est,D}$. This was why the dominant peak noise was estimated precisely by using the wind velocity conversion as the sixth power of the wind velocity as a dipole sound source.

However, Fig. 3.15(B), which shows the pantograph noise with the sound insulating plate, indicates that $SPL_{est,VdD}$ at a low frequency region less than 400 Hz was higher than $SPL_{est,D}$. This leads the overall noise level of $SPL_{est,VdD}$ to being 2.5 dB higher than that of $SPL_{est,D}$ and showing that the noise reduction effect of the sound insulating plate was underestimated in the conversion of the wind velocity. This was caused by the frequency characteristics of the noise reduction effect of the sound insulating plate. In this study, the pantograph noise level in a low frequency range at 50 m/s was not acquired the noise reduction effect of the sound insulating plate in contrast to that at 116.7 m/s, as shown in Fig. 3.14. Therefore, $SPL_{est,VdD}$, at low frequency was higher by not including the noise reduction effect of the sound insulating plate. On the other hand, the estimated value by using the theoretical noise reduction effect, $SPL_{est,VdD,red}$, has same tendency of $SPL_{est,D}$. This leads the overall noise levels of $SPL_{est,VdD,red}$ to being with 0.8 dB difference from $SPL_{est,D}$. This was why the dominant peak noise

was estimated precisely by using the wind velocity conversion and the reduced noise level by the sound insulating plates.

This result illustrates that the sound insulating plate, of which the noise reduction effect has a frequency characteristic, made the actual noise level increase lower than the noise level conversion of wind velocity. This caused the noise reduction effect of the sound insulating plate to be underestimated. This problem could be solved by subtracting the theoretical reduction noise level of the plate from the estimated noise level of the pantograph itself. This leads the pantograph noise with the sound insulating plate to being estimated within 0.8 dB difference.

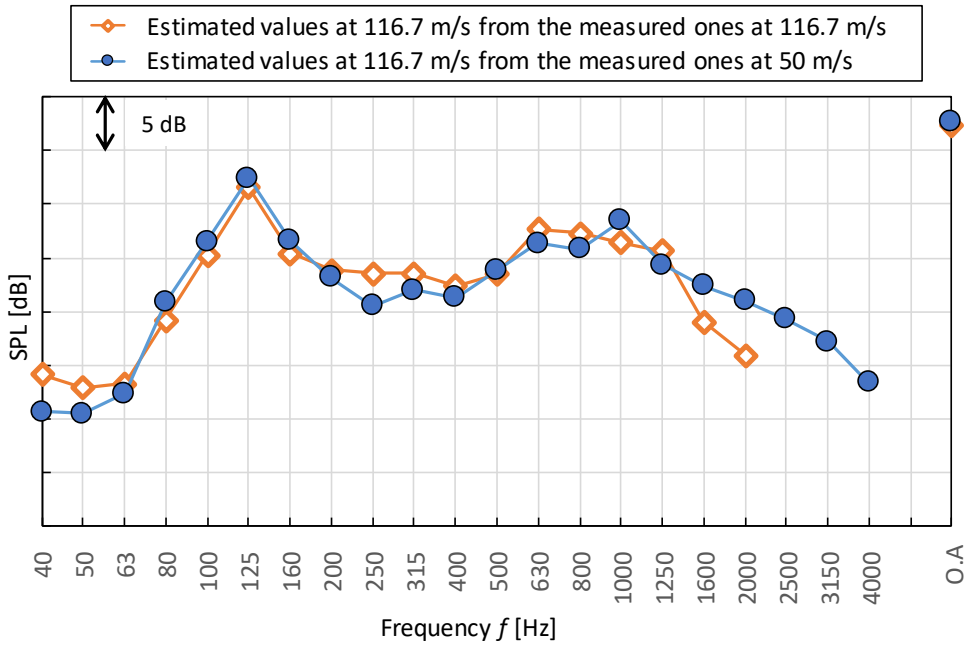

(A) Pantograph without the sound insulating plate

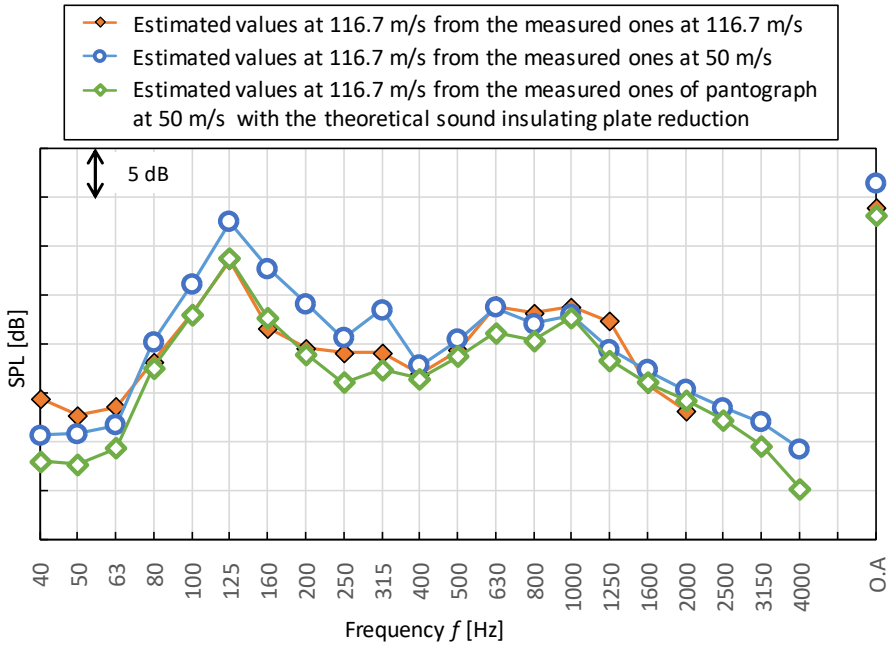

(B) Pantograph with the sound insulating plate

Figure 3.15 1/3 octave band frequency analysis of the noise from measured and estimated values of 1/10-scale pantograph without and with the sound insulating plate. Estimated value from measured values at 116.7 m/s by Eqs. (3.2) and (3.16) are plotted with orange and white rhombus dots. Estimated values from the values at 50 m/s by Eqs. (3.2), (3.15) are plotted with blue and white circle dots. Estimated values from the values at 50 m/s by Eqs. (3.2), (3.17) are plotted with rhombus square dots.

3.4. Conclusion

We measured the aerodynamic noise radiating from cylinders without and with periodic holes and a pantograph model without and with a sound insulating plate when the flow was faster than 100 m/s in a low-noise high-speed wind tunnel to assess aerodynamic noise sources and the wind velocity conversion of the similarity law.

The background noise of the wind tunnel was proportional to the sixth power of wind velocity until 60 m/s and became proportional to the eighth power in a high-speed region. This dependence shows that the aerodynamic sound source of the vortex generated from the shear layer at the nozzle became dominant as a quadrupole sound source.

From a measurement of the cylinders without and with periodic holes, in the Reynolds number range, where the vortex formation is unchanged, the noise level of the cylinder increased in proportion to the sixth power of wind velocity as a dipole sound source, and the noise reduction effect due to the change in flow structure, such as periodic holes, also continued regardless of wind velocity. However, the second peak noise radiated from the cylinder was in proportion to the eighth power of wind velocity over 130 m/s and was underestimated by using the wind conversion based on a dipole sound source.

The noise level of the pantograph model with the sound insulating plate increased in proportion to lower than the sixth power of wind velocity in contrast to the pantograph model itself as a dipole sound source. This is why the increase of the actual dominant noise level at a low frequency was reduced to less than the sixth power of wind velocity by the sound insulating plate. The plate was more effective at reducing noise at a high frequency than at a low one. In addition, by increasing the wind velocity, the dominant frequency of the pantograph noise shifted higher. These leads the dominant noise level to be affected by the noise reduction of the sound insulating plate. This caused the reduction effect of the sound insulating plate to be underestimated by 2.5 dB due to the noise level conversion of wind velocity. To solve this problem, the plate's theoretical reduction noise level, which was calculated by using the Fresnel number, was subtracted from the estimated noise level of the pantograph itself. This leads the pantograph noise with the sound insulating plate to be estimated within 0.8 dB difference.

These results indicate that the noise level radiated from cylinders and pantograph increased steadily in proportion to the sixth power by dipole sound at a wind velocity up to 116.7 m/s. However, it was found that noise at higher frequency may increase in proportional to the sum of the sixth and eighth powers of wind velocity because a quadrupole sound source increases due to the shorter turbulent correlation length. And, it was indicated that the noise level of objects with a sound insulating structure is lower than the sixth power of wind velocity. It was found to be effective to add the theoretical noise reduction by the diffraction for the estimation of the actual noise level of objects with a sound insulating structure. In conclusion, there is the possibility that a noise level estimated by wind velocity conversion generates differences from the actual noise level. Therefore, we should carefully use the similarity law when we estimate the running full-scale noise level from a reduced-scale model at a different wind velocity.

Chapter 4
Measurement of Pressure Fluctuation Distribution around a Square Cylinder with Pressure Sensitive Paint

List of symbols

A Stern–Volmer coefficient [-]

A_0 Wave amplitude [-]

B Stern–Volmer coefficient [-]

C Pressure-fluctuation propagation speed [m/s]

C_2 Coefficient for Strouhal number in a turbulent boundary layer [-]

C_{XY} Cross-correlation function [-]

D Square cylinder standard width [mm]

H_w Wind tunnel height [mm]

I Luminescent intensity [-]

L Square cylinder standard height [mm]

L_w Wind tunnel length [mm]

M Mach number (= U/a) [-]

N_{FFT} FFT sampling data [-]

P Pressure [Pa]

P_{XX} Power spectrum [Pa^2]

St Strouhal number [-]

T Temperature [K]

U Freestream velocity [m/s]

U_c Vortex convection velocity [m/s]

W_w Wind tunnel width [mm]

X Frequency spectrum [-]

Y Frequency spectrum [-]

a Sound velocity [m/s]

f_{peak} Peak frequency [Hz]

f_s Sampling frequency [Hz]

Δf Frequency resolution [Hz]

h Square cylinder height [mm]

k Discrete frequency [Hz]

n_2 Coefficient for Strouhal number in a turbulent boundary layer [-]

w Square cylinder width [mm]

x Streamwise position [m]

y Width position [m]

Ψ Wave function [-]

δ Boundary layer thickness [mm]

λ Propagating wavelength [m]

σ Singular value of matrix [-]

γ Phase-correction constant [-]

γ_{XY}^2 Coherence [-]

ϕ_{XY}^2 Phase shift [rad]

Subscript

ref Reference condition

mes Measured value

the Theoretical value

Abbreviation

COP Coherent output power

FFT Fast Fourier Transform

POD Proper Orthogonal Decomposition

PSD Power Spectral Density Function

PSP Pressure Sensitive Paint

SNR Signal-to-Noise Ratio

$\mathbf{A}$ Matrix ($m \times n$)

$\mathbf{U}$ Eigenvector matrix of $\mathbf{A}\mathbf{A}^{\mathrm{T}}$

$\mathbf{V}$ Eigenvector matrix of $\mathbf{A}^{\mathrm{T}}\mathbf{A}$

4.1. Introduction

One of the important performances of products related to fluids, such as fans and transportation equipment, is quietness. Their rotation and/or running speed is becoming faster, aerodynamic noise intensity increases as the relative speed between their body surface and the surrounding fluids increases. Therefore, it is necessary to reduce aerodynamic noise for acquiring high-speed rotation and/or running speed with a quiet environment. Detailed knowledge of the properties of a sound source and the sound distribution is required for the reduction in aerodynamic noise.

The Lighthill-Curle equations (Lighthill 1952; Curle 1955) show that a sound source of aerodynamic noise is changed from a dipole sound source into a quadrupole sound source depending on the Mach number M (= U/a), which is the ratio between the freestream velocity U and the sound velocity a. Aerodynamic noise is found to be mainly generated as a dipole sound source from pressure fluctuations on a surface in the low-speed region under $M = 0.3$ (Iida et al. 2000). Therefore, it is important to measure distributions of surface-pressure fluctuation on a test model for the assessment and the detection of aerodynamic noise sources. Conventionally, pressure fluctuations are measured by using pressure sensors set in orifices on a surface of a test model. This measurement technique is highly accurate and reliable. However, it is difficult to be applied to a curved surface, and to acquire the pressure distribution across a whole surface, multiple sensors and/or repeated measurements are necessary.

Recently, as an alternative technique for measuring surface-pressure fluctuations to that using pressure sensors (with the problems described above), a technique using a pressure-sensitive paint (PSP) has been developed (Bell et al. 2001; Liu at al. 2005; Asai and Yorita 2011; Gregory et al. 2014). The PSP measurement allows us to estimate time-series surface-pressure distributions by measuring the varying intensity of the luminescent light from the dye in PSP excited by an excitation light. The surface-pressure distributions are measured by capturing this luminescence by using a camera, and a two-dimensional (2D) surface-pressure distribution with higher spatial resolution than that possible by using point measurement with a conventional pressure sensor can be obtained.

Measurements by PSP have mostly been applied to transonic and supersonic flows (Nakakita et al. 2012; Sugioka et al, 2015). In recent years, however, PSP has been applied to unsteady phenomena in the low-speed region (Liu 2003; Asai and Yorita 2011; Nakakita 2011; Peng et al. 2016). Applying PSP to unsteady phenomena in the low-speed range faces two major problems: time response of PSP and low signal-to-noise ratio (SNR) due to low dynamic pressure. Regarding the former problem, unsteady PSP has been developed, and PSPs with quick response time, which can adequately follow pressure fluctuation in the order of kilohertz (Gregory et al. 2001; Kitashima et al. 2014; Sugioka et al. 2018, 2018a, 2018b, 2021; Uchida et al. 2021) have been demonstrated. Regarding the latter problem, several methods for improving SNR of PSP have been developed. A simple one is a phase-lock measurement that accumulates synchronized snapshots with a reference signal out of the targeted periodic phenomenon. A fast Fourier transform (FFT) was applied to PSP images (Nakakita 2011), and subtracting power spectral density (PSD) of the wind-off images from that of the wind-on images is shown to be an effective way to reduce the noise component (Nakakita 2013). Recently, the spectrum estimation technique using cross-corelation

was also devised and the noise floor was further reduced while it requires a lot of samples (Ozawa at al. 2019). Meanwhile, coherent output power (COP), which is given by a cross correlation between time-series pressure measured by PSP and a reference signal, was employed for the measurement of pressure fluctuations associated with tonal trailing-edge noise for a two-dimensional NACA 0012 airfoil (Noda et al. 2018). Accuracy of an unsteady PSP measurement in the low-speed region has thus been improved. However, there are still few examples of applying a PSP measurement to a complex shape for evaluation of a sound-source distribution and for comprehension of an unsteady phenomenon in the low-speed region.

In this study, the pressure fluctuations distribution on the floor surface behind a square cylinder in the turbulent boundary layer was measured at the Mach number around $M = 0.3$. These dominant pressure fluctuations are found to be generated by the Kármán vortex shedding from the cylinder sides (Sakamoto and Arie 1983; Wang and Zhou 2009). From the previous study, these flows around a square cylinder on the surface are generally classified according to three parameters (Sakamoto and Arie 1983). One is the Reynolds number, which is calculated from $\mathrm{Re} = U_\infty w/\nu$ with U_∞ the free-stream velocity, w the side length for square cylinders, and ν the kinematic viscosity. For Re > 2,000, the wake flow is turbulent. Another parameter is the cylinder's aspect ratio h/w, with the cylinder height h. The other parameter is the ratio of between the cylinder height h and the boundary layer thickness δ, h/δ. Generally, the threshold for thin boundary layers is accepted at $h/\delta = 3.0$ (Porteous et al. 2014; Kindree et al. 2018). The vortex shedding frequency of square cylinders is found to be independent of h/δ in the thin boundary layers $h/\delta \geq 3.0$, but the frequency of the Kármán vortex shedding is found to be lower with the ratio h/δ decreases in the boundary layer $h/\delta < 3.0$. The boundary layer thickness also influences the wake streamwise vortical structures generated by the separations around the top of the cylinder and its corner near the base floor (Bourgeois et al. 2011; Hosseini et al. 2013; El Hassan et al. 2015; Wang 2019; Barbara et al. 2020; Cheng et al. 2022). To examine the PSP's frequency response and accuracy of measured pressure fluctuations, the four types of the square cylinders were examined in the same turbulent boundary layer, which means that the three different aspect ratios ($h/d = 3.5, 7.0, 14.0$) and the 3 conditions of relative boundary layer thickness ($h/\delta = 1.14, 2.28, 4.56$) was measured. The impact of these parameters to the peak frequencies and distribution of the pressure fluctuations generated by the Kármán vortex from the square cylinder was examined. The main mode of the peak pressure fluctuations distribution was calculated by the singular value decomposition.

4.2. Experimental Apparatus

4.2.1. Unsteady Pressure-sensitive Paint (PSP)

Pressure-sensitive paint is a pressure sensor utilizing a photochemical reaction that involves luminescent molecules (luminophores) and binder (mainly polymer). The luminophores emit luminescence when illuminated by excitation light with an appropriate wavelength. Since the intensity of emitted light from the luminophores depends on the partial pressure of oxygen, the air pressure over the PSP can be calculated from the luminescent intensity captured by a camera. A ceramic PSP combined with a quick-response polymer is used in this study (Kitashima et al. 2014; Ozawa et al. 2019; Pandey and Gregory

2015; Sakaue et al. 2011; Scroggin et al. 1999; Sugioka et al. 2018, 2018a, 2018b, 2019; Uchida et al. 2021). Pressure sensitivity of the PSP (measured by static calibration) was 0.73 %/kPa. Moreover, according to frequency-response measurements using an acoustic resonance tube, frequency response of approximately 5,420 Hz was guaranteed (Sugimoto et al. 2017). In the present study, a frequency analysis is restricted to the maximum of 4,000 Hz. This cutoff frequency is higher than the peak frequency of the Kármán vortex shedding from the square cylinder in this study.

4.2.2. Experimental Model and Measurement System

The pressure fluctuations distribution on the floor surface behind a square cylinder in the turbulent boundary layer was measured in a low-noise high-speed wind tunnel (Hitachi 2014; Matsui, et al., 2017, 2020). The test section of the wind tunnel has the dimensions of 600 mm (W_w) × 400 mm (H_w) × 2,000 mm (L_w), and the maximum freestream velocity is 116.7 m/s.

Photographs and images of the test model are shown in Figure 4.1. Four square cylinders with different sizes are used and the frequency of the Kármán vortex shedding is used. The detailed model parameters and test conditions are shown in Table 4.1. The model cross-sectional side length w and its height h are set to acquire the aspect ratio w/h = 3.5, 7.0, 14.0, based on the standard width D = 6.5 mm and the standard height L = 45.5 mm. During the experiment, the model is fixed at the center of the circle floor surface on which PSP measurement can be applied. The diameter of the circle floor is 250 mm. Figures. 4.1(a), (d) show that cylinders and the floor on the splitter plate were vertically set to reduce the boundary layer thickness and to easily capture the images of the PSP painted on the floor surface.

The PSP measurement system shown in Figs. 4.1(a) and (c) is explained as follows. Three UV-LEDs (IL-106, HARDsoft) were used with a condenser lens (HSO-PL-180-UV, HARDsoft) as an excitation light source for the PSP. The LEDs were set at 800 mm horizontal side from the floor surface. A high-speed camera (V2012, Phantom) was used as a light-emission detector. The camera was fitted with a 50-mm-focal-length lens (Nikkor 85 mm f 1.4, Nikon) and a 590-nm long pass filter (9022621, Laser create Corp.). Images were captured with 512 × 512 pixels. Spatial resolutions were 0.59 mm/pixel. The number of images recorded during each run was 95,178. Its capture frequency was adjusted to be approximately 12 times of the expected peak frequency of the Kármán vortex shedding, which was estimated from the Strouhal number of the two-dimensional square cylinder, $St = f_{peak}w/U_\infty = 0.13$ (Okajima 1982), so that the peak pressure fluctuations could be precisely measured.

Unsteady surface pressure was measured using a Kulite pressure transducer (XCQ-062-5SG), which was flush-mounted on the floor surface. The installation position was x/w = 1.8, y/w = 0.5 where the origin point was located at the model center, as shown in Fig. 4.1(e). The cut off frequency of the Kulite sensor was 150 kHz, which is significantly higher than that of the unsteady PSP. The sampling frequency was set at 96 kHz. The data from the pressure transducer was amplified and recorded with a data recorder (LX-100 Series, TEAC). The high-speed camera and pressure transducer measurements were synchronized by a trigger signal produced by the start of camera recording.

Figure 4.2 shows the velocity profile and the turbulent intensity at the vertical direction on the model set position without the model. Velocity measurements by a hot-wire anemometer (Kanomax, Model

7000Ser) and an I-shaped probe show that the boundary-layer thickness δ on the model set position were δ = 20 mm without the model.

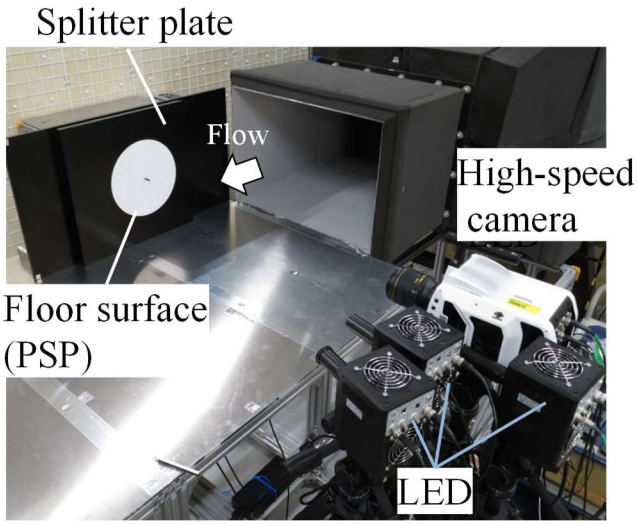

(a) Setup of measurement system

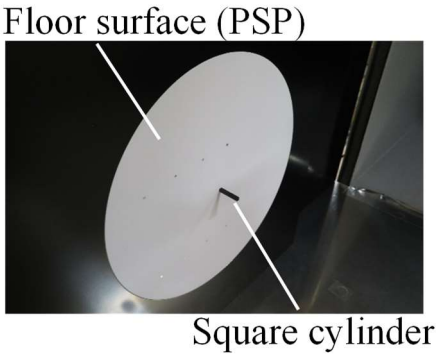

(b) Floor surface and square cylinder

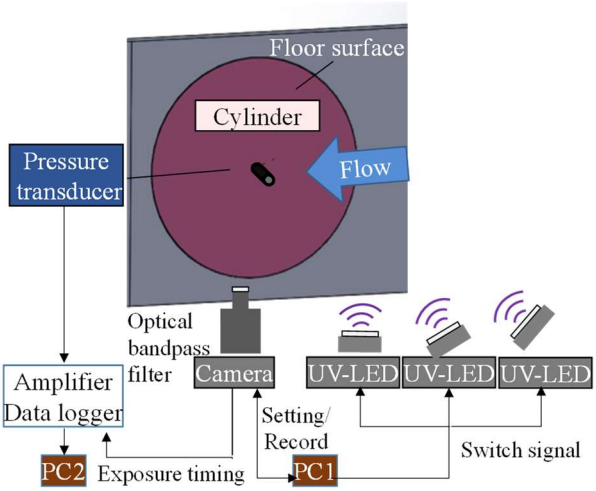

(c) Diagram of measurement system

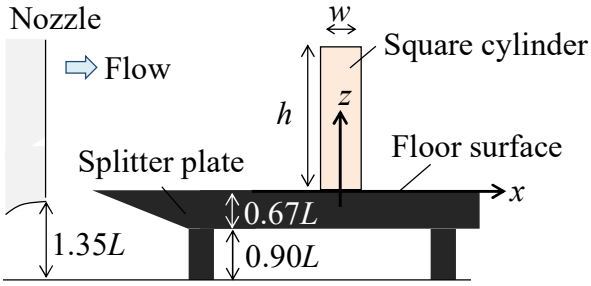

(d) Top view of splitter plate and cylinder position

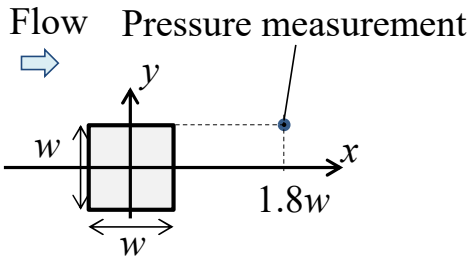

(e) Pressure-sampling point

Figure 4.1 Experimental model and measurement system

Table 4.1 Square cylinder size and measurement conditions

		(1)	(2)	(3)	(4)
Cylinders	Width w [mm]	$D/2$	D		
	Height h [mm]	L	$4L$	$2L$	L
	Aspect ratio h/w [-]	7.0	14	7.0	3.5
Wind velocity U_∞ [m/s]		100	116.7		
Reynolds number Re [$\times 10^5$]		2.2	5.1		
Expected peak frequency f_{peak} [Hz]		4,000	2,334		
Camera	Frame rate f_s [Hz]	48,000	28,000		
	Exposure time [μs]	20	35		
Kulite	Sampling frequency [Hz]	96,000			

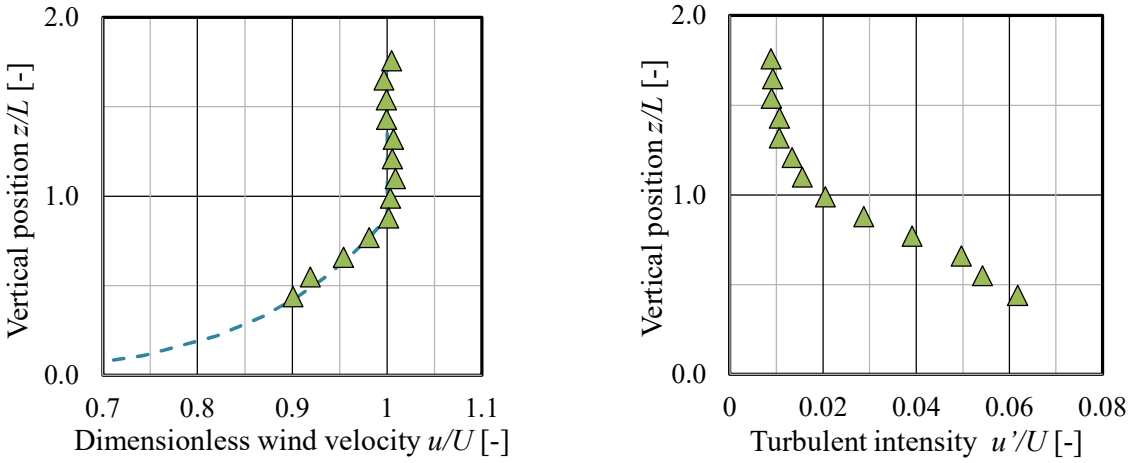

(a) Velocity profile (b) Turbulent intensity

Figure 4.2 Velocity profile and turbulent intensity on the model set position

4.2.3. Data Analysis

4.2.3.1. Pressure-intensity relation

The time-series pressure distribution was calculated from the captured PSP images by using the Stern–Volmer equation, defined as

$$\frac{I_{\mathrm{ref}}}{I} = A(T) + B(T)\frac{P}{P_{\mathrm{ref}}} \tag{4.1}$$

where I is luminescent intensity, P is pressure, and the subscript "ref" stands for reference conditions at which P and I are known. $A(T)$ and $B(T)$ are the Stern–Volmer coefficients, which depend on temperature. In this study, the images obtained by averaging the wind-on images and subtracting the dark images, which were captured without the excitation light, were used as the intensity of the reference image, I_{ref}.

This method makes it possible to reduce the influence of the change in luminescent intensity due to the temperature change or photo-degradation of the luminophores, but it only makes it possible to estimate the pressure fluctuations.

4.2.3.2. Power distribution

The overall flow of PSP data-analysis process is shown in Figure 4.3. After spatial binning of the time-series pressure distribution, PSD of the pressure fluctuations was calculated from the time-series pressure distribution by using an ensemble averaging FFT, as proposed by Nakakita (2011, 2013). In this method, images corresponding to an entire time-series data set are split into a smaller number of segmented data sets. The FFT processing was applied to time-series pressure data of N_{FFT} images. At that time, the split data sets were overlapped on neighboring data sets. The frequency resolution was determined as follows:

$$\Delta f = \frac{f_s}{N_{FFT}} \tag{4.2}$$

The power spectrum, $P_{XX}(f)$, which was calculated by using the frequency spectrum, $X(f)$, and its complex conjugate, $X^*(f)$, obtained by FFT, was ensemble averaged, and PSD was calculated as follows:

$$PSD(f) = \frac{\langle P_{XX}(f) \rangle}{\Delta f} = \frac{\langle X(f)X^*(f) \rangle}{\Delta f} = \frac{\langle X(f)X^*(f) \rangle}{f_s/N_{FFT}} \tag{4.3}$$

The Hanning window was used as a window function in the FFT analysis, and the power attenuation by the window function was corrected. In this analysis, the background spectrum subtraction obtained by wind-off images (Nakakita 2013) was not adopted because it was difficult to understand the noise floor. Table 4.2 shows the FFT analysis conditions. The sampling data (N_{FFT}) was changed by the cross-sectional cylinder size w, and the frequency resolution Δf of the PSP and Kulite measurements were set almost the same as each other.

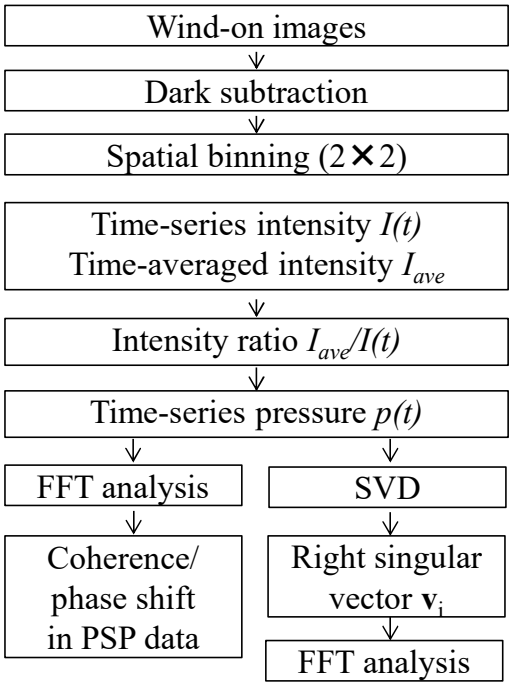

Figure. 4.3 Flow chart of processing of PSP data

Table 4.2 FFT analysis conditions

Cylinders		Sampling rate f_s [Hz]	Sampling data N_{FFT}	Average	Frequency resolution Δf [Hz]
(1)	PSP	48,000	1,024	100	46.9
	Kulite	96,000	2,048	100	46.9
(2)-(4)	PSP	28,000	1,024	100	27.3
	Kulite	96,000	4,096	100	23.4

4.2.3.3. Coherence and phase shift

Coherence represents degree of the correspondence between signals *x* and *y,* and phase shift represents the difference between the phases of the two signals (Bendat and Piersol, 1980; Marple, 1987). Coherence, $\gamma_{XY}^2(f)$, and phase shift, $\phi_{XY}(f)$, are defined as follows:

$$\gamma_{XY}^2(f) = \frac{|\langle C_{XY}(f)\rangle|^2}{\langle P_{XX}(f)\rangle\langle P_{YY}(f)\rangle} = \frac{|\langle X^*(f)Y(f)\rangle|^2}{\langle X(f)X^*(f)\rangle\langle Y(f)Y^*(f)\rangle} \tag{4.4}$$

$$\phi_{XY}(f) = \tan^{-1}\left(\frac{Q_{XY}(f)}{K_{XY}(f)}\right) = \tan^{-1}\left(\frac{\mathrm{Im}(C_{XY}(f))}{\mathrm{Re}(C_{XY}(f))}\right) \tag{4.5}$$

where $\langle C_{XY}(f)\rangle$ is the ensemble-averaged cross-correlation function.

The cross-correlation function $C_{XY}(f)$, which is calculated using the frequency spectra, $X(f)$ and $Y(f)$, of the two signals *x* and *y,* was ensemble averaged in this calculation. The pressure dataset captured by the PSP was separated into as an *x* signal, and the PSP data around the pressure taps was used as a *y* signal.

4.2.3.4. Singular-value decomposition analysis

Singular-value decomposition (SVD) is the decomposition of a $m \times n$ matrix $\boldsymbol{A}$ into its singular values as well as its left and right singular vectors, as shown in the following equation:

$$\mathbf{A} = \mathbf{U}\sum\mathbf{V}^T = \sum_{i=1}^{N}\mathbf{u}_i\sigma_i\mathbf{v}_i^T \tag{4.6}$$

where the $\sigma_1 > \sigma_2 > \cdots > \sigma_{\min\{n,m\}} > 0$ is the singular value of matrix **A**. $\mathbf{U} = [\mathbf{u}_1, \mathbf{u}_2, \ldots, \mathbf{u}_m]$ is the eigenvector matrix of $\mathbf{AA}^T$, while $\mathbf{V} = [\mathbf{v}_1, \mathbf{v}_2, \ldots, \mathbf{v}_n]$ is the eigenvector matrix of $\mathbf{A}^T\mathbf{A}$ and so-called as the right eigenvector matrix.

These decomposed components are consistent with those of POD method (Lumley 1967) used in a fluid analysis. SNR can be improved by excluding noise modes from decomposed modes and reconstructing data. Additionally, the right-side singular vector $\mathbf{v_i}$ has the time-evolution information for each mode. The FFT result of the right-side singular vector $\mathbf{v_i}$ from SVD decomposition process, which shows the spectral data of the pressure variation frequency peak associated with the dynamic nature of the flow, was extracted for comprehension of the flow structure and reduce the noise level in series of studies (Peng et al. 2016; Sugioka et al. 2019). In this study, the SVD was applied to 6,000 wind-on images. The two main modes, which has the maximum PSD data within the frequency tolerance band $f_{peak,\mathrm{PSP}} \pm 2\Delta f$ from the FFT result of the right-side singular vector $\mathbf{v_i}$, were extracted for comprehension of the flow dynamic phenomena.

4.3. Results and Discussion

4.3.1. Pressure Fluctuations

4.3.1.1. Comparison with PSP and pressure transducer

Figure 4.4 shows the PSD of the pressure fluctuation measured by the unsteady pressure transducer and PSP near the pressure tap. The measured values by PSP are found to have a similar trend to these by the pressure transducer up to 5,000 Hz in all conditions. Noise level of the PSP used in this study would be approximately 50-100 Pa^2/Hz. In each condition, the peak of pressure fluctuations generated by the Kármán vortex shedding from the square cylinder can be observed.

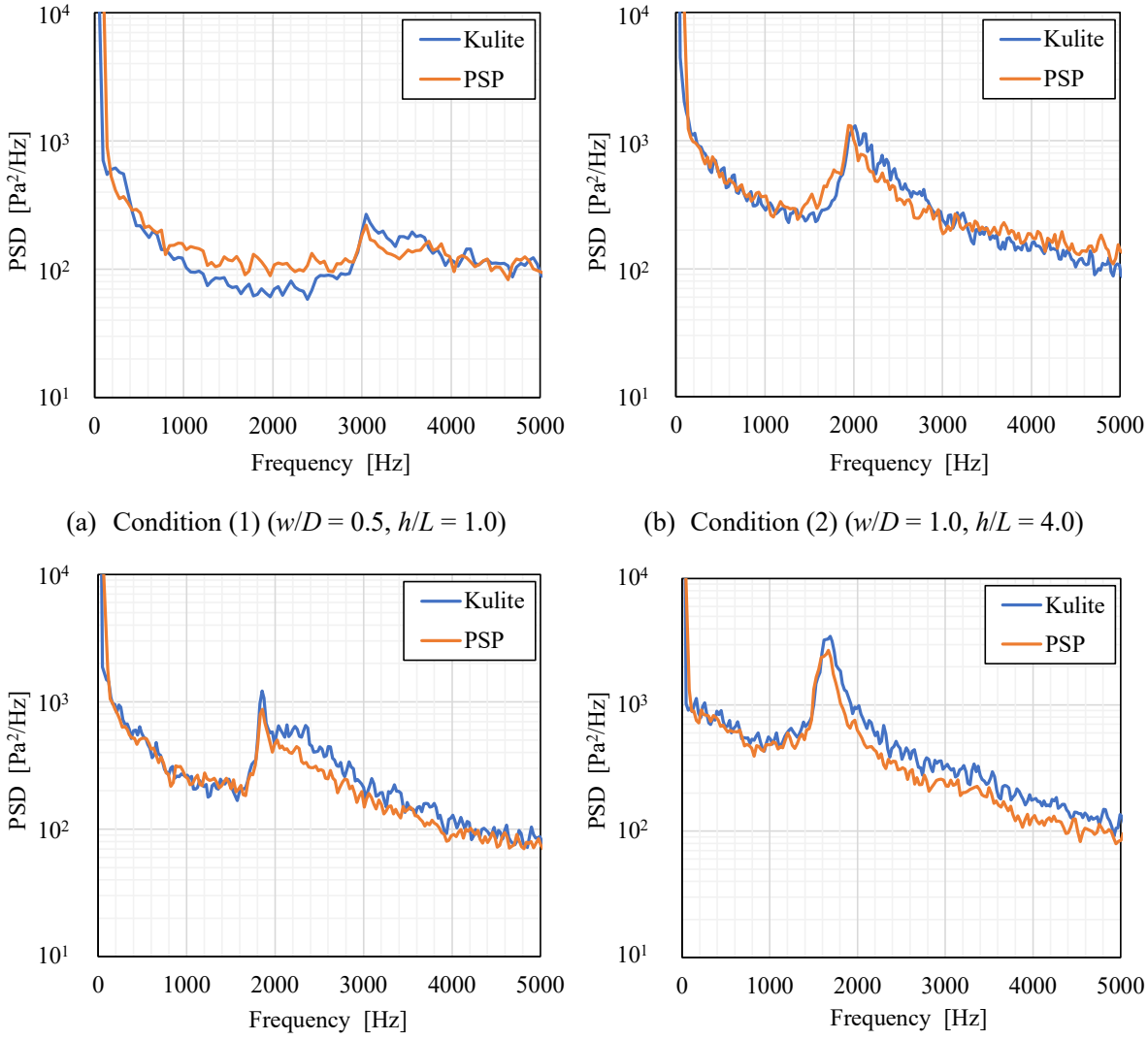

(a) Condition (1) (w/D = 0.5, h/L = 1.0)

(b) Condition (2) (w/D = 1.0, h/L = 4.0)

(c) Condition (3) (w/D = 1.0, h/L = 2.0)

(d) Condition (4) (w/D = 1.0, h/L = 1.0)

Figure 4.4 Comparison of PSD values measured by pressure transducer and PSP.

Table 4.3 shows the PSD values of the peak obtained from PSP and unsteady pressure transducer under each condition. The peak frequencies measured by the PSP and pressure transducer were almost the same as each other in all the conditions. Especially, the peak pressure fluctuation at 3,047 Hz can be observed by the PSP in the condition (1). The PSD values measured by PSP were 0.7-0.8 times lower than those measured by the pressure transducer under the conditions (1), (3) and (4). This would be considered caused by the spatial binning analysis and/or the model vibration generated by hitting high-speed flow. The measurement uncertainty of the PSP was estimated to 1.9% from the standard deviation of the average pressure measured by the pressure tap because the pressure fluctuation was calculated by using averaging the wind-on images as the intensity of the reference image in this study.

Table 4.3 Peak frequency and PSD values obtained from PSP and pressure transducer

	Cylinder				Kulite		PSP	
	w/D	*h/L*	*h/w*	h/δ	Peak frequency $f_{peak,kulite}$ [Hz]	PSD_{kulite} [Pa^2/Hz]	Peak frequency $f_{peak,PSP}$ [Hz]	PSD_{PSP} [Pa^2/Hz]
(1)	0.5	1.0	7.0	1.14	3,047	267	3,047	220
(2)	1.0	4.0	14	4.55	2,016	1,306	1,941	1,313
(3)	1.0	2.0	7.0	2.28	1,852	1,216	1,859	876
(4)	1.0	1.0	3.5	1.14	1,688	3,483	1,668	2,707

4.3.1.2. Peak frequency of square cylinder with different sizes

Table 4.3 presents that the peak frequency was observed to be lower with the lower cylinder height *h* in the spite of the common square cylinder width *w* in the conditions (2)-(4). This is due to the difference of the ratio of between the cylinder height *h* and the boundary layer thickness δ, h/δ. Sakamoto and Arie (1972) found that the peak frequency of the Kármán vortex shedding from the cylinders in the thick boundary layer is changed by the cylinder aspect *w/h* and the boundary-layer characteristics h/δ due to the vortex formation. Their experiment result leads to the following empirical equation of the Strouhal number *St* under the condition, $2 < w/h < 8$, and $0.2 < h/\delta < 1.6$.

$$St_{the} = C_2 \left(\frac{h}{w}\right)^{n_2}, \tag{4.7}$$

where the coefficients C_2 and n_2 are functions of h/δ alone and are given in Figure 4.5.

Table 4.4 shows the comparison of the measured and theoretical peak frequencies. Theoretical peak frequencies were calculated by the Equation (4.7). In the condition (3), which was out of the region of h/δ, the coefficients C_2 and n_2 were extrapolated by the cubic and linear function of h/δ, respectively. In the conditions (1), (3) and (4), the measured and theoretical peak frequencies were found to be almost the same as each other. Therefore, the peak frequencies of the cylinders in the turbulent boundary layer were found to be changed by the cylinder aspect *w/h* and the boundary-layer characteristic h/δ as same as the precious study.

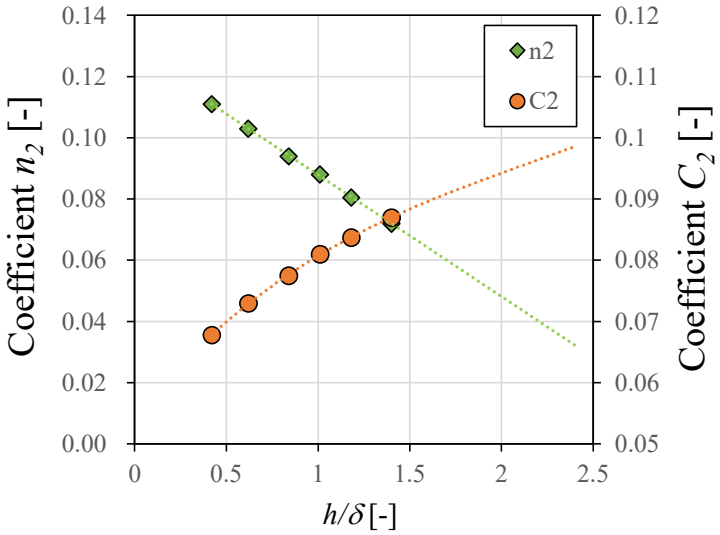

Figure 4.5 Relation between coefficients C_2 and n_2. Plots are given from the reference (Sakamoto and Arie 1983) and the dashed line was the approximated line from the plots. C_2 and n_2 were extrapolated by the cubic and linear function of h/δ, respectively.

Table 4.4 Peak frequency and PSD values obtained from PSP and pressure transducer

	Cylinder				Peak frequency	Wind velocity	Measured peak	Theoretical peak
	w/D	h/L	h/w	h/δ	$f_{peak,PSP}$ [Hz]	U [m/s]	frequency St_{PSP} [-]	frequency St_{the} [-]
(1)	0.5	1.0	7.0	1.14	3,047	100	0.099	0.098
(2)	1.0	4.0	14	4.55	1,941	116.7	0.108	-
(3)	1.0	2.0	7.0	2.28	1,859	116.7	0.104	0.105
(4)	1.0	1.0	3.5	1.14	1,668	116.7	0.093	0.092

4.3.1.3. Pressure fluctuation distribution at peak frequency

Figure 4.6 shows the PSD distribution at the peak frequency in each condition. Figure 4.7 shows the PSD profile in the streamwise line at y/w = 0.5 and the spanwise line at x/w = 1.8, shown the dashed line in Fig. 4.6.

Figure 4.7(b) illustrates that the 2 high-pressure-fluctuation areas were observed behind the square cylinder at the y/D= ±0.5 because the Kármán vortex shedding from the square cylinder in all the conditions. Figure 4.7(a) shows that the peak PSD values on both sides were almost the same as each other, and the peak PSD value was seen around at the streamwise position x/w = 2.0 in all the conditions.

Compared with the cylinders with the same cylinder width w (conditions (2)-(4)), the peak PSD value in the conditions (4) was more than twice as high as these at the other conditions. The high-pressure fluctuation area was only observed at around the streamwise position x/w = 2.0 and not to be spread into the downstream in x/w > 7.0. This will be caused by the low cylinder height. In the condition (4), the flow from the upper end of the square cylinder is thought to become dominant in the wake rather than that from the square cylinder side due to the low cylinder height.

This phenomenon was observed in the previous study (Porteous et al. 2017; Sumner et al. 2017). Sumner et al. (2017) show that the increasing influence of the lower-momentum, viscous flow within the boundary layer has a strong effect on the flow field of the shorter square cylinder. The free-end flow field and its associated downwash was found to move closer to the ground plane and begin to have a greater influence on the near-wake flow field within the boundary layer and close to the ground plane. This influence can be seen in the development of vortex downstream of the prism-wall junction, where it becomes progressively smaller as the square cylinder aspect is shorter and disappears once the prism is below the critical aspect ratio.

Therefore, at the shorter square cylinder, it was observed that the flow from the upper free-end vertically runs toward the floor surface, and generates higher pressure fluctuation on the surface and makes the flow to the streamwise direction weaker in the wake.

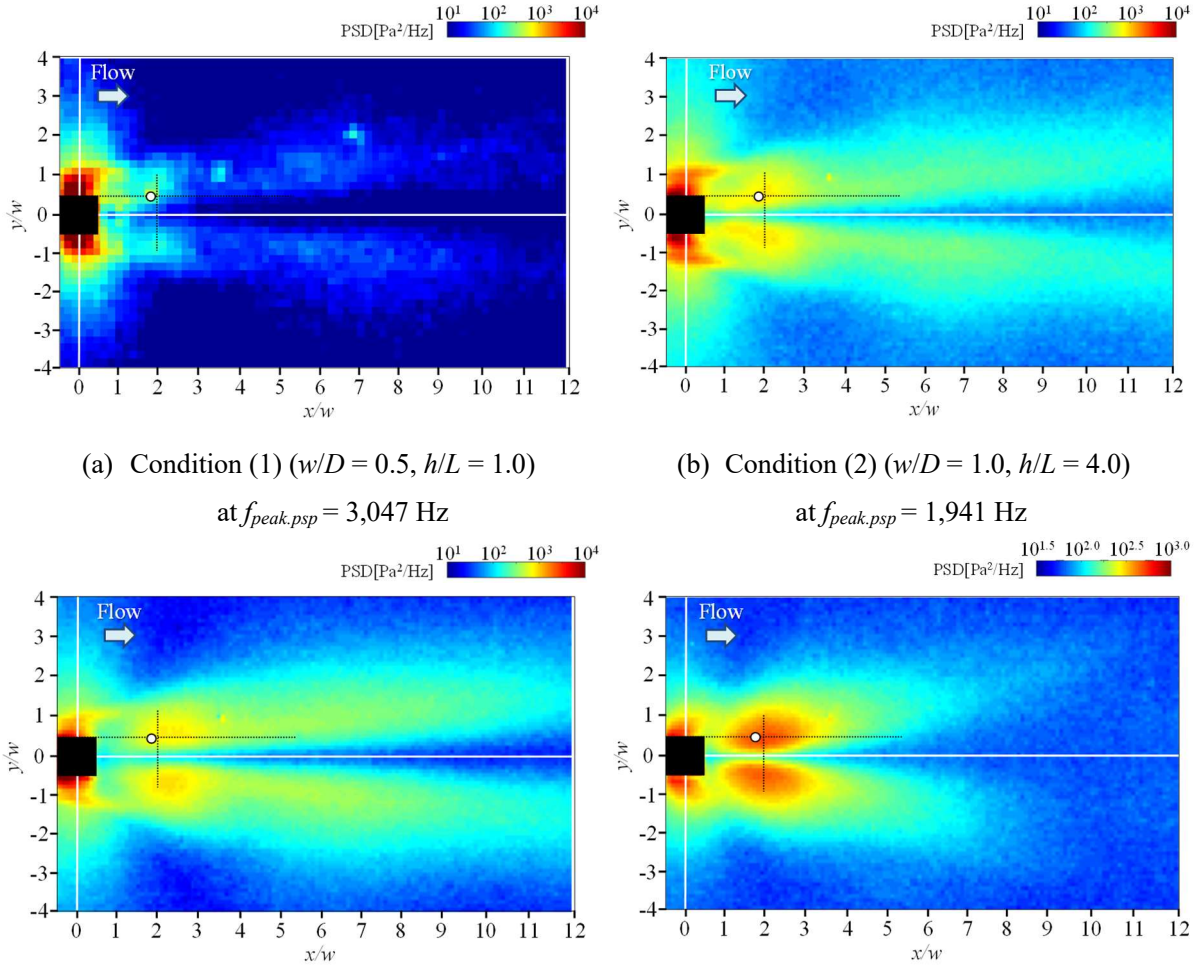

(a) Condition (1) (w/D = 0.5, h/L = 1.0) at $f_{peak.psp}$ = 3,047 Hz

(b) Condition (2) (w/D = 1.0, h/L = 4.0) at $f_{peak.psp}$ = 1,941 Hz

(c) Condition (3) (w/D = 1.0, h/L = 2.0) at $f_{peak.psp}$ = 1,859 Hz

(d) Condition (4) (w/D = 1.0, h/L = 1.0) at $f_{peak.psp}$ = 1,668 Hz

Figure 4.6 Measured pressure-fluctuation distribution at frequency of peak pressure fluctuation

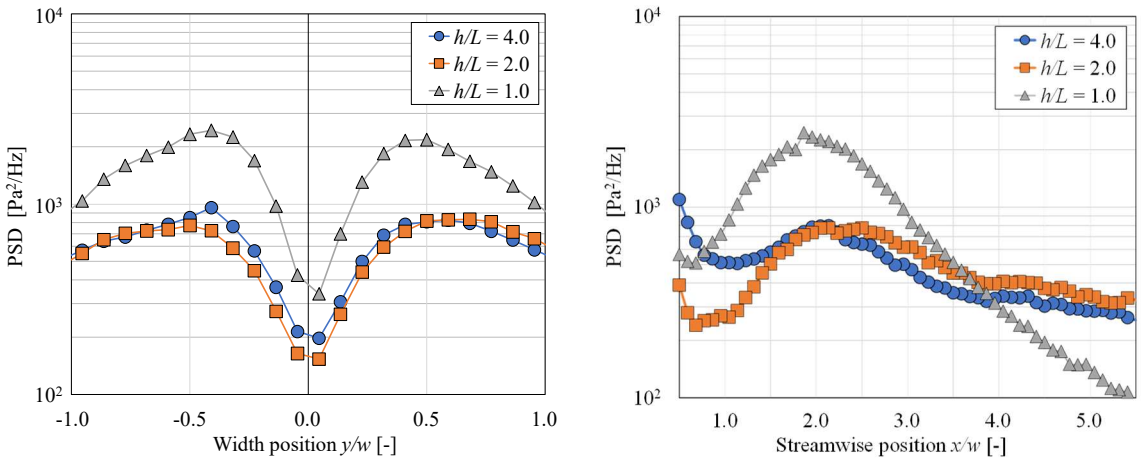

(a) At the streamwise position x/w = 2.0 (b) At the spanwise position y/w = 0.5

Figure 4.7 Measured pressure fluctuation profile at frequency of peak pressure fluctuation

4.3.2. Coherence and Phase between Pressure Fluctuations

4.3.2.1. Coherence

Coherence γ_{PSP}^2 based on the PSP data near the pressure tap, shown as a white dot in Figure 4.6, were calculated from the measured time-series pressure distribution. Coherence distributions at the peak frequency are shown in Figures 4.8. Coherences on each pixel at the streamwise position x/w = 1.8 and the spanwise position y/w = 1.0, which are shown as dashed lines in Fig. 4.8, are shown in Fig 4.9.

According to Figure 4.8, the high-coherence area was found to be spread from the sides of the cylinder to the downstream along the Kármán vortex shedding. Figure 4.10(a) shows that the coherence value near the pressure tap is almost unity and that in the opposite side of the centerline, that is around at y/w = -0.5, is 0.8 in all conditions. Compared with the square cylinders with the same width w (conditions (2)-(4)), the high-coherence area under the conditions (3) and (4) look same as the PSD distribution, but the spatial peak coherence is found to be at the downstream direction under the condition (2). Figure 4.9(b) presents that the peak of coherence values under the condition (2) are at the streamwise position x/w = 2.0 and 6.5. This suggests the vertical movement of the Kármán vortex shedding. The square cylinder can be presumed to be set in a thin turbulent boundary under condition (2) where the cylinder height h is sufficiently large for the boundary layer thickness δ. In the previous study, the square cylinder in a thin boundary layer, h/δ = 3.1 is found to have two pairs of counter-rotating streamwise vortices in the wake; one close to the obstacle free end and another close to the wall junction area (Bourgeois et al. 2011; Hosseini et al. 2013; Chen et al. 2022; Mohammadi et al. 2022). Therefore, it is possible that the same vortex formations are generated and may lead to generate the spatial peak coherence under the condition (2).

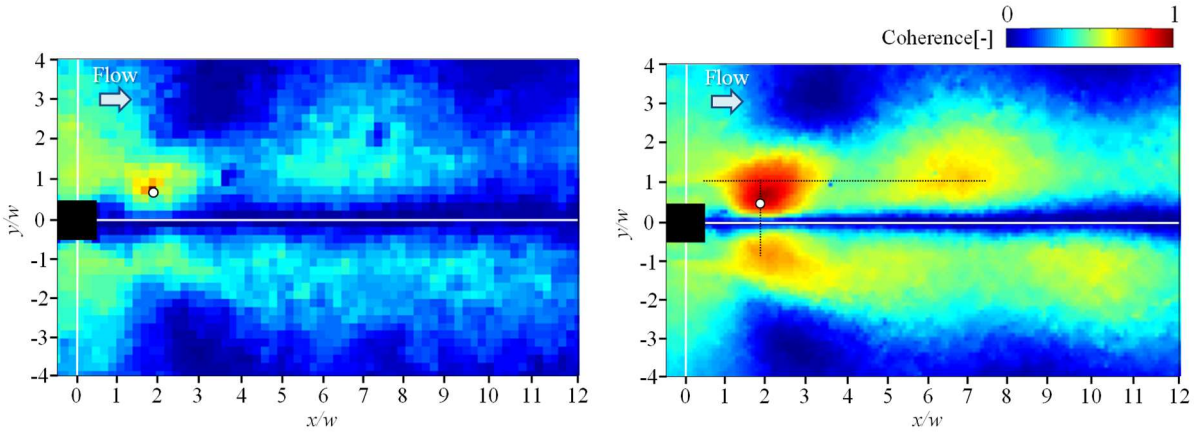

(a) Condition (1) (w/D = 0.5, h/L = 1.0) at $f_{peak.psp}$ = 3,047 Hz

(b) Condition (2) (w/D = 1.0, h/L = 4.0) at $f_{peak.psp}$ = 1,941 Hz

(c) Condition (3) (w/D = 1.0, h/L = 2.0) at $f_{peak.psp}$ = 1,859 Hz

(d) Condition (4) (w/D = 1.0, h/L = 1.0) at $f_{peak.psp}$ = 1,668 Hz

Figure 4.8 Coherence distribution at peak frequency based on PSP data obtained near the pressure tap

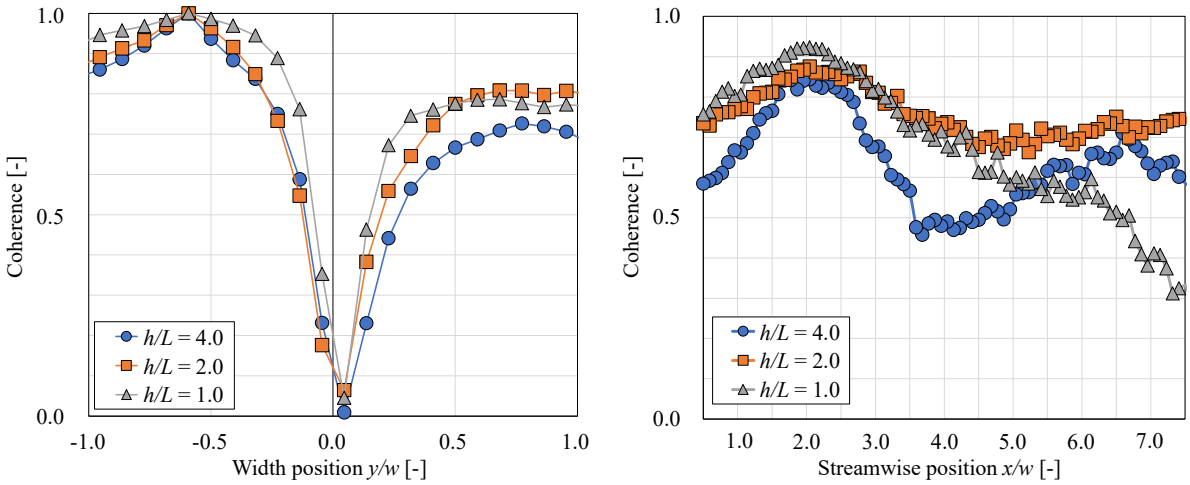

(a) At the streamwise position x/w = 1.8

(b) At and the spanwise position y/w = 1.0

Figure 4.9 Coherence on each pixel based on the PSP data obtained near the pressure tap

4.3.2.2. Phase shift

Phase shift ϕ_{PSP}, based on the PSP data near the pressure tap, shown as a white dot in Figure. 4.6, were calculated from the measured time-series pressure distribution. Phase-shift distributions at peak frequency are shown in Figures 4.10. Phase shift on each pixel at the spanwise position $y/w = 0.5$, which are shown as dashed lines in Fig. 4.10, are shown in Fig. 4.11.

Figure 4.10 presents that the phase distribution at peak sound frequency is almost the constant in all the conditions. The phase appears to be the uniform in the spanwise (y) direction ($-2 < y/w < 2$) and delayed into the downstream (x) direction. This result suggests that the Kármán vortex flow to the downstream. Figure 4.11 illustrates that the phase is delayed in the downstream direction under the conditions (2)-(4), and this delay is a little shorter at lower height.

Propagation speed of pressure fluctuation was estimated from the phase delay at peak frequency. One-period delay length under the conditions (1)-(4) was calculated by linear approximation of the phase delay from $x / w = 2.0$ in the downstream direction. The pressure fluctuation is assumed to be propagated in accordance with the wave equation given as follows (Kosaka et al. 2017):

$$\Psi(r,t) = A_0 e^{i\left(\frac{2\pi}{\lambda}r - 2\pi f_p t\right)} \tag{4.7}$$

The one-period delayed length of the pressure fluctuation was also assumed to equal to the propagating wavelength λ. Pressure-fluctuation propagation speed C was calculated from the peak frequency f_{peak} and the wavelength λ as follows:

$$\lambda = \frac{C}{f_{peak}} \tag{4.8}$$

where Ψ denotes a wave function, and A_0 denotes an amplitude of the wave.

Estimated propagating velocities of pressure fluctuation at each wind velocity are listed in Table 4.5. When C is nondimensionalized with each freestream wind velocity U, the Kármán vortex was revealed to propagate at approximately 85 % of the velocity normalized by the freestream wind velocity U.

Table 4.5 Propagating velocity of pressure fluctuation

Cylinder	(1)	(2)	(3)	(4)
Cylinder width w/D [-]	0.5	1.0	1.0	1.0
Cylinder height h/L [-]	1.0	4.0	2.0	1.0
Wind velocity U [m/s]	100	116.7	116.7	116.7
Phase delay [/pixel]	0.257	0.141	0.141	0.128
Wavelength of propagation λ [mm]	28.9	52.6	52.6	57.8
Peak sound frequency $f_{mes,p}$ [Hz]	3,047	1,941	1,859	1,695
Propagating velocity of pressure fluctuation C [m/s]	88.0	102.1	97.8	98.0
Dimensionless velocity C/U [-]	0.88	0.87	0.84	0.84

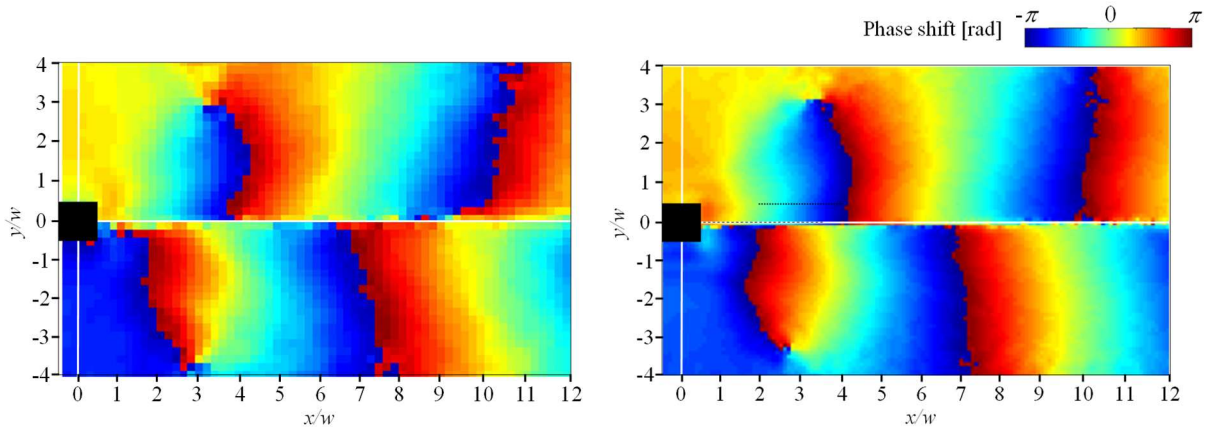

(a) Condition (1) (w/D = 0.5, h/L = 1.0) at $f_{peak.psp}$ = 3,047 Hz

(b) Condition (2) (w/D = 1.0, h/L = 4.0) at $f_{peak.psp}$ = 1,941 Hz

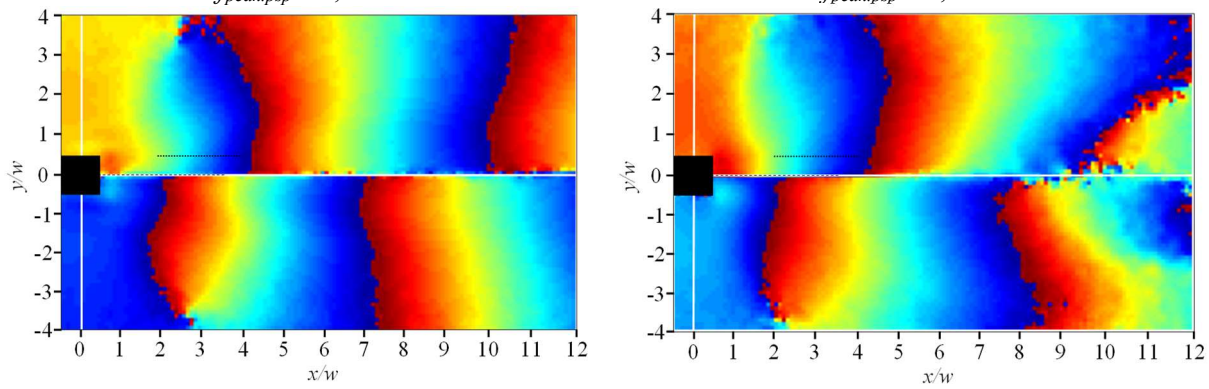

(c) Condition (3) (w/D = 1.0, h/L = 2.0) at $f_{peak.psp}$ = 1,859 Hz

(d) Condition (4) (w/D = 1.0, h/L = 1.0) at $f_{peak.psp}$ = 1,668 Hz

Figure 4.10 Phase-shift distribution at peak frequency based on the PSP data obtained near the pressure tap

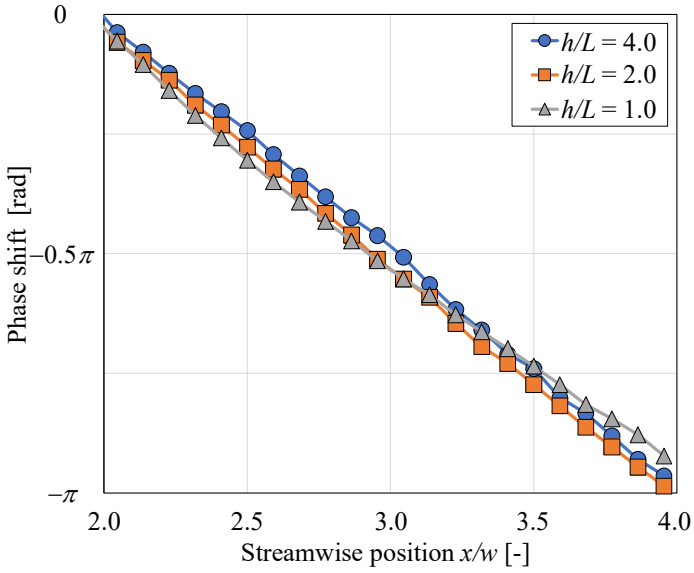

Figure 4.11 Phase-shift of the cylinder width $w = D$ on each pixel based on the PSP data obtained near the pressure tap at and the spanwise position y/w = 0.5

4.3.3. SVD Analysis

Figure 4.12 shows the PSD values of the right-side singular vector $\mathbf{v_i}$ within the frequency tolerance band $f_{peak,\mathrm{PSP}} \pm 2\Delta f$ of each mode. Figure 4.13 shows the contours of the two modes, which have the highest PSD values within the frequency tolerance band $f_{peak,\mathrm{PSP}} \pm 2\Delta f$.

Figure 4.12 presents that some modes have the peak PSD values within the frequency tolerance band $f_{peak,\mathrm{PSP}} \pm 2\Delta f$ in all conditions. The modes with the more peak PSD than 3 were extracted. Figure 4.13 shows that the high and low value areas repeat to the downstream behind the square cylinder along the Kármán vortex shedding. The contours of both two modes are observed to be axisymmetric with the respect to the centerline of the model at the downstream direction under the conditions (1) and (4). Both positive and negative similar values are observed to be at each side of the centerline, $y/w = 0$, at the same streamwise position. On the other hand, a contour of one mode was observed as asymmetric under the conditions (2) and (3). Figure 4.13 (B)(a) and (C)(b) illustrate that the values around at the streamwise position x/w = 1-1.5 and the spanwise position y/w = -0.5 is higher than that at the opposite side y/w = 0.5, and the area and positions of the peak values are found to be different at each side of the centerline at the same streamwise position. This asymmetric distribution is thought to be caused by the change of the flow structure in the wake due to the taller square cylinder. The flow from the sides of the square cylinder becomes dominant as the square cylinder becomes taller, which may lead to generation of the asymmetric complex vortical structure in the wake.

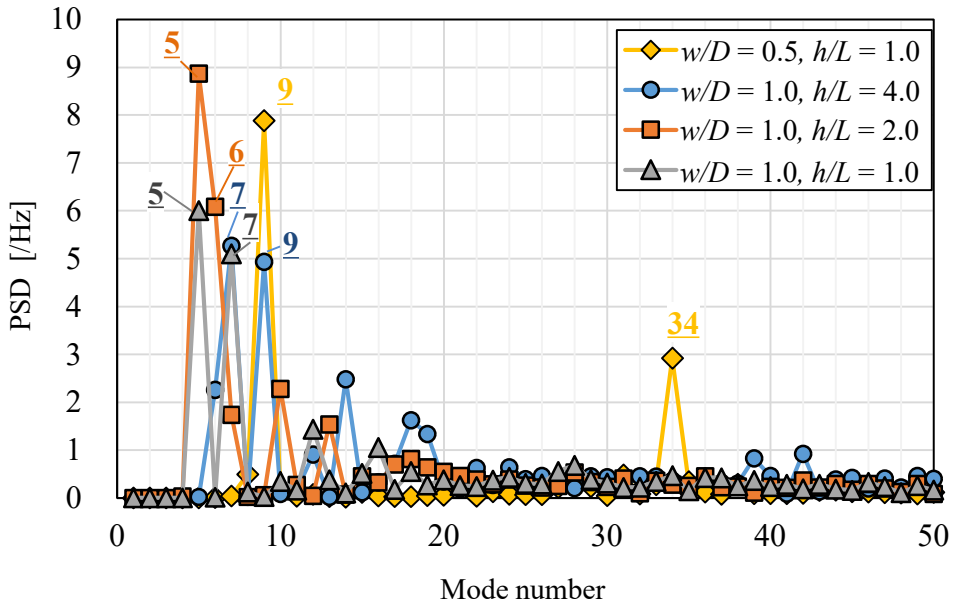

Figure 4.12 PSD values of the right-side singular vector $\mathbf{v_i}$ within the frequency tolerance band. The numbers written with plots are the extracted mode for Fig 4.13.

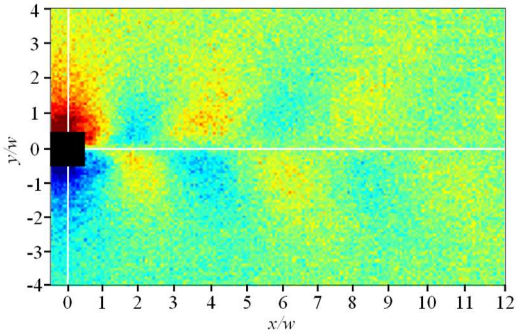

(a) Mode 9

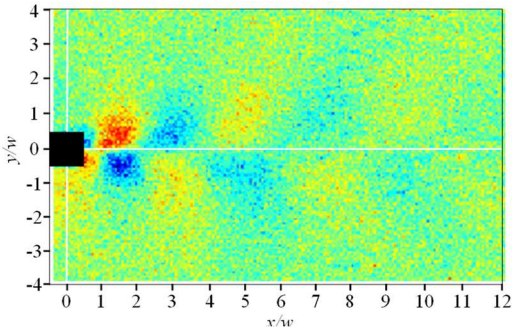

(b) Mode 34

(A) Condition (1) (w/D = 0.5, h/L = 1.0)

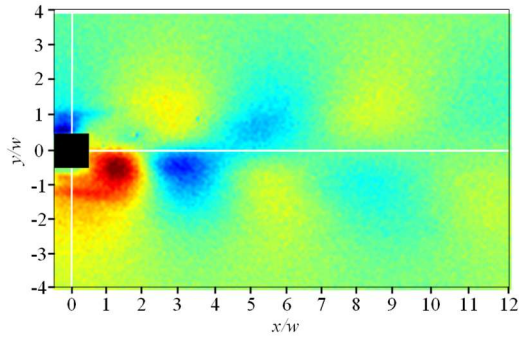

(a) Mode 7

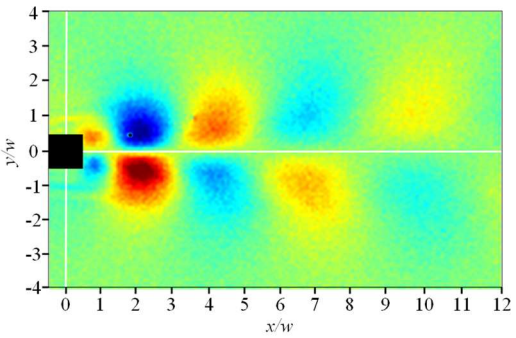

(b) Mode 9

(B) Condition (2) (w/D = 1.0, h/L = 4.0)

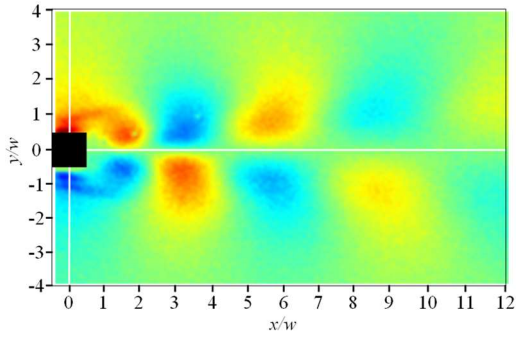

(a) Mode 5

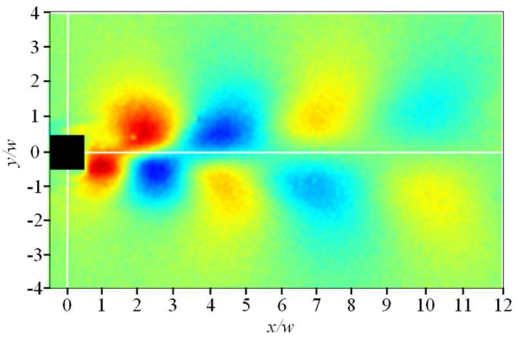

(b) Mode 6

(C) Condition (3) (w/D = 1.0, h/L = 2.0)

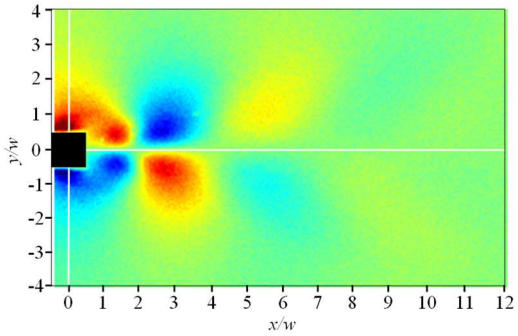

(c) Wind velocity U = 100 m/s

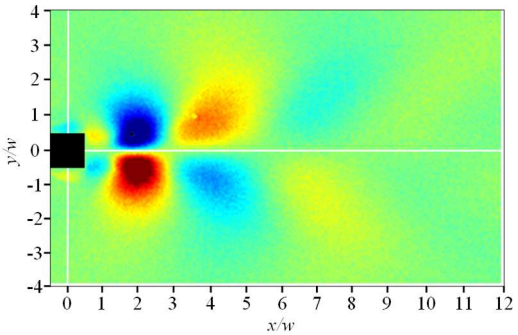

(d) Wind velocity U = 116.7 m/s

(a) Mode 5

(b) Mode 7

(D) Condition (4) (w/D = 1.0, h/L = 1.0)

Figure 4.13 Contours of two modes with the highest PSD values within the frequency tolerance band $f_{peak,\mathrm{PSP}} \pm 2\Delta f$.

4.4. Conclusion

The pressure fluctuations distribution on the floor surface behind a square cylinder in the turbulent boundary layer was measured by PSP and its accuracy and frequency response at the Mach number around $M = 0.3$ were examined, where aerodynamic noise is mainly generated from the surface pressure fluctuations. Four types of the square cylinders were examined in the same turbulent boundary layer for detailed comprehension of the relationship between these conditions and the Kármán vortex shedding structure. In this study, the following conclusions are made:

- The measured values by PSP have a similar tendency to that of the pressure transducer up to 5 kHz. The peak PSD of pressure fluctuations generated by the Kármán vortex shedding from the square cylinder can be observed within an error of approximately 30 % up to greater than 3 kHz.
- The peak frequency of the Kármán vortex shedding is found to become lower with the shorter square cylinder similar to the previous empirical equation of the Strouhal number.
- The peak PSD value of the shortest square cylinder ($w/D = 1.0$, $h/L = 1.0$) is twice higher than the other conditions and its high-pressure fluctuation area is not to be spread into the downstream, which suggests the flow from the upper end of the cylinder to become dominant in the wake rather than that from the square cylinder side.
- The spatial peak coherence distribution is observed behind the tallest square cylinder ($w/D = 1.0$, $h/L = 14$), which suggests the vertical movement of the Kármán vortex shedding. The Kármán vortex is revealed to propagate at approximately 85 % of velocity normalized by the freestream wind velocity U from the phase shift distribution.
- One contour of the two main modes extracted as the highest PSD of the right-side singular vector $\mathbf{v_i}$ at the Kármán vortex frequency have asymmetric distribution behind the taller square cylinder ($w/D = 1.0$, $h/L \geq 7.0$), which suggests that the flow from the square cylinder side becomes dominant.

Chapter 5
Sound-source Distribution in the Bogie Section of a Train Determined by Simultaneous Measurement by Pressure-sensitive Paint and a Microphone

List of symbols

A Stern–Volmer coefficient [-]

A_0 Wave amplitude [-]

B Stern–Volmer coefficient [-]

C Pressure-fluctuation propagation speed [m/s]

C_{XY} Cross-correlation function [-]

D_w Bogie wheel diameter [mm]

Fi Force for fluid [N]

H Wind tunnel height [mm]

H_b Bottom bogie surface height set position [mm]

H_c Bogie cavity height [mm]

I Luminescent intensity [-]

L Wind tunnel length [mm]

L_b Bogie bottom surface length [mm]

L_c Bogie cavity length [mm]

L_f Bogie side frame length [mm]

L_u Length from the upstream cavity edge and the upstream edge of the bottom bogie surface [mm]

M Mach number (= U/a) [-]

N_{FFT} FFT sampling data [-]

P Pressure [Pa]

P_{XX} Power spectrum [Pa^2]

$S_{y,bs}$ Bogie bottom surface [m^2]

St Strouhal number [-]

T Temperature [K]

U Freestream velocity [m/s]

U_c Vortex convection velocity [m/s]

W Wind tunnel width [mm]

W_b Bogie bottom surface width [mm]

W_c Bogie cavity width [mm]

W_f Bogie side frame width [mm]

W_w Bogie wheel width [mm]

X Frequency spectrum [-]

Y Frequency spectrum [-]

a Sound velocity [m/s]

f_p Sound peak frequency [Hz]

f_s Capture frequency [Hz]

Δf Frequency resolution [Hz]

k Discrete frequency [Hz]

m Vibration mode of free shear layer [-]

p Sound pressure [Pa]

p_{bs} Pressure in vertical direction on the surface [Pa]

p_d Far-field sound pressure [Pa]

$p_{d,bs}$ Far-field sound pressure from the bogie bottom surface [Pa]

p_i Local surface pressure [Pa]

p_s Surface pressure [Pa]

p_0 Reference sound pressure (= 20 μPa) [Pa]

r Distance between a noise source and a measurement point [m]

s Captured area per pixel [m^2/pixel]

x Streamwise position [m]

y Width position [m]

Ψ Wave function [-]

δ Boundary layer thickness [mm]

κ Dimensionless vortex convection velocity [-]

λ Propagating wavelength [m]

γ Phase-correction constant [-]

γ_{XY}^2 Coherence [-]

ϕ_{XY}^2 Phase shift [rad]

θ Boundary layer momentum thickness [mm]

Subscript

ref Reference condition

mes Measured value

theo Theoretical value

Abbreviation

COP Coherent Output Power

DMD Dynamic Mode Decomposition

FFT Fast Fourier Transform

POD Proper Orthogonal Decomposition

PSD Power Spectral Density Function

PSP Pressure Sensitive Paint

SNR Signal-to-Noise Ratio

SPL Sound Pressure Level

SVD Single-Value Decomposition

5.1. Introduction

It is a worldwide trend that intercity trains are becoming faster, and noise intensity increases as the running speed of such trains increases. Therefore, it is necessary to reduce aerodynamic noise for maintaining a quiet environment around the railway. Detailed knowledge of the properties of a sound source and the sound distribution is required for the reduction in aerodynamic noise.

The Lighthill-Curle equations (Lighthill 1952; Curle 1955) show that a sound source of aerodynamic noise is changed from a dipole sound source into a quadrupole sound source depending on the Mach number M (= U/a), which is the ratio between the freestream velocity U and the sound velocity a. In case of high-speed trains, of which the Mach number is approximately M = 0.3, aerodynamic noise is mainly generated as a dipole sound source from pressure fluctuations on a surface (Iida et al. 2000). Therefore, it is important to measure distributions of surface-pressure fluctuation on a test model for the assessment and the detection of aerodynamic noise sources. Conventionally, pressure fluctuations are measured by using pressure sensors set in orifices on a surface of a test model. This measurement technique is highly accurate and reliable. However, it is difficult to be applied to a curved surface, and to acquire the pressure distribution across a whole surface, multiple sensors and/or repeated measurements are necessary.

Recently, as an alternative technique for measuring surface-pressure fluctuations to that using pressure sensors (with the problems described above), a technique using a pressure-sensitive paint (PSP) has been developed (Bell et al. 2001; Liu at al. 2005; Asai and Yorita 2011; Gregory et al. 2014; Peng and Liu 2020; Liu et al.,2021). The PSP measurement allows us to estimate time-series surface-pressure distributions by measuring the varying intensity of the luminescent light from the dye in PSP excited by an excitation light. The surface-pressure distributions are measured by capturing this luminescence by using a camera, and a two-dimensional (2D) surface-pressure distribution with higher spatial resolution than that possible by using point measurement with a conventional pressure sensor can be obtained.

Measurements by PSP have mostly been applied to transonic and supersonic flows (Nakakita et al. 2012; Sugioka et al. 2015). In recent years, however, PSP has been applied to unsteady phenomena in the low-speed region (Liu 2003; Asai and Yorita 2011; Nakakita 2011; Peng et al. 2016). Applying PSP to unsteady phenomena in the low-speed range faces two major problems: time response of PSP and low signal-to-noise ratio (SNR) due to low dynamic pressure. Regarding the former problem, unsteady PSP has been developed, and PSPs with quick response time, which can adequately follow pressure fluctuation in the order of kilohertz, have been demonstrated. The time response of PSP is governed by the diffusion process through the binder. Therefore, a fast-responding PSP with a highly diffusive porous binder should be employed for the measurement of time-resolved pressure distributions. One of the most common binders for a sprayable fast-responding PSP is a polymer/ceramic binder composed of a polymer matrix and small ceramic particles. In particular, the polymer/ceramic PSP (PC-PSP) developed by Scroggin et al. (1999) and modified by Gregory et al. (2001) has been widely used in wind-tunnel testing. Klein et al. (2008) developed an original PC-PSP, the response time of which was approximately 1 ms. Kitashima et al. (2014) developed a PC-PSP composed of a fluoric polymer and titanium dioxide (TiO_2) particles with a kilohertz-order time response by controlling particle size, particle content, and a dye application method. Peng et al. (2018) developed a new formulation of fast PSP using mesoporous, hollow SiO_2 particles as

luminophore hosts to provide additional paths for oxygen diffusion. This mesoporous-particle-based PSP (MP-PSP) featured both fast response (about 100 μs) and high durability with a uniform luminophore distribution throughout the binder. The response time was found to be reduced to 5 μs or less for a paint with a similar formulation using a luminophore with shorter luminescence lifetime (Egami et al., 2019). Sugioka et al. (2018) developed a PC-PSP with reduced surface roughness (~ 0.5 μm) for measurements in transonic flows by comparing the PSP's properties (such as particle size, mass content and solvent). This PSP leads that the unsteady pressure distribution can be measured without affecting the flow field on the model (Sugioka et al., 2018a, 2018b; Uchida et al., 2021). A PC-PSP based on polymer particles which prevent it from losing its luminescent intensity was proposed (Matsuda et al. 2016).

Regarding the low signal-to-noise ratio (SNR) due to low dynamic pressure, several methods for improving SNR of PSP have been developed. A simple one is a phase-lock measurement that accumulates synchronized snapshots with a reference signal out of the targeted periodic phenomenon (McGraw et al. 2006; Gregory et al. 2007). Advanced data-processing methods including single-value decomposition (SVD) and proper orthogonal decomposition (POD) can be directly applied to the PSP image sequence, generating a set of modes representing distinctive features in the time-resolved data. For applications at low-speed region, the high level of noise demands more rigorous criteria for mode selection, which was achieved by examining the spatial contour and frequency spectrum of each mode (Pastuhoff et al. 2013; Peng et al. 2016). The mode selection method based on compressed data fusion, which incorporated the clean data from scattered microphones, was proposed to optimize the reconstruction of POD modes (Wen, et al., 2018). In addition, dynamic mode decomposition (DMD) has also found applications in analysing unsteady PSP data, which was less susceptible to noise contamination and more effective in extracting pressure features than POD (Ali, et al. 2016; Gößling et al. 2020). For a precise measurement of pressure fluctuation level in aerodynamic application, the frequency-domain method based on fast Fourier transform (FFT) is usually applied. FFT was applied to PSP images (Nakakita, 2011), and subtracting power spectral density (PSD) of the wind-off images from that of the wind-on images is shown to be an effective way to reduce the noise component (Nakakita, 2013). Advanced techniques for spectral analysis which extract other unsteady information in addition to the power spectrum, such as coherence and phase, were also developed. Recently, the spectrum estimation technique using cross-corelation was also devised and the noise floor was further reduced while it requires a lot of samples (Ozawa at al. 2019). Meanwhile, coherent output power (COP), which is given by a cross correlation between time-series pressure measured by PSP and a reference signal, was employed for the measurement of pressure fluctuations associated with tonal trailing-edge noise for a two-dimensional NACA 0012 airfoil (Noda et al. 2018). Accuracy of an unsteady PSP measurement in the low-speed region has thus been improved.

Hence, the PSP measurement has been applied to acoustic applications. The pressure on the wall of the rectangular cavity excited by a single-frequency sound source was measured for evaluating the capabilities of PSP for acoustics measurements (Gregory et al. 2006; Disotell et al. 2011Tthe pressure amplitudes of 125.4 dB SPL (52.7 Pa) was found to be resolved using phase averaging. Moreover, the minimal detectable pressure level limit of 5 Pa (108 dB) of the same rectangular cavity was observed by using the DMD and FFT data reduction (Gößling et al. 2020). Fast PSP measurements were performed

and discrete tonal noises in high-speed inclined jet impingement scenarios were clarified (Liu et al., 2022, 2022a). These measurements demonstrated the wave propagation along the wall surface and revealed vortices with different size were induced by instability of shear-layer, which travelled downstream and interacted with the flat plate. In addition, the sound pressure measurements of tonal sound fields in a circular duct were measured with PSP and microphone arrays for assessment of the applicability of PSP in turbomachinery acoustics applications, which indicated the maximum detected deviation in the pressure measurement of PSP was found to be 30 Pa (Gößling et al. 2023). However, there are still few examples of applying a PSP measurement to a complex shape for evaluation of a sound-source distribution and for comprehension of an unsteady phenomenon in the low-speed region.

In this study, the sound level emitted from a bogie section of a railway vehicle, that includes a bogie and a lower section of the train around it, was measured. In the previous study (Kitagawa et al. 2013; Yamazaki et al. 2019), the sound radiated from a bogie section was shown to be one of the dominant sound sources in the case of a Shinkansen ("bullet train") running at a speed above 83.3 m/s and generated from the wind blowing directly onto the bogie and its cavity structure. The sound level from a 1/8-reduced-scale simplified model and pressure-fluctuation distribution of the bottom surface of the bogie were measured simultaneously by a microphone and PSP, and the sound-source distribution from the bogie section was discussed. The peak sound source distribution was detected by comparing the results of frequency analysis and calculating the coherence between the surface pressure measured by PSP and the measured sound pressure. The vortex convection velocity was estimated from the phase distribution of the pressure fluctuation at the peak frequency. The sound level at the bottom surface of the bogie was estimated from the COP data, which was calculated from the pressure data measured by PSP with the measured sound pressure, by using the Lighthill-Curle equation, and the contribution of the sound radiated from the bottom surface of the bogie was evaluated.

5.2. Experimental Apparatus

5.2.1. Unsteady pressure-sensitive paint (PSP)

Pressure-sensitive paint is a pressure sensor utilizing a photochemical reaction that involves luminescent molecules (luminophores) and binder (mainly polymer). The luminophores emit luminescence when illuminated by excitation light with an appropriate wavelength. Since the intensity of emitted light from the luminophores depends on the partial pressure of oxygen, the air pressure over the PSP can be calculated from the luminescent intensity captured by a camera. A ceramic PSP combined with a quick-response polymer is used in this study (Kitashima et al. 2014; Ozawa et al. 2019; Pandey and Gregory 2015; Sakaue et al. 2011; Scroggin et al. 1999; Sugioka et al. 2018, 2018a, 2018b, 2019; Uchida et al. 2021). Pressure sensitivity of the PSP (measured by static calibration) was 0.77 %/kPa. Moreover, according to frequency-response measurements using an acoustic resonance tube (Sugimoto et al. 2017), frequency response of approximately 4,400 Hz was guaranteed. In the present study, a frequency analysis is restricted to a maximum of 4.4 kHz. This cutoff frequency is six times higher than the peak frequency of the sound radiated from the test model used in this study.

5.2.2. Experimental Model and Measurement System

Sound-pressure level emitted from a 1/8-reduced-scale simplified train model and pressure-fluctuation distribution of its lower surface of the bogie were experimentally evaluated in a low-noise high-speed wind tunnel (Hitachi 2014; Matsui et al. 2017, 2020). The test section of the wind tunnel has the dimensions of 600 mm (W) × 400 mm (H) × 2,000 mm (L), and maximum freestream velocity is 116.7 m/s. In this study, wind velocity was set to be U = 55.6, 69.4, 83.3, 100, and 116.7 m/s.

A 1/8-reduced-scale train model, which simulates the lower part of the train around a bogie, was employed. Photographs and images of the test model are shown in Fig. 5.1. The test model consists of a simplified bogie in a cavity, with length L_c = 500 mm, width W_c = 374 mm, and depth H_c = 100 mm. The bogie is set at the center of the cavity. As the measurement area, the bottom surface of the bogie, which is I-shaped as shown in Figs. 5.1(a) and (c), was painted by PSP because this area is considered to become one of the main sound sources by wind blowing directly onto it. The bottom surface of the bogie,which has width $W_b = 0.75W_c$ and length $L_b = 0.27L_c$ along its center line, was set at the distance $H_b = 0.85H_c$ from the carbody. The bogie has the side frame with width $W_f = 0.088W_c$ and length $L_f = 0.84L_c$, and four wheels with width $W_w = 0.045W_c$ and diameter $D_w = 0.22L_c$. The length from the upstream edge of the cavity and the upstream edge of the bottom surface of the bogie is $L_u = 0.36L_c$. The train model was inverted vertically and set without rails and on the ground. This configuration makes it easy to capture images of the PSP and to directly measure the noise radiated from the model. The train model was fixed so that its upper level could be aligned with the bottom of the wind-tunnel nozzle. It has 18-degree slopes on the upstream and downstream sides of the cavity. This configuration eliminates the velocity defect near a ground, which is generated by the development of a boundary layer in the nozzle, on the upstream side, so it suppresses the noise from separation of the freestream at the downstream edge. Velocity measurements by a hot-wire anemometer (Kanomax, Model 7000Ser) and an I-shaped probe show that the boundary-layer thickness δ and momentum thickness θ on the upstream side 70 mm from the upstream cavity edge were δ = 25 mm and θ = 2.1 mm, respectively.

The PSP measurement system shown in Figs. 5.1(d) and (e) is explained as follows. Three ultraviolet (UV)-light emitting diodes (LEDs) (IL-106, HARDsoft) were used with a condenser lens (HSO-PL-180-UV, HARDsoft) as an excitation light source for the PSP. The LEDs were set at 650 mm horizontal side from the center of the bogie. A high-speed camera (V2012, Phantom) was used as a light-emission detector. The camera was fitted with a 50-mm-focal-length lens (Nikkor 85 mm f 1.4, Nikon) and a 590-nm long pass filter (9022621, Laser create Corp.). Images were captured at 16 kps with 1,280 × 720 pixels. Spatial resolutions were 0.33 and 0.43 mm/pixel in the streamwise (*y)* and width (*x)* directions, respectively, at the center of the surface of the bogie bottom. The number of images recorded during each run was 27,641.

Unsteady surface pressure was measured using a Kulite pressure transducer (XCQ-062-5SG), which was flush-mounted on the bottom plate of the bogie. The pressure tap connected to the Kulite sensor was set at the distance $0.2L_b$ from the upstream edge of the bottom surface of the bogie in the streamwise direction, as depicted in Fig. 5.1(c). The cutoff frequency of the response of the Kulite sensor was 150 kHz, which is significantly higher than that of the unsteady PSP. Sound radiated from the test model was

measured by a microphone (DC53A, Rion) and a sound-level meter (NL-14, Rion). The microphone was set at height of 1 m from the upstream edge of the cavity in the center of wind tunnel for direct measurement of the far-field sound pressure radiated from the bogie cavity including the bogie. The data from the pressure transducer and sound-level meter was recorded with a data recorder (LX-100 Series, TEAC) at 16 kHz (which is as high as the frame rate of the camera). The high-speed camera, pressure transducer, and sound-level meter measurements were synchronized by a trigger signal produced by the start of camera recording.

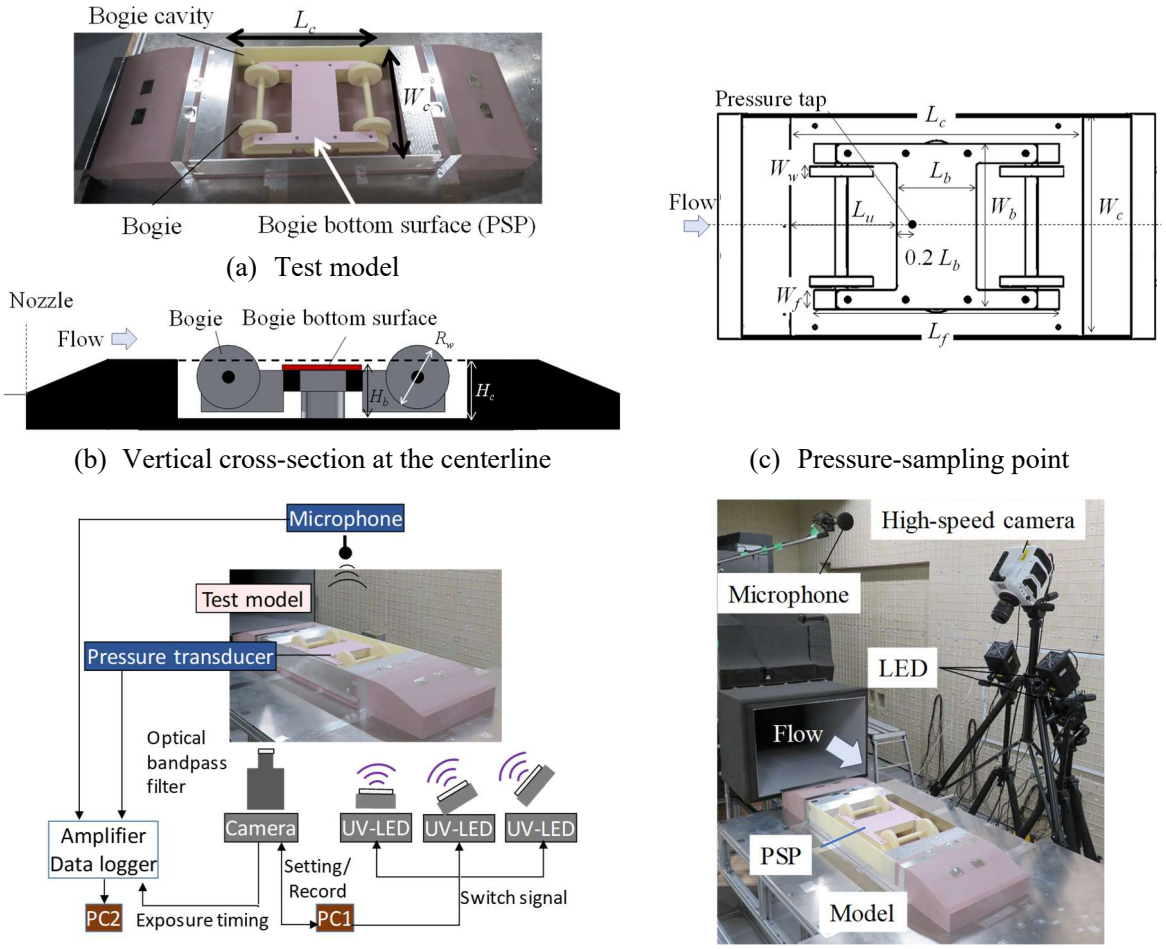

(a) Test model

(b) Vertical cross-section at the centerline

(c) Pressure-sampling point

(d) Diagram of measurement system

(e) Setup of measurement system

Figure 5.1 Experimental model and measurement system

5.2.3. Data Analysis

5.2.3.1. Pressure-intensity relation

The time-series pressure distribution was calculated from the captured PSP images by using the Stern–Volmer equation, defined as

$$\frac{I_{\mathrm{ref}}}{I} = A(T) + B(T)\frac{P}{P_{\mathrm{ref}}} \tag{5.1}$$

where I is luminescent intensity, P is pressure, and the subscript "ref" stands for reference conditions at which P and I are known. $A(T)$ and $B(T)$ are the Stern–Volmer coefficients, which depend on temperature. In this study, the images obtained by averaging the wind-on images and subtracting the dark images, which were captured without the excitation light, were used as the intensity of the reference image, I_{ref}, as applied in the previous studies (Nakakita, 2013; Crafton et al.., 2017; Sugioka et al., 2019). This method makes it possible to reduce the influence of the change in luminescent intensity due to the temperature change or photo-degradation of the luminophores, though only the pressure fluctuations could be calculated. In this study, pressure was calculated using the averaged luminance value of 4×4 pixels area as a calculating single pixel for reducing the noise level as the spatial binning. The PSP images with 320 × 180 calculating pixels after spatial averaging over a 4×4 pixels area were analyzed for pressure fluctuation calculation.

5.2.3.2. Power distribution

Figure 5.2 shows the overall flow of PSP data-analysis process. After spatial binning of the time-series pressure distribution, PSD of the pressure fluctuations was calculated from the time-series pressure distribution by using an ensemble averaging FFT, as proposed by Nakakita (2011, 2013). In this method, images corresponding to an entire time-series data set are split into a smaller number of segmented data sets, containing 2^N images per sets. The FFT processing was applied to time-series pressure data of N_{FFT} (=2^N×2) images obtained by combining two adjacent data sets. At this time, the data set was selected so as to overlap 2^N images at a time. The split data sets were overlapped with neighboring data sets. The frequency resolution was determined as follows:

$$\Delta f = \frac{f_s}{N_{FFT}} \tag{5.2}$$

The power spectrum, $P_{XX}(f)$, which was calculated by using the frequency spectrum, $X(f)$, and its complex conjugate, $X^*(f)$, obtained by FFT, was ensemble averaged, and PSD was calculated as follows:

$$PSD(f) = \frac{\langle P_{XX}(f)\rangle}{\Delta f} = \frac{\langle X(f)X^*(f)\rangle}{\Delta f} = \frac{\langle X(f)X^*(f)\rangle}{f_s/N_{FFT}} \tag{5.3}$$

$$\langle X(f)X^*(f)\rangle = \frac{1}{R}\sum_{r=1}^{R} X(f)X^*(f) \tag{5.4}$$

Where the operator < > denotes the ensemble average, r is the r th data set and R (=10) is the average times.The Hanning window was used as a window function in the FFT analysis, and the power attenuation by the window function was corrected. In this analysis, the background spectrum subtraction obtained by wind-off images (Nakakita 2013) was not adopted because the background spectrum was not constant at each calculating pixel area with each measurement case. The sampling data (N_{FFT}) was sampled at 4,096 points and averaged 10 times. Δf was 3.9 Hz. The FFT processing conditions of the pressure transducer

and the sound-level meter were set to be the same as the PSP under all the test conditions.

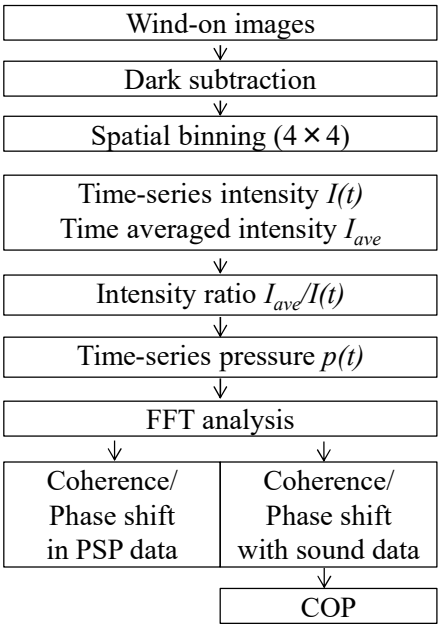

Figure 5.2 Flow chart of processing of PSP data

5.2.3.3. Coherence and phase shift

Coherence represents degree of the correspondence between signals *x* and *y,* and phase shift represents the difference between the phases of the two signals (Bendat and Piersol 1980; Marple 1987). Coherence, $\gamma_{XY}^2(f)$, and phase shift, $\phi_{XY}(f)$, are defined as follows:

$$\gamma_{XY}^2(f) = \frac{|\langle C_{XY}(f)\rangle|^2}{\langle P_{XX}(f)\rangle\langle P_{YY}(f)\rangle} = \frac{|\langle X^*(f)Y(f)\rangle|^2}{\langle X(f)X^*(f)\rangle\langle Y(f)Y^*(f)\rangle} \tag{5.5}$$

$$\phi_{XY}(f) = \tan^{-1}\left(\frac{Q_{XY}(f)}{K_{XY}(f)}\right) = \tan^{-1}\left(\frac{\mathrm{Im}(C_{XY}(f))}{\mathrm{Re}(C_{XY}(f))}\right) \tag{5.6}$$

where $\langle C_{XY}(f)\rangle$ is the ensemble-averaged cross-correlation function.

The cross-correlation function $C_{XY}(f)$, which is calculated using the frequency spectra, $X(f)$ and $Y(f)$, of the two signals *x* and *y,* was ensemble averaged in this calculation. The pressure dataset captured by the PSP was separated into as an *x* signal, and two other datasets, the PSP data around the pressure taps and the data measured by a microphone, were used as a *y* signal.

5.2.3.4. Coherent output power

The degree to which the frequency response of signal *x* contributes to signal *y* could be represented by COP (Bendat and Piersol 1980; Goldman 1999; Noda et al. 2018). It is defined as the power spectrum at each frequency component *X*(*k*) multiplied by squared coherence γ_{XY}^2 between spectra *X*(*k*) and *Y*(*k*). The data measured by a microphone was used as the *y* signal, and the pressure data captured by PSP were

used as an output power. The COP was calculated at each calculating pixel. By using COP, it is possible to determine the contribution of the pressure fluctuation on a surface to the detected sound as follows:

$$\mathrm{COP}(f) = \langle P_{XX}(f) \rangle * \gamma_{XY}^2(f) \tag{5.7}$$

where $\langle P_{XX}(f) \rangle$ is the ensemble-averaged power spectrum.

5.2.3.5. Estimation of sound power

The sound level from the bottom surface of the bogie was estimated by using the Curle equation. According to which, aerodynamic noise in a low-Mach-number region is dominantly generated from the pressure fluctuations on the surface acting as a dipole sound source. The Lighthill-Curle equation gives the far-field sound pressure $p_d(\boldsymbol{x},t)$ radiated from the test model (Phillips, 1956; Iida, et al., 2000, Larsson, et al., 2004) as follows:

$$p_d(\boldsymbol{x},t) \sim \frac{x_i}{4\pi a|\boldsymbol{x}|^2}\frac{\partial}{\partial t}\boldsymbol{F_i}\left(t-\frac{|\boldsymbol{x}|}{a}\right) = \frac{x_i}{4\pi a|\boldsymbol{x}|^2}\int_S \frac{\partial}{\partial t}p_s(\boldsymbol{y}, t-\frac{|\boldsymbol{x}|}{a})n_i dS_j \tag{5.8}$$

where $\boldsymbol{x}$ denotes a measurement point position, $\boldsymbol{y}$ denotes a point in a surface S_j, a is the sound speed and $\boldsymbol{F_i}$ is the total force with which the whole surface acts upon the fluid. The force for fluid $\boldsymbol{F_i}$ can be calculated from the integral of the multiplication of the surface pressure, $\underline{p_s}$, and the unit normal vector of the surface, n_i. In this study, the wavelength of peak sound was larger than the size of the bogie, and thus, the effect of retard time can be disregarded. Hence, the mean square of the far-field sound pressure from the bogie bottom surface, $\overline{{p_{d,bs}}^2(f)}$, can be estimated from the pressure in vertical direction on the surface, p_{bs} as follows:

$$\overline{{p_{d,bs}}^2(f)} \sim \frac{1}{16\pi^2 a^2 r^4}\overline{\frac{\partial}{\partial t}\boldsymbol{F_i}(f)^2}$$

$$\sim \frac{1}{16\pi^2 a^2 r^4}\int_{S_{y,bs}}\int_{S_{y,bs}}\overline{\frac{\partial}{\partial t}p_{bs}(\boldsymbol{y},f)\frac{\partial}{\partial t}p_{bs}(\boldsymbol{y}',f)}\, dS(\boldsymbol{y})\, dS(\boldsymbol{y}') \tag{5.9}$$

where r is a distance between the measurement point and the bogie bottom surface, $S_{y,bs}$. In this study, only the pressure fluctuation correlated to the sound data was employed and the force for fluid $\boldsymbol{F_i}$ was estimated from the COP data under the assumption that the phase delay of surface pressure is negligible. The differential of local surface pressure p_{bs} was estimated in the frequency domain and the surficial integral of the square root of the COP was calculated by the sum of the multiplication of the COP data and pixel area at each calculating pixel, which was spatially averaged over a 4×4 pixels area, as follows:

$$\overline{\left(\int_{S_{y,bs}}\frac{\partial}{\partial t}\boldsymbol{F_i}(f)dS\right)^2} \sim \left(\int\overline{\frac{\partial}{\partial t}\sqrt{\mathrm{COP}(f)}}\, dS\right)^2 \cong \left(\sum_{y_p}\sum_{x_p} 2\pi k\Delta f \cdot s\sqrt{\mathrm{COP}(k)}\right)^2 \tag{5.10}$$

where k denotes a discrete frequency, s denotes the captured area per calculating pixel. Here, s on the whole surface is assumed to be 1.3 × 1.7 mm^2, which is the value at the center of the bottom surface of the bogie. Therefore, SPL from the bottom surface of the bogie were calculated from the integral of the square root of COP data as follows:

$$SPL_{est} = 10\log_{10}\frac{\overline{p_{d,bs}{}^2(f)}}{p_0^2} = 10\log_{10}\left(\frac{(k\Delta f)^2 s^2}{4a^2 r^4 p_0^2}\left(\sum_{y_p}\sum_{x_p}\sqrt{\mathrm{COP}(k)}\right)^2\right) \quad (5.11)$$

where p_0 denotes reference sound pressure (p_0 = 20 μPa).

5.3. Results and Discussion

5.3.1. Power Distribution of Sound-level and Pressure fluctuations

5.3.1.1. Sound level

Figure 5.3 shows the measured sound level of the test model at each wind velocity. The peak sound, which is shown by the black-line circles in Fig. 5.3, was found to increase remarkably at the wind velocity over U = 83.3 m/s. This peak-sound level and peak frequency were increased by increasing the wind velocity. The peak frequency f_p, the Strouhal number St, and increase in the sound level from that at U = 55.5 m/s are listed in Table 5.1. The peak sound at the wind velocity U = 55.5 m/s and 69.4 m/s was selected from the small peak sound at the frequency range from f = 300 Hz to f = 400 Hz, which is shown by the black-dashed line circles indicated in Fig. 5.3. Note that St was calculated from f_p and the length L_u between the upstream edge of the cavity and the upstream edge of the bottom surface of the bogie as follows:

$$St = \frac{L_u f_p}{U} \quad (5.12)$$

According to Table 5.1, St is almost the constant, indicating the peak noise level results from an aerodynamic phenomenon such as a cavity tone. Increase in the peak sound level ΔSPL_{mes} from that at U = 116.7 m/s is shown in Fig. 5.4. The measured value differs from the sound level at U = 116.7 m/s as follows:

$$\Delta SPL_{mes} = SPL_{mes,peak} - SPL_{mes,peak\ at\ U=116.7\ m/s} \quad (5.13)$$

Generally, aerodynamic noise in a low-Mach-number is found to increase in proportion to the sixth power of wind velocity (Iida et al. 2000; Matsui et al. 2020). The estimated peak sound level in proportion to the sixth power of wind velocity from that at U = 69.4 m/s was calculated as follows:

$$\Delta SPL_{est} = 60\log(U/69.4) + \Delta SPL_{mes\ at\ U\ =\ 69.4\ \mathrm{m/s}} \quad (5.14)$$

The peak noise level was found to increase more than the sixth power of wind velocity at wind velocity from $U = 69.4$ m/s to $U = 100.0$ m/s. This result suggests that the noise source area expands with increasing wind velocity under the condition that the sound was mainly generated from surface-pressure fluctuation.

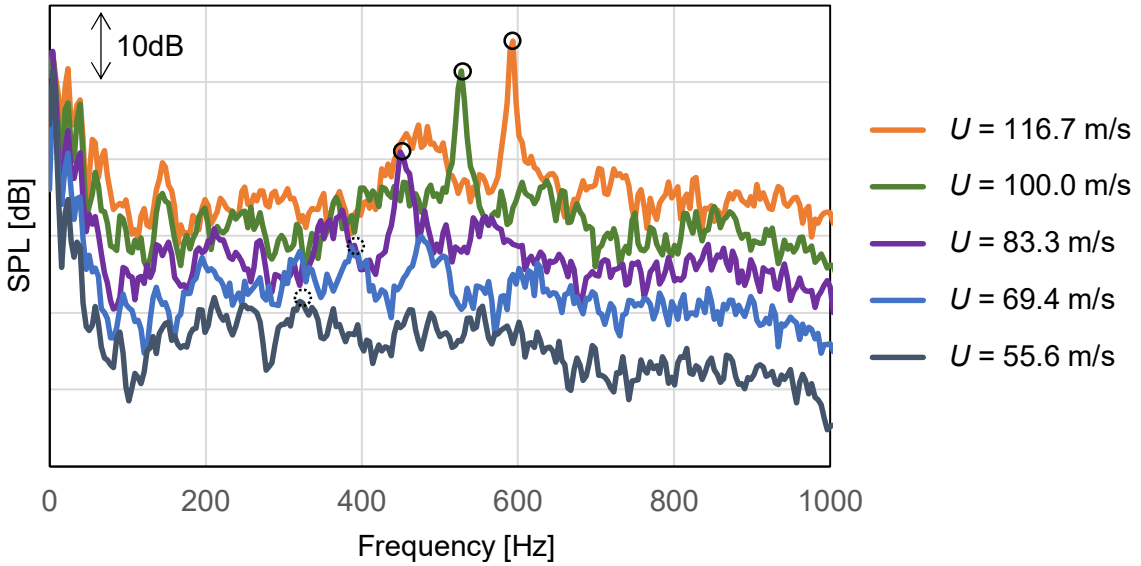

Figure 5.3 Results of frequency analysis of measured sound level radiated from the test model. The black, blue, purple, green, and orange lines show measured values at wind velocity $U = 55.6$, 69.4, 83.3, 100, and 116.7 m/s. The black-line circles show sound level.

Table 5.1 Measured sound level and peak sound frequency

Wind velocity U [m/s]	55.6	69.4	83.3	100.0	116.7
Peak frequency f_p [Hz]	335	395	449	527	594
Strouhal number St [-]	1.10	1.03	0.98	0.96	0.93
ΔSPL_{mes} [dB]	-34.7	-26.8	-14.4	-3.9	-
ΔSPL_{est} [dB]	-32.6	-26.8	-22.1	-17.3	-13.3

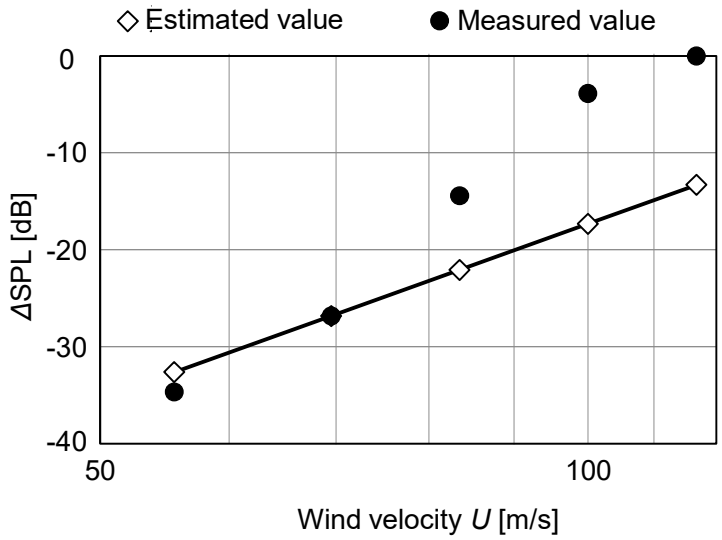

Figure 5.4 Increase in the peak sound level ΔSPL from measured sound level at U = 116.7 m/s calculated by Eq. (5.13). The black dots show measured values. The white dots show values estimated from Eq. (5.14), and the black line shows the sixth power of wind velocity determined from the measured value at U = 69.4 m/s.

5.3.1.2. Pressure fluctuation

PSD values measured by pressure transducer and PSP are compared in Fig. 5.5. The solid line shows the frequency of the measured peak sound. A peak of pressure fluctuation appears at the same frequency as the peak sound level at all wind velocities. This result indicates that the bottom surface of the bogie is one of the main noise sources of the peak sound. Moreover, in the same manner as peak sound, peak pressure fluctuation increases remarkably at the wind velocity over U = 83.3 m/s. The peak pressure fluctuation measured by PSP is similar to that measured by the pressure transducer in all cases. Noise level of the PSP used in this study was estimated to be approximately 70 Pa^2/Hz from the FFT results of the wind-off image. Thus, the PSP is concluded to be able to measure the pressure similarly to the pressure transducer up to 800 Hz at wind velocity U = 116.7 m/s.

Figure 6 shows the pressure-fluctuation distribution at the frequencies f = 484, 597 and 730 Hz at the wind velocity U = 116.7 m/s. These frequencies correspond to the sound peaks shown in Fig. 5.5(d). At frequency f = 484 and 730 Hz, an area of high-pressure fluctuation appears on the upstream side of the bottom surface of the bogie, namely, near the pressure tap. As a result, the wind from the upstream cavity edge blows to the upstream side of the bottom surface of the bogie. However, high-pressure fluctuation was found on the whole surface at frequency f = 597 Hz.

The dimensionless pressure-fluctuation distribution at the peak frequency of sound at the wind velocities U = 69.4, 83.3, 100, and 116.7 m/s is shown in Figure 5.7. The dimensionless pressure fluctuation p'^2 was calculated as follows:

$$p'^2(f) = \frac{PSD(f)}{q^2} = \frac{PSD(f)}{\left(\frac{1}{2}\rho U^2\right)^2} \tag{5.15}$$

According to the figure, a high-pressure fluctuation area appears at the center position of the upstream side (near the pressure tap) at wind velocity U = 69.4 and 83.3 m/s, where the center position is shown as a white circle in the figure. The high-pressure fluctuation areas expand to the whole area toward the downstream direction with increasing wind velocity. This result suggests that the peak noise results from expansion of the high-pressure-fluctuation area in the downstream direction on the bottom surface of the bogie with increasing wind velocity. It also suggests that the peak pressure fluctuation was generated on the upstream side of the bottom surface of the bogie and expanded in the downstream direction with increasing the wind velocity.

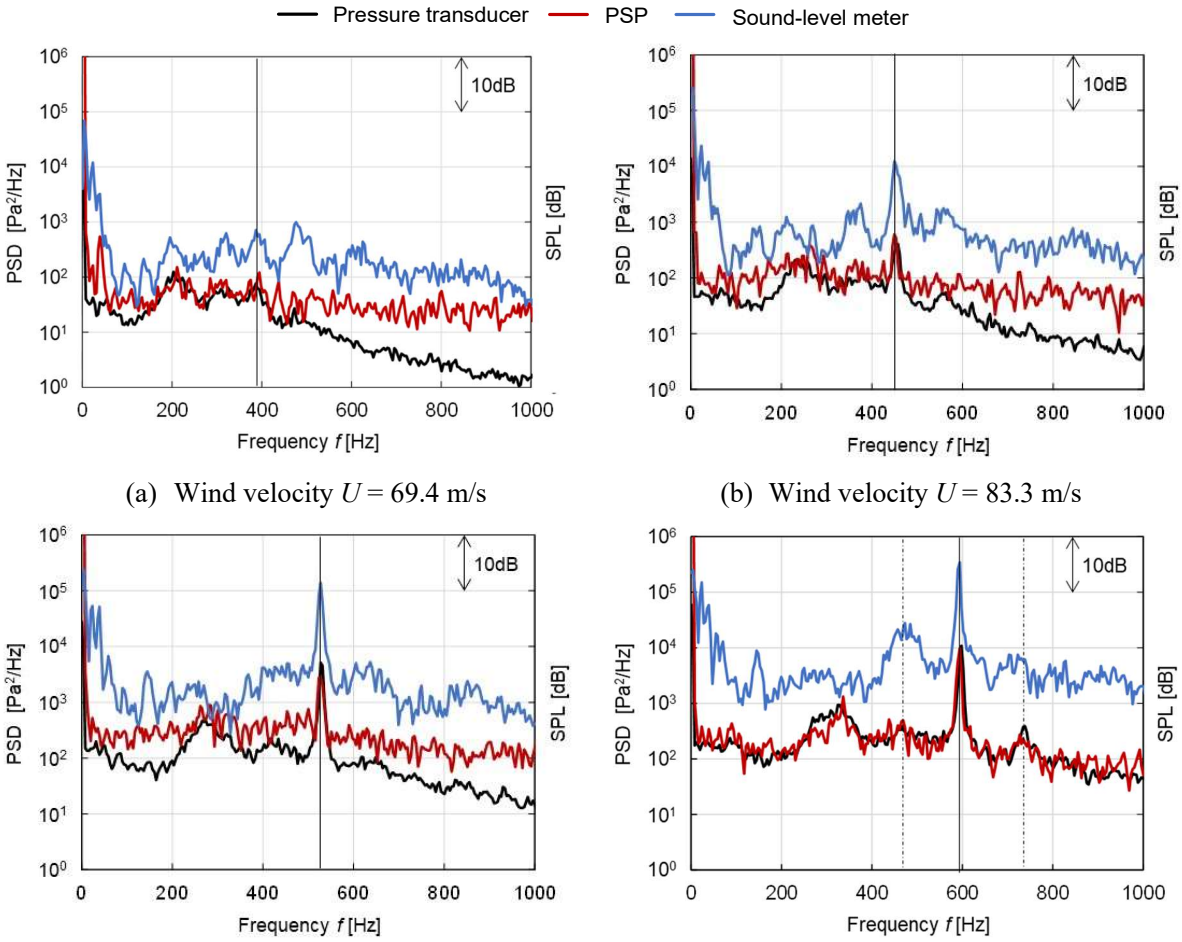

(a) Wind velocity U = 69.4 m/s

(b) Wind velocity U = 83.3 m/s

(c) Wind velocity U = 100 m/s

(d) Wind velocity U = 116.7 m/s

Figure 5.5 Comparison of PSD values measured by pressure transducer and PSP with SPL. The black and red lines show values measured by pressure transducer and PSP, respectively. The blue line shows SPL measured by the sound-level meter.

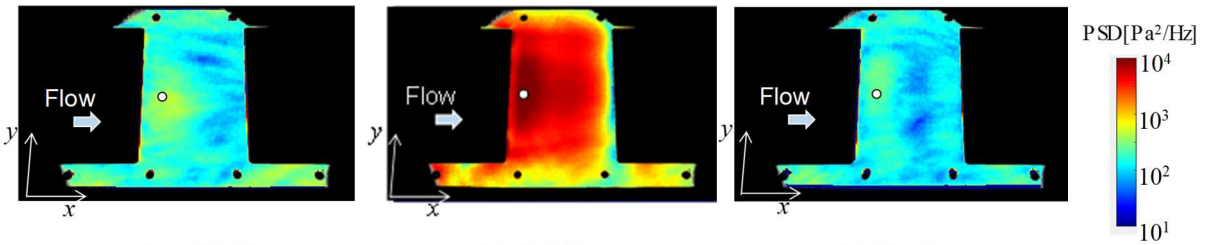

(a) 484 Hz (b) 597 Hz (c) 730 Hz

Figure 5.6 Measured pressure fluctuation distribution at wind velocity U = 116.7 m/s

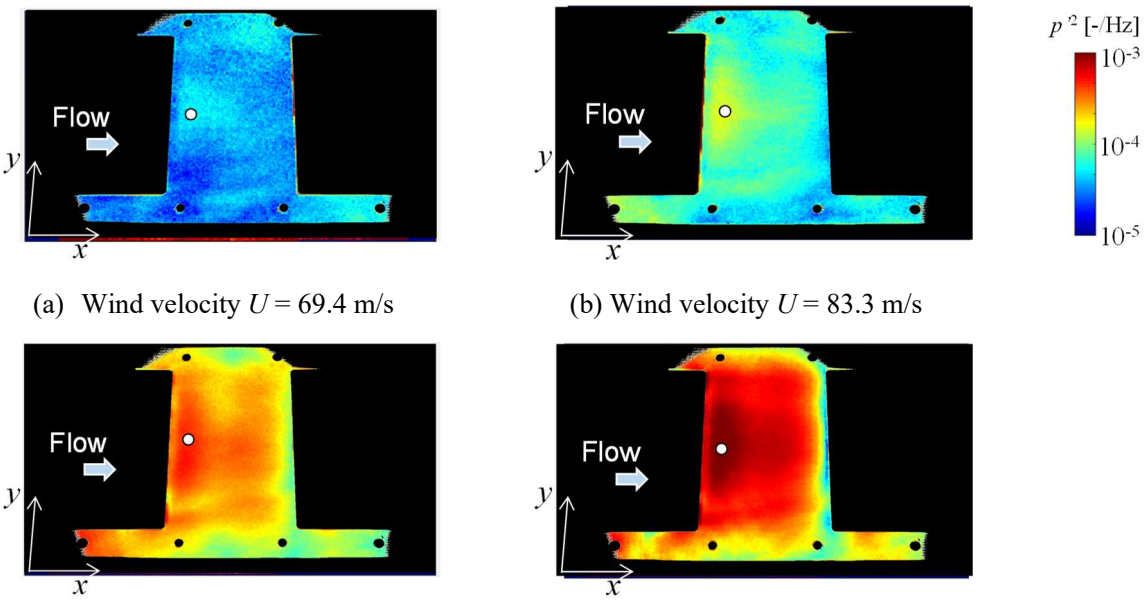

(a) Wind velocity U = 69.4 m/s (b) Wind velocity U = 83.3 m/s

(c) Wind velocity U = 100 m/s (d) Wind velocity U = 116.7 m/s

Figure 5.7 Measured dimensionless pressure-fluctuation distribution at frequency of peak sound level

5.3.2. Coherence and Phase between Pressure Fluctuations

5.3.2.1. Coherence and phase shift

Coherence γ_{PSP}^2 and phase shift ϕ_{PSP}, based on the PSP data near the pressure tap, shown as a white dot in Fig. 5.7, were calculated from the measured time-series pressure distribution. Figures 5.8 and 5.9 show the coherence and phase-shift distributions at the peak sound frequency, respectively. Coherence and phase shift on each pixel at the centerline position, which are illustrated as dashed lines in Figs. 5.8 and 5.9, are shown in Figure 5.10. The origin of streamwise position x was set to be that of the pressure tap. According to Figure 5.8, the high-coherence area expands with increasing the wind velocity. The high-coherence area is only near the pressure tap (shown as a white circle) at the wind velocity U = 69.4 m/s. At the wind velocity over U = 83.3 m/s, the coherence value near the pressure tap increases to about 1 and the high-coherence area expands in the width direction (y-direction) Moreover, at the wind velocity U = 116.7 m/s, the high coherence appears on the whole surface. According to Fig. 5.10(a), the coherence on the upstream side of the bottom surface of the bogie increases up to almost unity from the wind velocity U = 69.4 m/s to U = 83.3 m/s. At the wind velocity U = 116.7 m/s, the coherence value increases to unity on the whole surface. This result suggests that the wind from the

upstream edge becomes uniform at peak sound frequency with increasing wind velocity.

According to Fig. 5.9, the phase distribution at the peak sound frequency is almost constant at all wind velocities. The phase appears to be the uniform in the spanwise (y) direction and delayed into the downstream (x) direction. This result suggests that the peak sound is generated from acoustic feedback of a cavity tone. The sound wave, which is radiated from the bogie and the downstream cavity edge, makes the periodic vortex shedding from the upstream cavity edge as shown in Fig. 5.11. The bogie bottom surface was set at a lower position than the cavity edge, which implies that the vortex from the upwind cavity edge hits the whole bogie bottom surface and part of the vortex flows to the downstream cavity edge. According to Figure 5.10(b), the phase is delayed in the downstream direction at all wind velocities, and this delay is a little shorter at high wind velocity.

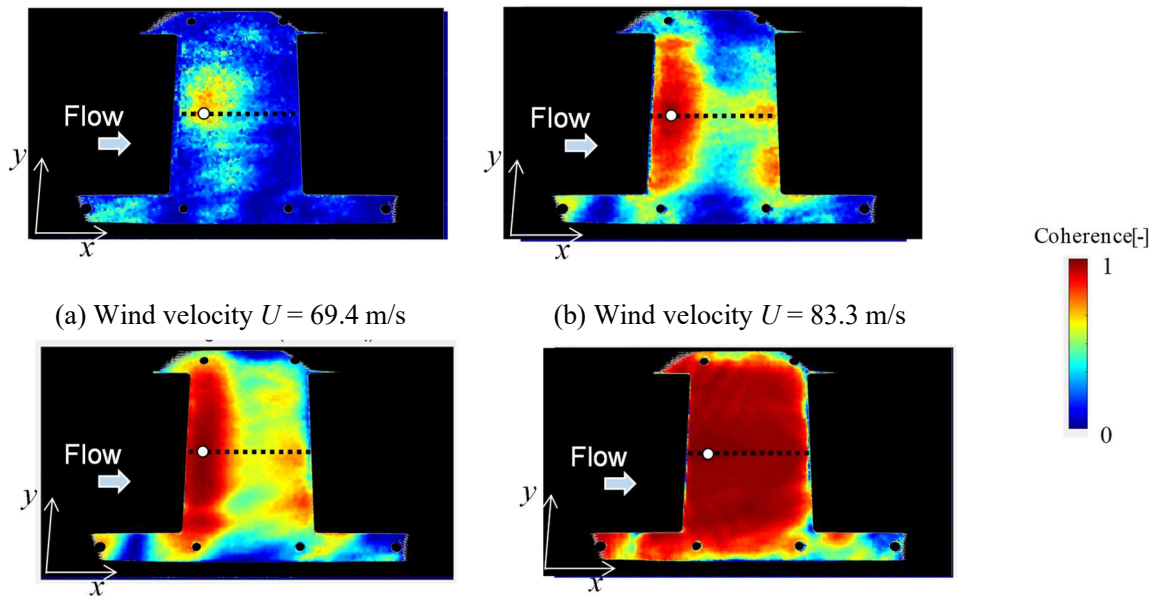

(a) Wind velocity U = 69.4 m/s (b) Wind velocity U = 83.3 m/s

(c) Wind velocity U = 100 m/s (d) Wind velocity U = 116.7 m/s

Figure 5.8 Coherence distribution at peak sound frequency based on PSP data obtained near the pressure tap

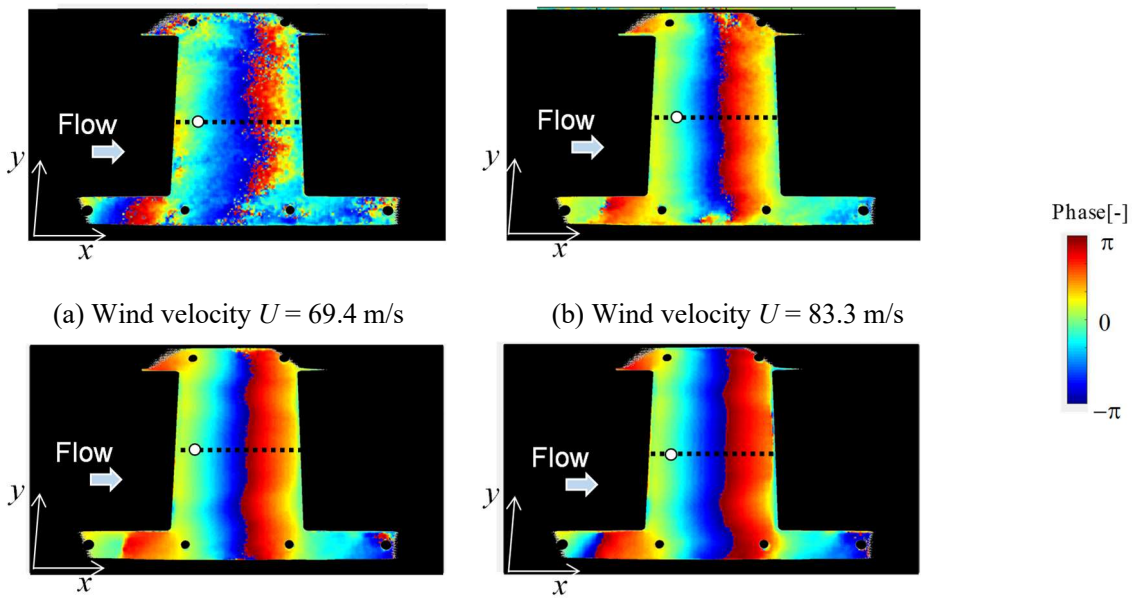

(a) Wind velocity U = 69.4 m/s (b) Wind velocity U = 83.3 m/s

(c) Wind velocity U = 100 m/s (d) Wind velocity U = 116.7 m/s

Figure 5.9 Phase-shift distribution at peak sound frequency based on the PSP data obtained near the pressure tap

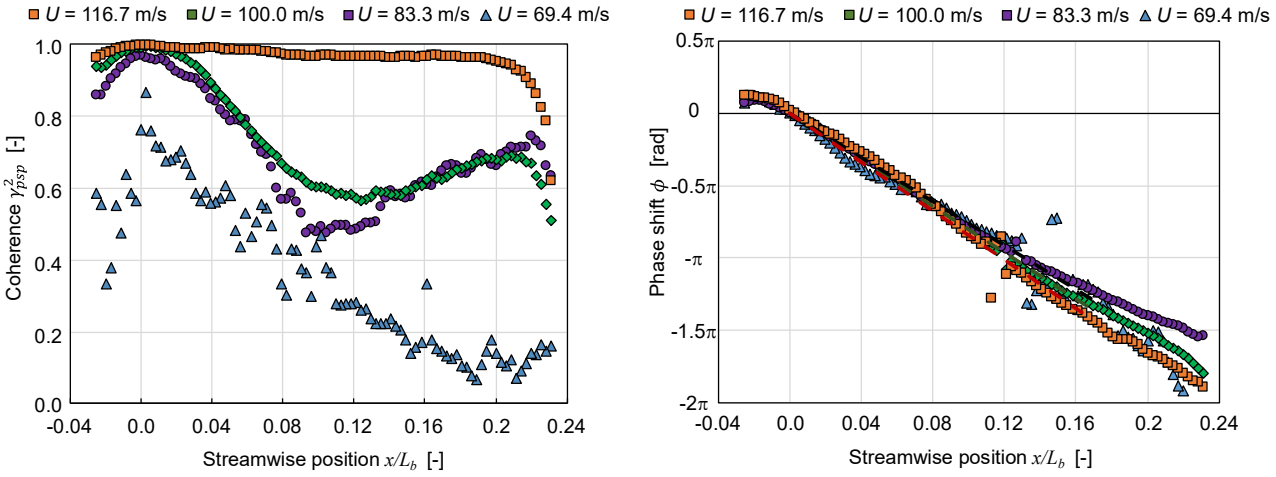

(a) Coherence (b) Phase shift

Figure 5.10 Coherence and phase shift on each pixel along the centerline based on the PSP data obtained near the pressure tap

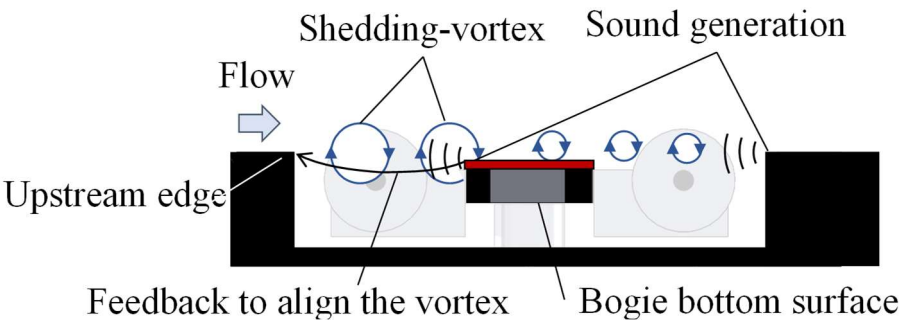

Figure 5.11 Schematic of mechanism of peak-sound generation

5.3.2.2. *Propagation speed of pressure fluctuation*

The propagation speed of the pressure fluctuation was estimated from the phase delay at peak sound frequency. The one-period delay length at the wind velocity U = 83.3, 100, 116.7 m/s was calculated by linear approximation of the phase delay from a reference point to x / L_b = 0.17 in the downstream direction. The pressure fluctuation is assumed to be propagated in accordance with the wave equation given as follows (Kosaka et al. 2017):

$$\Psi(r,t) = A_0 e^{i\left(\frac{2\pi}{\lambda}r - 2\pi f_p t\right)} \tag{5.16}$$

Also, the one-period delayed length of the pressure fluctuation was assumed to equal to the propagating wavelength λ. The pressure-fluctuation propagation speed C was calculated from the peak frequency f_p and the wavelength λ as follows:

$$\lambda = \frac{C}{f_p} \tag{5.17}$$

where Ψ denotes a wave function, and A_0 denotes an amplitude of the wave.

Estimated propagating velocities of pressure fluctuation at each wind velocity are listed in Table 5.2. When C is nondimensionalized with each freestream wind velocity U, the pressure fluctuation was revealed to propagate at approximately 66 % of the velocity normalized by the freestream wind velocity U.

Table 5.2 Propagating velocity of pressure fluctuation

Wind velocity U [m/s]	83.3	100	116.7
Phase delay [/pixel]	0.075	0.071	0.068
Wavelength of propagation λ [mm]	83.6	87.6	93.1
Peak sound frequency $f_{mes,p}$ [Hz]	449	527	594
Propagating velocity of pressure fluctuation C [m/s]	52.9	65.1	78
Dimensionless velocity C/U [-]	0.64	0.66	0.67

5.3.2.3. *Verification of cavity tone*

The measured peak sound frequency was compared with a theoretical frequency of a cavity tone and the peak sound from the test model was verified to be generated by acoustic feedback of a cavity tone. The theoretical frequency was calculated from the following equation, which shows the frequency of the peak cavity tone (Rossiter 1964):

$$St = \frac{m-\gamma}{1/\kappa + M} \tag{5.18}$$

where m is the vibration mode of the free shear layer, and M is the Mach number, κ is the dimensionless vortex convection velocity, which is given by the vortex convection velocity U_c divided by the freestream velocity U, and γ is the phase-correction constant.

A previous study (Terao et al. 2011) illustrated that the vibration mode of a free shear layer, m, is determined by the ratio of momentum thickness θ of the cavity upstream side and cavity length L_u, which means $m = 2$ in this study because $L_u/\theta = 85$. The phase-correction constant, γ, which is the phase delay until the sound wave is generated by the vortex colliding with the downstream edge of the cavity, is generally set at $\gamma = 0.25$. In addition, the vortex convection velocity U_c was assumed to be the same as the propagation speed C of the pressure fluctuation calculated in Section 5.3.2.2. The peak sound frequency of cavity tone is estimated as follows:

$$f_{p,theo} = \frac{U}{L_u}\frac{2-0.25}{\frac{U}{C}+\frac{U}{a}} \tag{5.19}$$

Measured and theoretical frequencies of peak sound are listed in Table 5.3. Table 5.3 clearly shows that the theoretical frequency of the peak sound coincides with that measured by the microphone. This result confirms that the peak sound is generated from acoustic feedback in the cavity, which is the gap between the upstream cavity edge and the bogie, as shown in Fig. 5.11.

Table 5.3 Peak noise frequency

Wind Velocity U [m/s]	83.3	100	116.7
Mach number M [-]	0.25	0.29	0.34
Propagating velocity of pressure fluctuation C [m/s]	52.9	65.1	78
Ratio of velocity κ [-]	0.64	0.66	0.67
Estimated peak noise frequency $f_{p,theo}$ [Hz]	443	530	609
Measured peak noise frequency $f_{p,mes}$ [Hz]	449	527	594

5.3.3. Coherent Output Power and Sound Estimation

5.3.3.1. Coherence between sound level and pressure fluctuations

The coherence γ^2_{sound} between the sound level and the pressure fluctuations was calculated from the PSP data and the measured sound data. The coherence at the peak sound frequency is shown in Figure 5.12, and the coherence on each pixel at the centerline position, which is illustrated as a dashed line in Fig. 5.12, is shown in Figure 5.13. Figure 5.12 presents that the high-coherence area expands with increasing the wind velocity. There is also a high-coherence area at the center of the bottom surface of the bogie at the wind velocity $U = 69.4$ m/s. At the wind velocity over $U = 83.3$ m/s, the high-coherence area expands to cover the whole surface, and the coherent value becomes almost unity with increasing the wind velocity. Figure 5.13 shows that the coherent value increases to unity with increasing the wind velocity. Moreover, the coherence is almost the same in the streamwise direction. That is considered to be the reason why the acoustic feedback becomes stronger and its effect expands the whole bogie bottom

surface as wind velocity increases. Therefore, the whole bottom surface of the bogie is a noise source and its contribution to the peak sound increases with increasing the wind velocity.

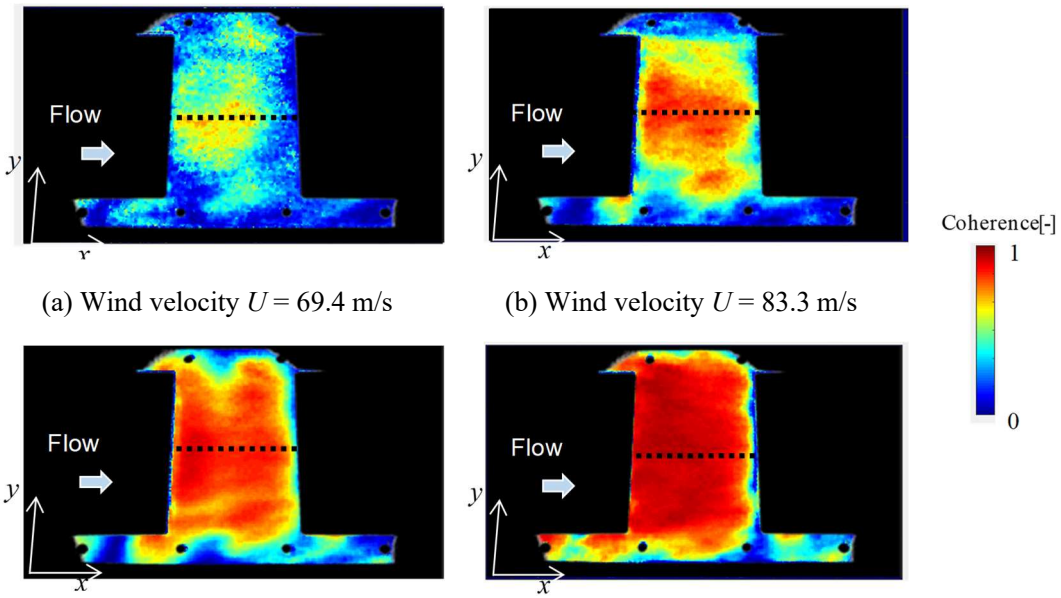

(a) Wind velocity U = 69.4 m/s (b) Wind velocity U = 83.3 m/s

(c) Wind velocity U = 100 m/s (d) Wind velocity U = 116.7 m/s

Figure 5.12 Coherence distribution at peak sound frequency based on measured sound data

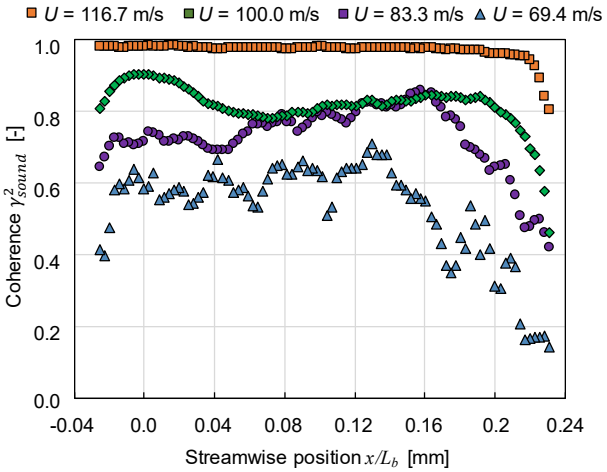

Figure 5.13 Coherence on each pixel along the centerline based on the measured sound data

5.3.3.2. Estimation of coherent output power and sound power

Then, COP was calculated from the PSP data and coherence γ^2_{sound} between the sound level and the PSP data. The COP distribution at peak sound frequency is shown in Figure 5.14. At all the sound velocities, a high-COP area appears on the upstream side of the bottom surface of the bogie, indicating that the bottom surface is one of the sound sources. The COP value at wind velocity U = 69.4 m/s and 83.3 m/s is lower than the PSD value, which is shown in Fig. 5.7, because coherence γ^2_{sound} is small. In contrast, the COP value at wind velocity U = 116.7 m/s is almost the same as the PSD value because the coherence to the peak sound increases.

The measured sound level and the estimated value from the COP distribution at the peak sound frequency are shown in Fig. 5.15. The estimated sound level of the bottom surface of the bogie is lower (within 3 dB) than the measured values at the wind velocity U = 83.3 m/s and 100.0 m/s, indicating that the bottom surface of the bogie is one of the dominant sound sources of the peak sound. This estimation from the PSP data includes the only sound radiated from the bogie bottom surface and excludes that from the downstream cavity edge. This is considered to become approximately 1-2 dB the difference in the estimated and measured sound levels from the measurement result with the chamfered downstream cavity edge, which is described in the Appendix. The estimated value is larger than the measured value at U = 69.4 m/s, possibly due to the PSP-measurement error, and the result represents that the peak pressure fluctuation has the same level as the PSP noise floor. The measured sound level and that estimated from the COP distribution in the frequency range up to 1,000 Hz are shown in Figure 16. The estimated sound level of the bottom surface of the bogie shows the same trend as the measured value at the near peak sound frequency, namely, 300 - 600 Hz. The measured sound level is higher due to the background noise of the wind tunnel itself at the lower frequency than 300 Hz, but it is lower due to the PSP-measurement noise floor in the higher frequency range than 600 Hz. At U = 116.7 m/s, measured sound level at around 470 Hz is 6 dB higher than the estimated value, suggesting that this sound (at around 470 Hz) is generated by parts other than the bottom surface of the bogie. These results clearly illustrate that the bottom surface of the bogie mainly generates the peak sound and the difference in the estimated and measured sound levels is no more than 3 dB.

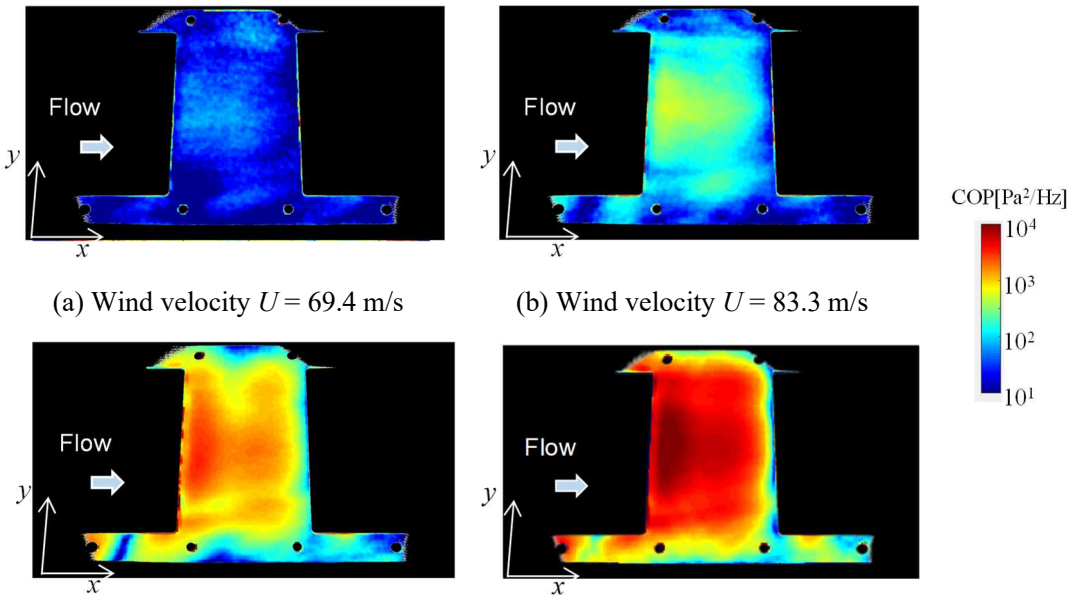

(a) Wind velocity U = 69.4 m/s (b) Wind velocity U = 83.3 m/s

(c) Wind velocity U = 100 m/s (d) Wind velocity U = 116.7 m/s

Fig. 5.14 COP distribution at peak sound frequency

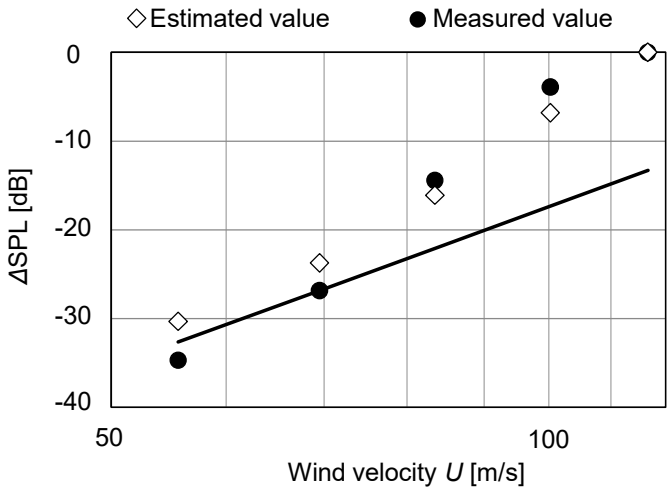

Figure 5.15 Increase of peak sound level ΔSPL from that at U = 116.7 m/s. The black solid circles show measured values and the white triangles show the COP distribution. The black line shows the sixth power of wind velocity from the measured value at U = 69.4 m/s.

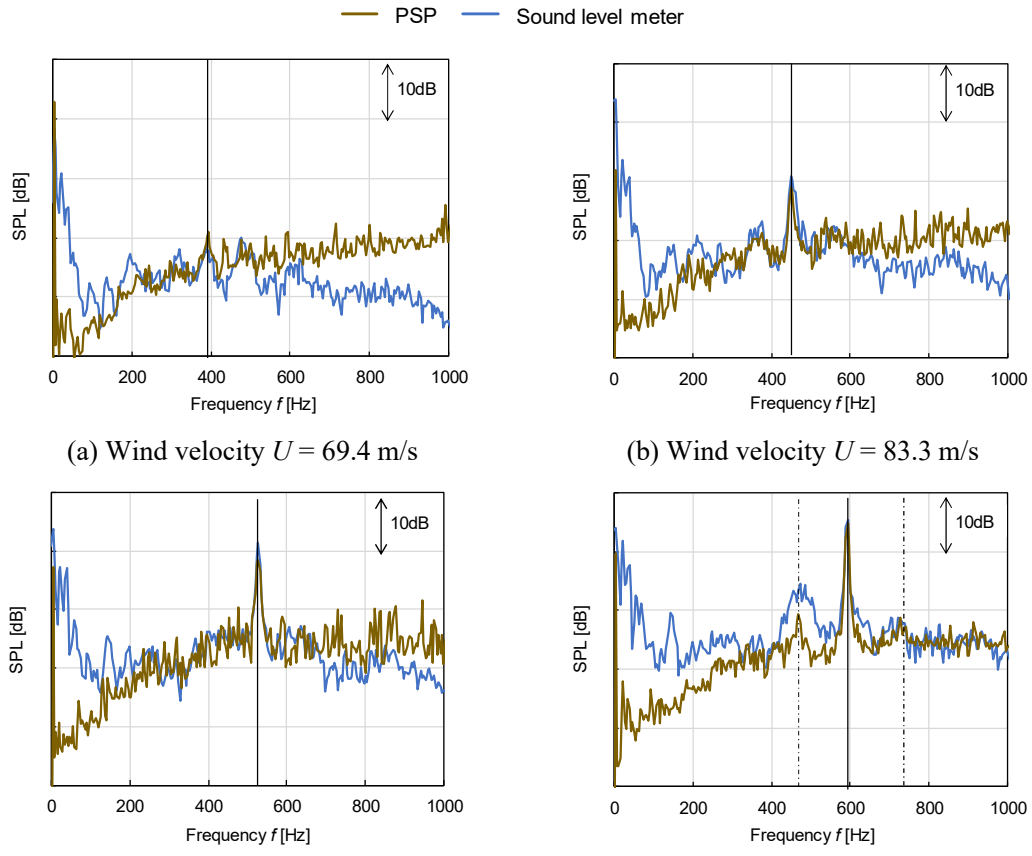

(a) Wind velocity U = 69.4 m/s

(b) Wind velocity U = 83.3 m/s

(c) Wind velocity U = 100 m/s

(d) Wind velocity U = 116.7 m/s

Figure 5.16 Comparison of measured sound level and value estimated from the COP distribution. The blue and brown lines show values measured by sound-level meter and values estimated from surface pressure fluctuation based on PSP data.

5.4. Conclusion

Sounds level from a 1/8-reduced-scale simplified model of a bogie and pressure-fluctuation distributions of the bottom surface of the bogie were measured simultaneously by a microphone and an unsteady PSP, and the sound-source distribution of a bogie section of a train was clarified. A peak sound was observed at wind velocity over 69.4 m/s, and a high-pressure-fluctuation area was observed on the upstream side on the bottom surface of the bogie at the peak sound frequency. Phase-shift distribution of the pressure fluctuation shows a delay in the downstream direction regardless of wind velocity. This result shows that the propagation speed of peak pressure fluctuation was 66 % of freestream wind velocity. Thus, measured peak sound frequency was found to be the same as theoretical cavity peak frequency given by the Rossiter equation at this propagation speed of the peak surface pressure fluctuation. Moreover, the difference between estimated and measured sound level on the bottom surface of the bogie was no more than 3 dB, where estimated sound level was calculated from the COP data by using the Lighthill-Curle equation. Therefore, the peak sound is concluded to be mainly generated by acoustic feedback in the cavity, namely, the gap between the upstream cavity edge and the bogie.

5.5. Appendix: Investigation for the effect of the downstream cavity edge

The sound-pressure level radiated from the test model and the pressure-fluctuation distribution of the bottom surface of the bogie were measured simultaneously by using a microphone and a PSP with the chamfered downstream cavity edge, and the aerodynamic sound source was further clarified. Figure 5.17 shows a right-angled and a chamfered downstream cavity edge. The height and angle of the chamfered edge were $H_{cf} = 0.25Hc$ and 45 deg., respectively.

Figure 5.18 shows the measured sound level radiated from the test model at the wind velocity $U =$ 100 m/s. Figure 5.19 shows the calculated values from the measured data of the PSP and microphone at the peak frequency of sound. The peaky sound was observed at approximately 500 Hz. The peak sound level with the chamfered downstream cavity edge was found to be 1.1 dB lower than that with the right-angled edge, indicating that the downstream cavity edge is one of the noise sources. The peak frequencies with the right-angled edge and the chamfered edge were slightly different at 520 and 531 Hz, respectively. Figure 5.19(a) and (c) show that the high-pressure-fluctuation and phase-shift distributions with a chamfered downstream cavity edge have the same tendency as that with the right-angled edge, which represents that acoustic feedback in the cavity, which is the gap between the upstream cavity edge and the bogie, occurs independently on the downstream cavity edge. The coherence distribution on the PSP data obtained near the pressure tap shown in Figure 5.19(b) illustrates that the high-coherence area with the chamfered downstream cavity edge was on the whole bogie bottom surface, while that with the right-angled downstream cavity edge was observed only at the upstream side of the surface. This is why acoustic feedback from the downstream cavity edge may occur and affect the vortex shedding from the upstream cavity edge to the bogie bottom surface. The coherence distribution on the measured sound data, shown in Figure 5.19(d), presents that the coherence value with the chamfered downstream cavity edge was larger than that with the right-angled downstream cavity edge, which resulted from that sound radiated from the bogie bottom surface becomes more dominant by eliminating the sound from the

downstream cavity edge. The results above shows that the downstream cavity edge is one of the main sound sources. This result also shows that the peak sound can be generated just only from acoustic feedback in the cavity, which is the gap between the upstream cavity edge and the bogie.

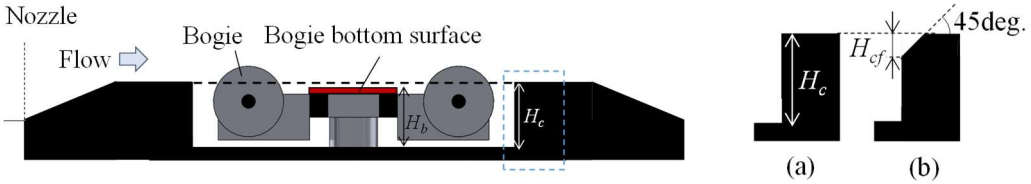

Figure 5.17 The downstream cavity edge ((a) Right-angled (original), (b) Chamfered)

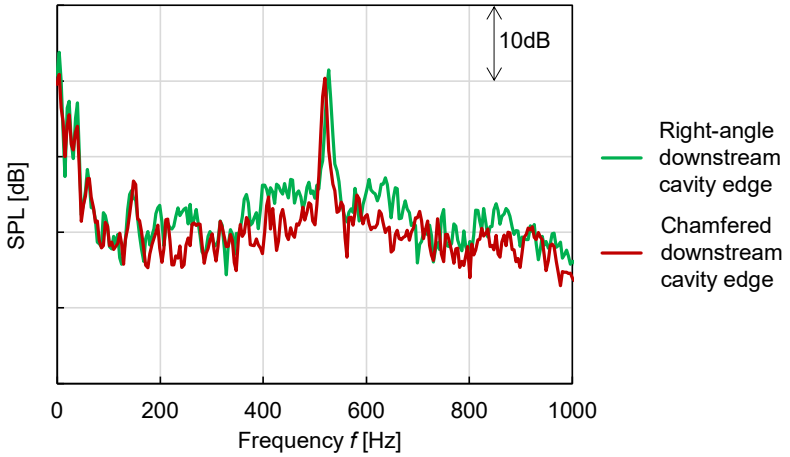

Figure 5.18 Frequency analysis of measured sound level at the wind velocity $U = 100$ m/s

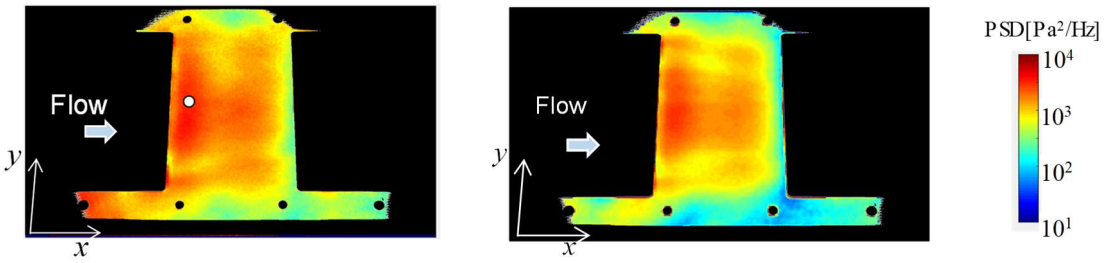

(a) Measured pressure-fluctuation distribution

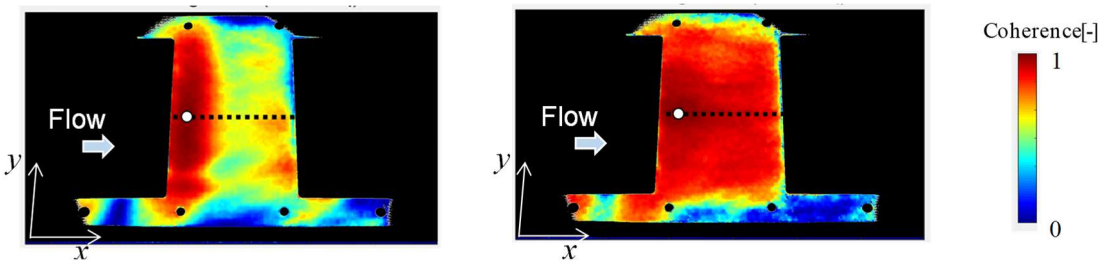

(b) Coherence distribution based on PSP data obtained near the pressure tap

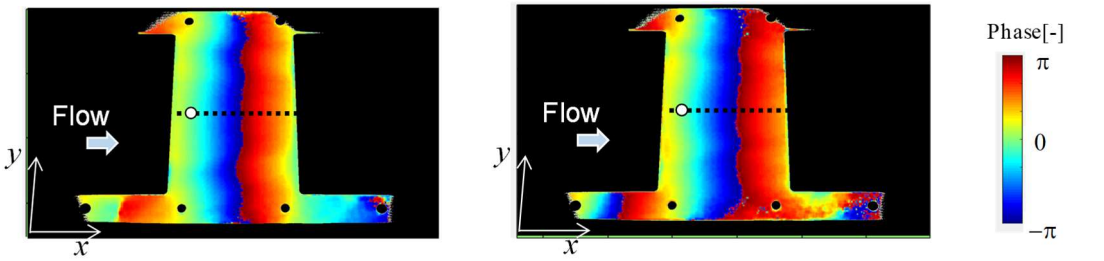

(c) Phase-shift distribution based on the PSP data obtained near the pressure tap

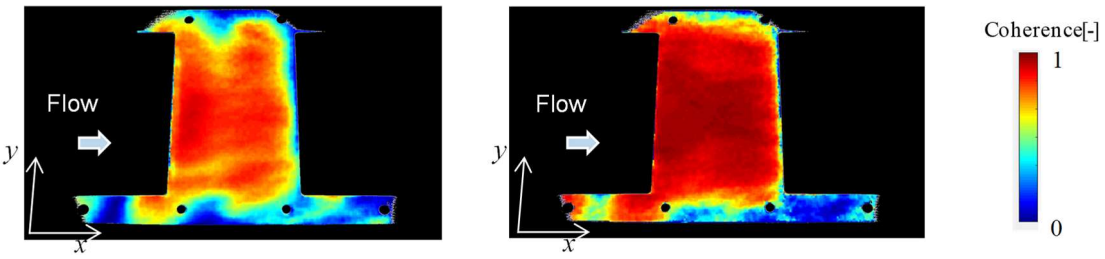

(d) Coherence distribution based on measured sound data

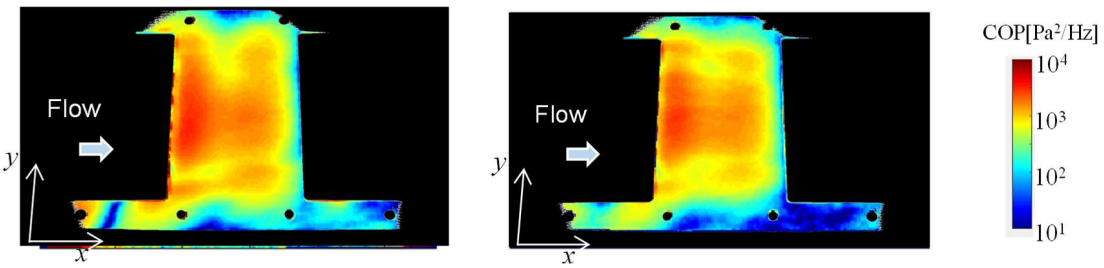

(e) COP distribution

Figure 5.19 Calculated values from the measured data of the PSP and microphone at peak sound frequency at wind velocity U = 100 m/s (Left: Right-angled (original) Right: Chamfered)

Chapter 6
Conclusions

6.1. Summary

In the present dissertation, the innovative wind tunnel testing techniques that can assess the crosswind stability and evaluate the aerodynamic noise with noise source detection were developed towards the future high-speed train with the low CO_2 emission. Firstly, in Chapter 2, the aerodynamic force and moment measurement system was developed in a compact wind tunnel for repeatable simplified evaluations of the crosswind stability. Secondly, in Chapter 3, the correlation between wind velocity and aerodynamic noise level for structure with acoustical insulation was investigated and the similarity law for accurately estimating full-scale noise from the results obtained with a reduced scale model was evaluated. Finally, in Chapters 4 and 5, pressure-sensitive paint (PSP) was applied to a complex shape. A sound-source distribution was evaluated and an unsteady phenomenon in the low-speed region was comprehended for the development of the aerodynamic noise reduction. The summaries of each chapter are described below.

6.1.1. Chapter 2

In Chapter 2, an aerodynamic force and moment measurement system including a wide nozzle and a splitter plate was developed with reference to European Norm EN14067-6 for the measurement of the force and the moment of trains precisely in a compact wind tunnel to assess crosswind stability.

The wide nozzle outlet, which has a width 3.6 times larger than its height and matches the train model, was designed , and the adequate contraction from the inlet area to the outlet area was considered by a simple equation (Hassan & Rouse). Simulation and experimental results show that the developed wide nozzle achieves the same flow quality as that in the reference wind tunnel in the European Norm.

The simulation results show that the higher splitter plate with a small nozzle increase the separation area because the flow over the train model runs insufficiently. When the splitter plate was set at the height 0.02 times the test model height, the boundary layer thickness was satisfied, and sufficient vertical space was acquired over the train model.

The force and moment measurement of the wind tunnel benchmark vehicle model shows that the average and maximum tolerances of this system are 0.086 and 0.149 from the European Norm for 5-degree yaw angles from 0 to 90 degrees.

Thus, the proposed system can satisfy the equipment and flow specifications and has the same measurement accuracy as the benchmark described in the European Norm.

6.1.2. Chapter 3

In chapter 3, we measured the aerodynamic noise radiating from cylinders without and with periodic holes and a pantograph model with and without a sound insulating plate when the flow was faster than 100 m/s in a low-noise high-speed wind tunnel and aerodynamic noise sources and the wind velocity conversion of the similarity law were assessed.

The background noise of the wind tunnel was proportional to the sixth power of wind velocity until 60 m/s and became proportional to the eighth power in a high-speed region. This dependence shows that the aerodynamic sound source of the vortex generated from the shear layer at the nozzle became dominant

as a quadrupole sound source.

A measurement of the cylinders without and with periodic holes shows that in the Reynolds number range in which the vortex formation is unchanged, the noise level of the cylinder increased in proportion to the sixth power of wind velocity as a dipole sound source, and the noise reduction effect due to the change in flow structure, such as periodic holes, also continued regardless of wind velocity. However, the second peak noise radiated from the cylinder was in proportion to the eighth power of wind velocity over 130 m/s and was underestimated by using the wind conversion based on a dipole sound source.

The noise level of the pantograph model with the sound insulating plate increased in proportion to lower than the sixth power of wind velocity in contrast to the pantograph model itself as a dipole sound source. This is the reason why the increase of the actual dominant noise level at a low frequency was reduced to less than the sixth power of wind velocity by the sound insulating plate. The plate was more effective at reducing noise at a high frequency than at a low one. In addition, by increasing the wind velocity, the dominant frequency of the pantograph noise shifted higher. These leads the dominant noise level to be affected by the noise reduction of the sound insulating plate. This caused the reduction effect of the sound insulating plate to be underestimated by 2.5 dB due to the noise level conversion of wind velocity. This problem was solved by subtracting the theoretical reduction noise level, which was calculated by using the Fresnel number, from the estimated noise level of the pantograph itself. This leads the pantograph noise with the sound insulating plate to be estimated within 0.8 dB difference.

These results indicate that the noise level radiated from cylinders and pantograph increased steadily in proportion to the sixth power by dipole sound at a wind velocity up to 116.7 m/s. However, noise at higher frequency was found to possibly increase in proportional to the sum of the sixth and eighth powers of wind velocity because a quadrupole sound source increases due to the shorter turbulent correlation length. The noise level of objects with a sound insulating structure is indicated to be lower than the sixth power of wind velocity. In conclusion, there is the possibility that a noise level estimated by wind velocity conversion generates differences from the actual noise level. Therefore, we should carefully use the similarity law when we estimate the running full-scale noise level from a reduced-scale model at a different wind velocity.

6.1.3. Chapter 4

In Chapter 4, the pressure fluctuations distribution on the floor surface behind a square cylinder in the turbulent boundary layer was measured by PSP and its accuracy and frequency response at the Mach number around, $M = 0.3$, were examined, where aerodynamic noise is mainly generated from the surface pressure fluctuations. Four types of the square cylinders were examined in the same turbulent boundary layer for detailed comprehension of the relationship between these conditions and the Kármán vortex shedding structure.

The measured values by PSP have a similar tendency to that of the pressure transducer up to 5 kHz. The peak PSD of pressure fluctuations generated by the Kármán vortex shedding from the square cylinder was observed within an error of approximately 30 % up to more than 3 kHz.

The peak frequency of the Kármán vortex shedding is found to become lower with the shorter square

cylinder similar to the previous empirical equation of the Strouhal number. The peak PSD value of the shortest square cylinder is twice higher than the other conditions and its high-pressure fluctuation area is not to be spread into the downstream, which suggests the flow from the upper end of the cylinder to become dominant in the wake rather than that from the square cylinder side. Moreover, the spatial peak coherence distribution is observed behind the tallest square cylinder, which suggests the vertical movement of the Kármán vortex shedding. In addition, The Kármán vortex is revealed to propagate at approximately 85 % of velocity normalized by the freestream wind velocity from the phase shift distribution.

One contour of the two main modes extracted as the highest PSD of the right-side singular vector at the Kármán vortex frequency have asymmetric distribution behind the taller square cylinder, which suggests that the flow from the square cylinder side becomes dominant.

6.1.4. Chapter 5

In chapter 5, sounds level from a 1/8-reduced-scale simplified model of a bogie and pressure-fluctuation distributions of the bottom surface of the bogie were measured simultaneously by a microphone and an unsteady PSP, and the sound-source distribution of a bogie section of a train was clarified.

A peak sound was observed at wind velocity over 69.4 m/s, and a high-pressure-fluctuation area was observed on the upstream side on the bottom surface of the bogie at the peak sound frequency. Phase-shift distribution of the pressure fluctuation shows a delay in the downstream direction regardless of wind velocity. This result shows that the propagation speed of peak pressure fluctuation was 66 % of freestream wind velocity. Thus, measured peak sound frequency was found to be the same as theoretical cavity peak frequency given by the Rossiter equation at this propagation speed of the peak surface pressure fluctuation. Moreover, the difference between estimated and measured sound level on the bottom surface of the bogie was no more than 3 dB, where estimated sound level was calculated from the COP data by using the Lighthill-Curle equation. Therefore, the peak sound is concluded to be mainly generated by acoustic feedback in the cavity, namely, the gap between the upstream cavity edge and the bogie.

6.2. Outlook

This dissertation shows that the developed wind testing techniques are powerful tools for the assessment of the real-scale train performance, especially crosswind stability and external noise. Hence, it is expected that these techniques are applied for the improvement of the high-speed trains at the design stage. In addition, these techniques will contribute to the improvement of the unsteady computational fluid dynamics (CFD).

In Chapter 2, the aerodynamic force and moment measurement system including a wide nozzle and a splitter plate was developed in a compact wind tunnel to assess crosswind stability. This measurement system is effective to optimize the resistant train shape to overturning. Moreover, the design method of the nozzle curve and the splitter plate position with using CFD can be applied to the development of the wind tunnel. However, it is also important to preliminary assess the crosswind stability by CFD for the development of the train shape because CFD can easily produce new shape and assess its impact. The

combination approach of this measurement system and the CFD is expected to contribute to the rapid improvement the crosswind stability with the CFD validation by the experimental results.

Chapter 3 revealed the correlation between wind velocity and aerodynamic noise level. The noise level with the acoustical insulation was found to be accurately estimated from subtracting its theoretical noise reduction from that without it. This similarity law is utilized to estimate accurately full-scale noise from the results obtained with a reduced scale model at the design stage of the high-speed train. However, the similarity law is required to be assessed for precise noise estimation when the train runs at more than 420 km/h, that is the maximum wind speed in this wind tunnel test, because from the noise source is expected to be changed from the dipole sound source to the quadrupole sound source depending on the frequency band. In addition, the correlation between the model scale and aerodynamic noise level is required to be investigated by the wind tunnel tests with different sizes on the same model for accurate full-scale noise estimation.

In Chapter 4 and 5, PSP measurement is found to be effective tools for aerodynamic noise detection and its noise level estimation from the measured surface pressure fluctuations in the low-speed region around the Mach number $M = 0.3$. PSP measurement will contribute to easily detect the sound source position and investigate the countermeasure structure for the train cars development. Moreover, the results from PSP measurement can be applied to the validation of the unsteady computational fluid dynamics. However, it is desirable to detect the source and reduce not only of the peak sound but also for the broadband sound for low-external-noise train. The improvements of SNR and frequency response of PSP are expected for accurately acquiring the correlation between the sound level and PSP data.

The developed wind testing techniques and knowledges in this dissertation is expected to be applied to the improvement of the crosswind stability and reduction of the external noise at the design stage of high-speed train, which finally leads to contribute to achieve carbon neutral by supporting the development of trains with the low CO_2 emission.

References

Asai K, Yorita D (2011) Unsteady PSP measurement in low-speed flow-overview of recent advancement at Tohoku University. 49th AIAA Aerospace Sciences Meeting including the New Horizons Forum and Aerospace Exposition, AIAA 2011-0847.

Barbara LS, Chakravarty R., Sumner D, Bergstrom DJ (2020) Aerodynamic forces and three-dimensional flow structures in the mean wake of a surface-mounted finite-height square prism. Int. J. Heat Fluid Flow 83, 108569. https://doi.org/10.1016/j.ijheatfluidflow.2020.108569.

Bell JH, Schairer ET, Lawrence A, Hand LA, Mehta RD (2001) Surface pressure measurements using luminescent coatings. Annu Rev Fluid Mech 33:155–206

Bendat JS, Piersol AG (1980) Engineering applications of correlation and spectral analysis. Wiley, New York

Bocciolone M, Cheli F, Corradi R, Mugiasca S, Tomasini G (2008) Crosswind action on rail vehicles: Wind tunnel experimental analyses. Journal of Wind Engineering and Industrial Aerodynamics, Vol. 96, , 584-610

Bourgeois JA, Sattari P, Martinuzzi RJ (2011) Alternating half-loop shedding in the turbulent wake of a finite surface-mounted square cylinder with a thin boundary layer. Phys. Fluids 23, 095101. https://doi.org/10.1063/1.3623463.

Brambilla E, Giappino S, Tomasini G (2022) Wind tunnel tests on railway vehicles in the presence of windbreaks: Influence of flow and geometric parameters on aerodynamic coefficients. Journal of Wind Engineering and Industrial Aerodynamics, 220, 104838

British Standards Institution, BS EN 14067-6:2010; Railway applications. Aerodynamics. Requirements and test procedures for cross wind assessment, (2010)

Centre Scientifique et Technique du Bâtiment (French: Scientific Center and Technical Building), Jules Verne climatic wind tunnel, (accessed on 5 January, 2023) https://www.cstb.fr/assets/documents/cstb-jules-verne-climatic-wind-tunnel.pdf

Cheli, F., Ripamonti, F., Rocchi, D. and Tomasini, G., Aerodynamic behaviour investigation of the new EMUV250 train to cross wind, Journal of Wind Engineering and Industrial Aerodynamics, 98, p.189-201, 2010

Chen G, Li X, Sun B, Liang X (2022) Effect of incoming boundary layer thickness on the flow dynamics of a square finite wall-mounted cylinder, Phys. Fluids **34,** 015105 (2022); doi: 10.1063/5.0076541

Crafton JW, Gregory JW, Sellers ME, Ruyten W (2017) Data processing tools for dynamic pressure-sensitive paint. In: 55th AIAA Aerospace Sciences Meeting. AIAA-2017–0701

Curle N (1955) The Influence of Solid Boundaries upon Aerodynamic Sound. Proceedings of the Royal Society of London, Series A, Mathematical and Physical Sciences, Vol. 231, pp. 505–514.

Diedrichs B (2005) Computational Methods for Crosswind Stability of Railway Trains – A Literature Survey, TRITA-AVE Report 2005:27, ISSN 1651-7660, Dep. of Aeronautical and Vehicle Engineering, KTH Royal Institute of Technology, Stockholm, Sweden

Disotell KJ, Gregory JW (2011) Measurement of transient acoustic fields using a single-shot pressure-sensitive paint system, Rev. Scient. Instrum. 82, 075112

El Hassan M, Bourgeois JA, Martinuzzi RJ (2015) Boundary layer effect on the vortex shedding of wall-mounted rectangular cylinder. Exp. Fluids 56, 33. https://doi.org/10.1007/s00348-014-1882-6

Egami Y, Sato Y, Konihsi S (2019) Development of sprayable pressure sensitive paint with a response time of less than 10 μs. AIAA J 57:2198–2203. https://doi.org/10.2514/1.J057434

European Commission , Working Group Railway Noise of the European Commission, Position Paper on the European strategies and priorities for railway noise abatement, ISBN 92-894-6055-5, 2003, https://rigolett.home.xs4all.nl/Archief-geluid/Position%20Paper%20on%20the%20European%20strategies%20and%20priorities%20for%20railway%20noise%20abatement%202003.pdf

Fujita H, Suzuki H, Nagarekawa H, Sagawa A, Takaishi T (1999) The Aeolian Tone Characteristics of a Circular Cylinder in High Reynolds Number Flow, 5th AIAA/CEAS Aeroacoustic Conference, Paper No. AIAA- 99–1849.

German-Dutch Wind Tunnels, KRYO-KANAL KÖLN, (accessed on 5 January, 2023) https://www.dnw.aero/assets/DocumentLibrary/Brochures/KKK-Brochure.pdf

Giappino S, Rocchi D, Schito P, Tomasini G (2016) Cross wind and roll over risk on lightweight railway vehicles, Journal of Wind Engineering and Industrial Aerodynamics, 153, p.106-112

Goldman S (1999) Vibration spectrum analysis: a practical approach, 2nd edn. Industrial Press, New York

Gößling J, Ahlefeldt T, Hilfer M (2020) Experimental validation of unsteady pressure-sensitive paint for acoustic applications, Exp. Therm. Flu. Sci. 112, 109915

Gößling J, Fischer F, Seume JR, Hilfer M (2023) Uncertainty and validation of unsteady pressure-sensitive paint measurements of acoustic fields under aero engine-like conditions, Exp. Fluids 64:22.

Gregoire R, Paradot N, Bouchet, JP (2009) Determination of aeodynamic coefficients of the TGV Duplex in wind tunnel for flat ground configurations, Proceedings of EuroMech colloquium 509, Vehicle Aerodunamics.

Gregory JW, Sakaue H, Sullivan JP, Raghu S (2001) Characterization of miniature fluidic oscillator flowfields using porous pressure sensitive paint. In: Proceedings of the ASME fluid engineering division-summer meeting, New Orleans, LA, FEDSM-2001-18058

Gregory JW, Sakaue H, Liu T, Sullivan JP (2014) Fast pressure-sensitive paint for flow and acoustic

diagnostics. Annu Rev Fluid Mech 46:303–330

Gregory JW, Sullivan JP, Wanis SS, Komerath NM (2006) Pressure-sensitive paint as a distributed optical microphone array, The Journal of the Acoustical Society of America, 119, 251

Hibino Y, Shimomura T, Tanifuji K (2009) Verification of Static Analysis on Railway Vehicle Overturning under Crosswind, Transactions of the JSME (in Japanese), Vol. 75, No. 758, pp.2605-2612

Hibino Y, Kanemoto H, Shimomura T (2013) Safety Evaluation of Railway Vehicle against Crosswind Applying a Full-vehicle Model, Quarterly Report of RTRI, Volume 54 Issue 3 Pages 133-138

Hitachi, ltd. (2014) News release, http://www.hitachi.co.jp/New/cnews/month/2014/04/0407.html

Hoefener L, Romann D, Nayeri CN, Tielkes T, Paschereit CO (2009) Wind tunnel experiments of a high-speed train exposed to cross wind on ground and bridge configurations, Proceedings of EuroMech colloquium 509, Vehicle Aerodunamics, pp.117-129

Hosseini Z, Bourgeois JA, Martinuzzi RJ (2013) Large-scale structures in dipole and quadrupole wakes of a wall-mounted finite rectangular cylinder. Exp. Fluids 54, 1595. https://doi.org/10.1007/s00348-013-1595-2.

Iida A, Otaguro T, Nagarekawa H, Torii A, Naruse I (2000) Similarity Law of Aerodynamic Noise Generation, 6th AIAA/CEAS Aeroacoustic Conference, Paper No. AIAA-2000–2012.

Iida A (2007) Similarity of Scale Model Experiments on Aeroacoustics, *Journal of the Acoustical Society of Japan,* Vol. 63, No. 9, pp. 549–554 (in Japanese).

Intergovernmental Panel on Climate Change, Climate Change 2021 -The Physical Science Basis- Summary for Policymakers, Working Group I Contribution to the Sixth Assessment Report of the Intergovernmental Panel on Climate Change, 2021,
https://www.ipcc.ch/report/ar6/wg1/downloads/report/IPCC_AR6_WGI_SPM_final.pdf

International Energy Agency, The IEA Mobility Model, A comprehensive transport modelling tool aimed at improving the analysis of all the aspects of mobility, GHG intensity of passenger transport modes, 2019 https://www.iea.org/data-and-statistics/charts/ghg-intensity-of-passenger-transport-modes-2019

Ishihara T, Zhang D, Nagumo Y (2021) Numerical study of dynamic response of railway vehicles under tunnel exit winds using multibody dynamic simulations, Journal of Wind Engineering and Industrial Aerodynamics, Vol. 211, 104556

Kanda H, Tsuda H, Ichikawa K Yoshida S (2008) Environmental Noise Reduction of Tokaido Shinkansen and Future Prospect, Noise and Vibration Mitigation for Rail Transportation Systems, Proceedings of the 12th International Workshop on Railway Noise Systems, pp. 1-8.

Klein C, Henne U, Sachs WE, Egami Y, Mai H, Ondrus V, Beifuss U (2008) Application of Pressure-Sensitive Paint for Determination of Dynamic Surface Pressures on an Oscillating 2-D profile in Transonic Flow, 46th AIAA Aerospace Sciences Meeting, AIAA Paper 2008-0278

Kikuchi K, Suzuki M (2015) Study of aerodynamic coefficients used to estimate critical wind speed for vehicle overturning, Journal of Wind Engineering and Industrial Aerodynamics, Vol. 147, 1-17

Kindree, MG, Shahroodi M, Martinuzzi RJ (2018) Low-frequency dynamics in the turbulent wake of cantilevered square and circular cylinders protruding a thin laminar boundary layer. Exp. Fluids 59, 186. https://doi.org/10.1007/s00348-018-2641-x.

Kitagawa T, Nagakura K, Kurita T (2013) Contribution of Rolling Noise and Aerodynamic Noise to the Total Noise Generated from the Lower Part of Shinkansen Cars Running at High-speed, Quarterly Report of RTRI, Vol. 54, No. 4 pp. 214-221

Kitashima S, Numata D, Asai K (2014) Characterization of pressure sensitive paint containing ceramic particles. In: 16th International Symposium on Flow Visualization, ISFV16-1286.

Kobayashi R (1981) The design of the contraction nozzle for wind tunnel, The Memoirs of the Institute of High Speed Mechanics (in Japanese), Vol. 46, pp.17-37

Kunieda M (1972) Theoretical Study on the Mechanics of Overturn of Railway Rolling stock. Railway Technology Research Report No. 793 (February 1972)

Kurita T (2011) Development of External-Noise Reduction Technologies for Shinkansen High-Speed Trains, Journal of Environment and Engineering, Vol. 6, No. 4, pp. 805–819.

Kurita T, Hara M, Yamada H, Wakabayashi Y, Mizushima F, Satoh H Shikama T (2010) Reduction of Pantograph Noise of High-Speed Trains, Journal of Mechanical Systems for Transportation and Logistics, Vol. 3, No.1, pp.63-74

Kurita T, Wakabayashi Y, Yamada H, Horiguchi M (2011) Reduction of Wayside Noise from Shinkansen High-Speed Trains, Journal of Mechanical Systems for Transportation and Logistics, Vol. 4, No.1, pp.1-12

Larsson J, Davidson L, Olsson M, Eriksson LE (2004) Aeroacoustic Investigation of an Open Cavity at Low Mach Number, AIAA Journal 42:12

Li W, Liu T, Martinez-Vazquez P, Guo Z, Huo X Xia Y, Chen Z (2022) Effects of embankment layouts on train aerodynamics in a wind tunnel configuration, Journal of Wind Engineering and Industrial Aerodynamics, 220, 104830

Lighthill MJ (1952) On Sound Generated Aerodynamically, *Proceedings of the Royal Society of London, Series A, Mathematical and Physical Science,* Vol. 211, pp. 564–587.

Lighthill MJ (1954) On sound generated aerodynamically. Part II: Turbulence as a source of sound, Proc. Roy Soc. London., A222, pp. 1-32

Liu T (2003) Pressure-correction method for low-speed pressure-sensitive paint measurements. AIAA J 41:906–911

Liu T, Sullivan JP (2005) Pressure and Temperature Sensitive Paints. Springer, Berlin

Liu T, Sullivan JP, Asai K, Klein C, Egami Y (2021) Pressure and Temperature Sensitive Paints 2nd edition. Springer, Berlin

Liu X, Qin C, Tang Y, Zhao K, Wang P, Liu Y, He C, Peng D (2022) Resolving dynamic features of kHz pressure fluctuations using fast PSP: measurement of inclined jet impingement, Exp. Fluids 63:72.

Liu X, Qin C, Zhao K, Wang P, Liu Y, Peng D (2022a) Identification of discrete tonal noises of high-speed inclined impingement jet using Fast PSP, AIAA J

Lumley JL (1967) The structure of inhomogeneous turbulence. In: Yaglom AM, Tatarski VL (eds) Atmospheric turbulence and wave propagation. Nauka, Moscow, pp 166–178

Maekawa Z, (1962) Experimental Study on Acoustical Designing of a Screen for Noise Reduction, Jjournal of the Acoustical Society of Japan, Vol. 18, No. 4, pp.187-196 (in Japanese)

Martens A, Wedemann J, Meunier N, Leclere A (2009) High Speed Train Noise - Sound Source Localization at Fast Passing Trains, Deutsche Bahn AG, Sociedad Espanola de Acustica, S.E.A..

Marple SL (1987) Digital spectral analysis with applications. Prentice-Hall, New Jersey

Matsui A, Watanabe T, Abe Y (2017) Aerodynamic Force and Moment Measurement for Crosswind Stability Assessment in a Compact Wind Tunnel, Mechanical Engineering Journal, Vol. 4, No. 3, p.17-00034

Matsui A, Watanabe T, Abe Y (2020) Aerodynamic noise evaluation for Aeolian tone and acoustical insulating plate by similarity law, Mechanical Engineering Journal, Vol. 7 No. 6 p.20-00183

Matsuda Y, Uchida K, Egami Y, Yamaguchi H, Niimi T (2016) Polymer-particle pressure-sensitive paint with high photostability. Sensors 16(550):1–7. https://doi.org/10.3390/s16040550

McGraw CM, Bell JH, Khalil G, Callis JB (2006) Dynamic surface pressure measurements on a square cylinder with pressure sensitive paint. Exp Fluids 40:203–211

Mellet C, Létourneaux F, Poisson F, Talotte C (2006) High speed train noise emission: Latest investigation of the aerodynamic/rolling noise contribution, Journal of Sound and Vibration, Vol. 293, Issues 3–5, pp. 535-546

Ministry of the Environment, Government of Japan, Environmental Quality Standards for Shinkansen Superexpress Railway Noise, 1993, https://www.env.go.jp/en/air/noise/railway.html

Mitsumoji T, Sato N, Yamazaki N, Uda T, Usuda T, Wakabayashi Y (2016) Reduction of Aerodynamic Noise Emitted from Pantograph by Appropriate Aerodynamic Interference Around Pantograph Head Support, Noise and Vibration Mitigation for Rail Transportation Systems, Proceedings of the 12th International Workshop on Railway Noise Systems, pp. 411-422.

Moriyama A (2011) Verification of Railway Vehicle Overturning under Crosswind by Field Data (An Effect

of the Cross-Sectional Shape of Vehicles), Transactions of The Japan society of Mechanical Engineers Series C (in Japanese), Vol. 77, 778 pp. 2389-2399

Mohammadi A, Morton C, Martinuzz R (2022) Effect of boundary layer state on the wake of a cantilevered square cylinder of aspect ratio 4, Physical Review Fluids 7, 084702 (2022)

Nakakita K (2011) Unsteady pressure measurement on NACA0012 model using global low-speed unsteady PSP technique. 41st AIAA Fluid Dynamics Conference and Exhibit, AIAA 2011-3901

Nakakita K (2013) Phase Delay and Correlation Area Detection of Unsteady Pressure Field Using Unsteady PSP Measurement. AIAA Ground Testing Conference, AIAA 2013-3124

Nakakita K, Takama Y, Imagawa K, Kato H (2012) Unsteady PSP measurement of transonic unsteady flow field around a rocket fairing model. 28th Aerodynamic Measurement Technology, Ground Testing, and Flight-Testing Conference, AIAA 2012-2578.

Noda T, Nakakita K, Wakahara M, Kameda M (2018) Detection of small-amplitude periodic surface pressure fluctuation by pressure sensitive paint measurements using frequency-domain methods. Exp Fluids 59(6):94

Noguchi Y, Kanade K (2022) Numerical Simulations of the Wind Tunnel Tests on the Aerodynamic Characteristics of Trains in the Crosswind, Quarterly Report of RTRI, Vol. 63, No.1, pp. 37-43

Noguchi Y, Suzuki M (2018) Large-eddy Simulation of the Aerodynamics of a Simplified Train under Crosswinds, Quarterly Report of RTRI, Vol. 59, No.2, pp. 115-120

Okajima A (1982) Strouhal numbers of rectangular cylinders. J. Fluid Mech. 123, 379–398.

Orellano A, Shober M (2006) Aerodynamic Performance of a Typical High-Speed Train, Proceedings of the 4th WSEAS International Conference on Fluid Mechanics and Aerodynamics., pp.18-35

Ozawa Y, Nonomura T, Mercier B, Castelain T, Bailly C, Asai K (2019) Cross-spectral analysis of PSP images for estimation of surface pressure spectra corrupted by the shot noise, Exp Fluids 60:8.

Pandey A, Gregory JW (2015) Dynamic response characteristics of polymer/ceramic pressure-sensitive paint. 53rd Aerospace Sciences Meeting, AIAA 2015-0021.

Pastuhoff M, Yorita D, Asai K, Alfredsson PH (2013) Enhancing the signal-to-noise ratio of pressure sensitive paint data by singular value decomposition. Meas Sci Technol 24:075301. https://doi.org/10.1088/0957-0233/24/7/075301

Peng D, Wang S, Liu Y (2016) Fast PSP measurements of wall-pressure fluctuation in low-speed flows: improvements using proper orthogonal decomposition. Exp Fluids 57:1–17

Peng D, Gu F, Li Y, Liu Y (2018) A novel sprayable fast-responding pressure-sensitive paint based on mesoporous silicone dioxide particles. Sens Actuators A Phys 279:390–398. https://doi.org/10.1016/j.sna.2018.06.048

Peng D, Liu Y (2020) Fast pressure-sensitive paint for understanding complex flows: from regular to harsh environments. Exp Fluids 61:8

Porteous R, Moreau D, Doolan C (2014) A review of flow-induced noise from finite wall-mounted cylinders. J Fluids Struct 51:240–254. https://doi.org/10.1016/j.jfluidstructs.2014.08.012

Porteous R, Moreau D, Doolan C (2017) The aeroacoustics of finite wall-mounted square cylinders, Journal of Fluid Mechanics, Vol. 832, pp.287-328

Politecnico di Milano Wind Tunnel laboratory (GVPM), Facility, https://www.windtunnel.polimi.it/facility/ (accessed on 5 January, 2023)

Rocchi, D., Cheli, F., Ripamonti, F., Tomasini, G. and Zanetti, G., Design of Ansaldobreda High Speed Trains According to the TSI Crosswind Requirements, The 8th World Congress on Railway Research, PS.2.36 (2008)

Rocchi, D., Schober, M., Cheli, F., Orellano, A. and Tomasini, G., Comparison of wind tunnel tests results on th ATM train, Proceedings of EuroMech colloquium 509, Vehicle Aerodunamics, pp.229-238, 2009

Rossiter JE (1964) Wind-tunnel experiments on the flow over rectangular cavities at subsonic and transonic speed, Aeronautical Research Council Reports and Memoranda, No. 3438.

Rouse, H. and Hassan, M. M., Cavitation-free inlets and contractions (Electrical analogy facilitates design problem), Mechanical Engineering., Vol.71 (1949), pp.213-216

Rud, N., Loose, S., Kowalski, T., Ruter, A., Schober, M. and Stiepel, M., Reference wind tunnel measurements on aerodynamic coefficients of ICE3 end car, Proceedings of EuroMech colloquium 509, Vehicle Aerodunamics, pp.239-250, 2009

Sakamoto H, Arie M (1983) Vortex shedding from a rectangular prism and a circular cylinder placed vertically in a turbulent boundary layer. J Fluid Mech 126:147–165. https://doi.org/10.1017/S002211208 3000087

Sakaue H, Kakisako T, Ishikawa H (2011) Characterization and optimization of polymer-ceramic pressure-sensitive paint by controlling polymer content. Sensors 11(7):6967–6977

Saito M, Mizushima F, Wakabayashi Y, Kurita T, Nakajima S and Hirasawa T, Development of New Low-Noise Pantograph for High-Speed Trains, Noise and Vibration Mitigation for Rail Transportation Systems, Proceedings of the 13th International Workshop on Railway Noise Systems, 2019, pp. 81-89.

Sawamura Y, Uda T, Kitagawa T, Yokohama H and Iida A, Measurement and Reduction of the Aerodynamic Bogie Noise Generated by High-Speed Trains in Terms of Wind Tunnel Testing, Noise and Vibration Mitigation for Rail Transportation Systems, Proceedings of the 13th International Workshop on Railway Noise Systems, 2019, pp. 73-80.

Schober M, Weise M, Orellano A, Deeg P and Wetzel W, Wind tunnel investigation of an ICE 3 endcar on

three standard ground scenarios, BBAA VI International Colloquium on: Bluff Bodies Aerodynamics & Applications Milano, Italy, July, 20–24 2008

Scroggin AM, Slamovich EB, Crafton JW, Lachendro N, Sullivan JP (1999) Porous polymer/ceramic composites for luminescent-based temperature and pressure measurement. MRS Proc 560:347. https://doi.org/10.1557/PROC-560-347

Sica G, Solé J and Huguenet P, Pass-By Noise Assessment of High Speed Units by Means of Acoustic Measurements in a Perimeter Close to the Train, Noise and Vibration Mitigation for Rail Transportation Systems, pp 98–105, 2021, https://doi.org/10.1007/978-3-030-70289-2_8

Sellers ME, Nelson MA, Roozeboom NH, Burnside NJ (2017) Evaluation of unsteady pressure-sensitive paint measurement technique for space launch vehicle buffet determination. AIAA Scitech Forum, 9-13 Jan.2017, Grapevine, Texas: AIAA 2017-1402

Sugimoto T, Kitashima S, Numata D, Nagai H, Asai K (2017) Characterization of frequency response of pressure-sensitive paints. AIAA J. 55:4, 1460-1464. https://doi.org/10.2514/1.J054985

Sugioka Y, Arakida K, Kasai M, Nonomura T, Asai K, Egami Y, Nakakita K (2018) Evaluation of the characteristics and coating film structure of polymer/ceramic pressure-sensitive paint, Sensors 18:11, 4041.

Sugioka Y, Nakakita K, Koike S, Numata D, Nonomura T, Asai K (2018a) Experimental analysis of transonic buffet on a 3D swept wing using fast-response pressure-sensitive paint, Exp Fluids 59:6. https://doi.org/10.1007/s00348-018-2565-5

Sugioka Y, Numata D, Asai K, Koike S, Nakakita K, Nakajima T (2018b) Polymer/ceramic pressure-sensitive paint with reduced roughness for unsteady measurement in transonic flow. AIAA J 56(6):2145–2156

Sugioka Y, Hiura K, Chen L, Matsui A, Morita K, Nonomura T, Asai K (2019) Unsteady pressure sensitive paint (PSP) measurement in low-speed flow: characteristic mode decomposition and noise floor analysis. Exp Fluids 60:108. https: //doi.org/10.1007/s00348-019-2755-9

Sugioka Y, Nakakita K, Koike S, Nakajima T, Nonomura T, Asai K (2021) Characteristic unsteady pressure field on a civil aircraft wing related to the onset of transonic buffet. Exp Fluids 62:20. https://doi.org/10.1007/s00348-020-03118-y

Sumner D, Rostany N, Bergstrom DJ, Bugg JD (2017) Infuluence of aspect ratio on the mean flow field of a surface-mounted finite-height square prism, International Journal of Heat and Fluid Flow, Vo.65, pp.1-20

Suzuki M, Tanemoto K, Maeda T (2003) Aerodynamic characteristics of train/vehicles under cross winds, Journal of Wind Engineering and Industrial Aerodynamics, Vol. 91, No.1-2, pp. 209-218

Suzuki M (2011) Wind Tunnel Test of Railway Vehicle Under Cross Wind Using Moving Model Rig, Wind Engineers, JAWE (in Japanese), Vol. 128, No.3, pp.258-263

Suzuki M (2015) Wind tunnel experiment for cross wind effects on trains according to EN14067-6,

Proceedings of Anuual Meeting 2015 (in Japanese), Japan Association for Wind Engineering, p.201-202

Takaishi T, Ikeda M, Kato C (2003) Effects of Periodic Holes on the Suppression of Aeroacoustic Noise from a Pantograph Horn, Proceedings of ASME FEDSM'03 4th ASME/JSME Joint Fluids Engineering Conference, Paper No. FEDSM2003-45464, p.41-48.

Takano Y, Sasaki K, Satoh T, Murata K, Mae H, Goto J (2003) Development of Visualization System for High-Speed Noise Sources with a Microphone Array and a Visual Sensor. inter-noise 2003. N930. 2683-2689

Tanemoto K, Suzuki M, Saitou H Ido A (2013) Results of Wind Tunnel Tests for Aerodynamic Coefficients of Railway Vehicles, RTRI reports (in Japanese), Vol. 27, No.1, pp. 47-54

Technical specification for interoperability relating tothe 'rolling stock' sub-system of the trans-European high-speed rail system, (2008)

Technical specification for interoperability relating to the 'rolling stock — locomotives and passenger rolling stock' subsystem of the rail system in the European Union., (2014)

Terao K, Yokoyama H, Ogoe Y, Iida A (2011) Proposition of a New Formula for Frequency Prediction Based on Generation Mechanism of Aerodynamic Sound in Cavity Flows, Transactions of the Japan Society of Mechanical Engineers, Series B, Vol. 77, No. 779, pp. 1522-1532 (in Japanese)

Thompson D (2010) Railway Noise and Vibration - Mechanisms, Modelling and Means of Control-, Elsevier Science, https://doi.org/10.1016/B978-0-08-045147-3.X0023-0

Thompson D, Iglesias EL, Liu X, Zhu J, Hu Z (2015) Recent developments in the prediction and control of aerodynamic noise from high-speed trains, International Journal of Rail Transportation, Vol. 3, No. 3, pp.119–150, https://doi.org/10.1080/23248378.2015.1052996

Tomasini G, Giappino S, Corradi R (2014) Experimental investigation of the effects of embankment scenario on railway vehicle aerodynamic coefficients, Journal of Wind Engineering and Industrial Aerodynamics, 131, p.59-71

Uchida K, Sugioka Y, Kasai M, Saito Y, Nonomura T, Asai K, Nakakita K (2021) Analysis of transonic buffet on ONERA-M4 model with unsteady pressure-sensitive paint, Exp Fluids 62:6. https://doi.org/10.1007/s00348-021-03228-1

Uda T, Yamazaki N, Kitagawa T, Nagakura K, Wakabayashi Y (2016) Estimation of Aerodynamic Bogie Noise Through Field and Wind Tunnel Tests, Noise and Vibration Mitigation for Rail Transportation, Proceedings of the 12th International Workshop on Railway Noise Systems, pp.377-388.

Union des Industries Ferroviaires Européennes, Unife Global Rail Market Grows Despite COVID-19 (World Rail Market Study: Forecast 2020 to 2025) World Rail Market Study, https://www.unife.org/news/global-rail-market-grows-despite-covid-19-world-rail-market-study-forecast-2020-to-2025/

United Nations Treaty Collection, 7. d Paris Agreement, Paris, 12 December 2015,

https://treaties.un.org/pages/ViewDetails.aspx?src=TREATY&mtdsg_no=XXVII-7-d&chapter=27&clang=_en

Wakabayashi Y, Kurita T, Horiuchi M (2008) Development of Pantograph Noise Insulating Panels, JR EAST Technical Review, No. 12, pp. 28–33.

Wang H, Zhou Y (2009) The finite-length square cylinder near wake. J Fluid Mech 638:453–490. https://doi.org/10.1017/S0022112009990693

Wang Y (2019) Effects of Reynolds number on vortex structure behind a surface-mounted finite square cylinder with AR = 7, Phys. Fluids 31, 115103 (2019); doi: 10.1063/1.5123994

Wen X, Liu Y, Li Z, Chen Y, Peng D (2018) Data mining of a clean signal from highly noisy data based on compressed data fusion: a fast-responding pressure-sensitive paint application. Phys Fluids. 30, 097103 https://doi.org/10.1063/1.5046681

Yamamoto K, Takagi K (1991) Expressions of Maekawa's Chart for Computation, Journal of the INCE of Japan, Vol.15 No. 4, pp. 202-205 (in Japanese)

Yamamoto K, Hotta R, Takagi K (1994) A method for the calculation of noise attenuation by finite length barrier, Journal of the Acoustical Society of Japan, Vol.50 No. 4, pp. 271-278 (in Japanese)

Yamazaki N, Takaishi T (2007) Wind Tunnel Tests on Reduction of Aeroacoustic Noise from Car Gaps and Bogie Sections, Quarterly Report of RTRI, Vol. 48, No.4, pp.229-235.

Yamazaki N, Uda T, Kitagawa T, Wakabayashi Y (2019b) Influence of Bogie Components on Aerodynamic Bogie Noise Generated from Shinkansen Trains, Quarterly Report of RTRI, Vol. 60, No. 3 pp. 202-207

Yamazaki N, Nakayama M, Nishimura T (2019a) A method to evaluate the aeroacoustic bogie noise of Shinkansen high-speed trains by considering the acoustic field, Transactions of the JSME (in Japanese) 85 (869), Vol. 85 No. 869 p. 18-00316

Acknowledgment

This work is the outcome of the research over 10 years (FY2012 to FY2022) including when I have researched at Hitachi Ltd.

First of all, I wish to thank my academic supervisor, Associate Professor Taku Nonomura, Department of Aerospace Engineering, Graduate School of Engineering, Tohoku University. He always provided adequate advice on how to advance this research. I am honored to have had the opportunity to graduate under his guidance. Of course, I would like to acknowledge Professor Emeritus Keisuke Asai, Tohoku University. He supported me to start this research before entering my Ph.D. course. In addition, I am deeply grateful to the members of the Nonomura laboratory for their support of this research.

I am very grateful to the members of the doctoral committee, Professor Naofumi Ohnishi, Department of Aerospace Engineering, Graduate School of Engineering, Tohoku University, Professor Hiroki Nagai and Professor Shigeru Obayashi, Creative Flow Research Division, Institute of Fluid Science, Tohoku University. My doctoral dissertation has been remarkably improved with their appropriate advice.

I am deeply grateful to Mr. Takahisa Yamamoto, Mr. Shinji Kinoshita and Mr. Ken Kawasaki of the Kasado Works, Hitachi, Ltd. for their great efforts in conducting this research. I would like to take this opportunity to express my appreciation to them.

I would like to thank Mr. Kiyoshi Morita, Mr. Tomoo Hayashi, Mr. Yukinobu Abe and my colleagues in the Research and Development Group, Hitachi, Ltd. I would like to take this opportunity to thank them for their discussions and cooperation in carrying out this study. I look forward to working with them in the future.

Finally, I am also grateful to my family for their support in keeping a balance between work and student life.